

ARPES and NMTO Wannier Orbital Theory of $\text{LiMo}_6\text{O}_{17}$ - Implications for Unusually Robust Quasi-One Dimensional Behavior

L. Dudy

Randall Laboratory, University of Michigan, Ann Arbor, MI 48109, USA
Physikalisches Institut und Röntgen Center for Complex Material Systems,
Universität Würzburg, D-97074 Würzburg, Germany
and
Synchrotron SOLEIL, L'Orme des Merisiers, 91190 Saint-Aubin, France

J.W. Allen

Randall Laboratory, University of Michigan, Ann Arbor, MI 48109, USA

J.D. Denlinger

Advanced Light Source, Lawrence Berkeley National Laboratory, Berkeley, CA 94720, USA

J. He

Department of Physics and Astronomy, Clemson University, Clemson, SC 29534, USA

M. Greenblatt

Department of Chemistry & Chemical Biology, Rutgers University, 123 Bevier Rd. Piscataway, NJ 08854, USA

M.W. Haverkort

Max-Planck-Institut für Festkörperforschung, Heisenbergstrasse 1, D-70569 Stuttgart, Germany
Max-Planck-Institut für Chemische Physik fester Stoffe,
Nöthnitzer Str. 40, D-01187 Dresden, Germany
and
Institut für Theoretische Physik, Universität Heidelberg,
Philosophenweg 16, D-69120 Heidelberg, Germany

Y. Nohara and O.K. Andersen*

Max-Planck-Institut für Festkörperforschung, Heisenbergstrasse 1, D-70569 Stuttgart, Germany
 (Dated: December 11, 2018)

We present the results of a combined study by band theory and angle resolved photoemission spectroscopy (ARPES) of the purple bronze, $\text{Li}_{1-x}\text{Mo}_6\text{O}_{17}$. Structural and electronic origins of its unusually robust quasi-one dimensional (quasi-1D) behavior are investigated in detail. The band structure, in a large energy window around the Fermi energy, is basically 2D and formed by three Mo t_{2g} -like extended Wannier orbitals, each one giving rise to a 1D band running at a 120° angle to the two others. A structural "dimerization" from $\mathbf{c}/2$ to \mathbf{c} gaps the xz and yz bands while leaving the xy bands metallic in the gap, but resonantly coupled to the gap edges and, hence, to the other directions. The resulting complex shape of the quasi-1D Fermi surface (FS), verified by our ARPES, thus depends strongly on the Fermi energy position in the gap, implying a great sensitivity to Li stoichiometry of properties dependent on the FS, such as FS nesting or superconductivity. The strong resonances prevent either a two-band tight-binding model or a related real-space ladder picture from giving a valid description of the low-energy electronic structure. We use our extended knowledge of the electronic structure to newly advocate for framing $\text{LiMo}_6\text{O}_{17}$ as a weak-coupling material and in that framework can rationalize both the robustness of its quasi-1D behavior and the rather large value of its Luttinger liquid (LL) exponent α . Down to a temperature of 6 K we find no evidence for a theoretically expected downward renormalization of perpendicular single particle hopping due to LL fluctuations in the quasi-1D chains.

* oka@fkf.mpg.de

CONTENTS

I. Introduction	2	C. Experimental Extraction of the FS	47
II. Methods	5	1. Fermi-surface analysis	48
A. ARPES	5	2. Dispersion Analysis	49
B. NMTO full-potential calculations	6	3. Sparrow Analysis	49
III. Crystal structure and basic electronic structure	8	References	49
A. Crystal structure	8		
B. Basic electronic structure	10		
IV. Wannier orbitals and Hamiltonian	13		
A. Low-energy t_{2g} Wannier orbitals (WOs)	14		
B. Other sets of Wannier-functions (WFs)	15		
C. Six-band t_{2g} Hamiltonian	16		
D. $\{\mathbf{k}, \mathbf{k} + \mathbf{c}^*\}$ representation	16		
V. ARPES intensity variations and energy bands	18		
A. FS intersection with planes where $k_c = \text{const}$	18		
B. Simple theory of ARPES intensity variations	19		
C. Constant-energy surfaces in the $(6, k_b, k_c)$ plane	21		
D. Energy bands, $E_j(k_b, k_c)$	22		
E. Agreement between the LDA and ARPES	24		
VI. The quasi-1D bands in the gap	25		
A. Seeing the resonance peak in ARPES	25		
B. Refining the six-band TB Hamiltonian to agree with ARPES	25		
C. Dispersion and splitting of the bands in the gap	26		
D. Fermi surface and velocities	27		
E. Discussion of FS-nesting and gapping	30		
VII. Conclusion and Implications	33		
Acknowledgments	35		
A. Six-band TB Hamiltonian	35		
1. Sublattice representation	35		
2. $\{ \mathbf{k}\rangle, \mathbf{k} + \mathbf{c}^*\rangle\}$ representation	37		
3. Mixed representation	38		
B. Löwdin-downfolded two-band Hamiltonian	39		
1. Origin of the perpendicular dispersion and splitting of the quasi-1D bands in the gap	40		
a. Peak-, bulge-, and near band-crossing features	40		
b. Directly coupled terms	41		
c. Symmetries	41		
d. Indirectly coupled terms; role of the denominators	41		
e. Indirectly coupled terms; role of the residues	43		
f. xy - xz and xy - yz hopping integrals	45		
g. Synthesis	45		
2. Spin-spiral bands	46		

I. INTRODUCTION

In our three dimensional reality, prototypical realizations showing the concept of quasi-one-dimensional (quasi-1D) metals are rare. In quasi-1D metals, the Fermi liquid paradigm is replaced by the so-called Luttinger liquid in which the elementary excitations are of collective bosonic nature [1], called spinon and holon, reflecting the famous spin-charge separation. More or less ideal quasi-1D systems can be found, i.e. by ARPES experiments [2–6], in a variety of materials. $\text{LiMo}_6\text{O}_{17}$, often called the lithium purple bronze (LiPB) [7], appears to be an almost perfect realization of a quasi-1D metal. With decreasing temperature, there is no clear evidence for 1D to 3D crossover until it becomes a superconductor below a temperature T_{SC} of 1.9K. LiPB has a long history since its discovery [8] and subsequent structure determination [9] where a large part is a repeated effort to interpret a resistivity upturn for T less than $\sim 25\text{K}$ as signaling 1D to 3D crossover, e.g. as a transition to a charge density wave (CDW) or spin density wave (SDW). But thus far [10], direct signatures of density wave order, e.g. of a gap by optical spectroscopy or angle resolved photoemission spectroscopy (ARPES) or of a unit cell enlargement by x-ray diffraction, have not been found. Instead, there is direct evidence against either a CDW [11] or an SDW [12].

Set against this lack of evidence for crossover before the onset of superconductivity at T_{SC} , there is evidence for unusually robust 1D behavior [10]. The resistivity upturn itself can be well described as a power law, suggesting 1D behavior of some sort. Also the upturn can be suppressed by a large magnetic field, but only if applied along the 1D axis [13]. Further, spectral signatures from ARPES [10, 14, 15] and scanning tunneling spectroscopy [16] are strongly non-Fermi liquid-like from 300K down to at least 4K. Both, STM and ARPES, display in the momentum integrated single particle spectral function a power law approach to the Fermi energy E_F . Within the framework of the 1D Tomonaga-Luttinger (TL) model, a paradigm model for Luttinger liquid behavior, the power law is interpreted as the anomalous exponent α . Additionally, ARPES line shapes at temperatures 250K to 300K are well described by the TL spectral function, showing [10, 17, 18] both spinon edge and holon peak features, albeit broadened by temperature and experimental resolution. But there are also substantial T -dependent departures from the TL model. With decreasing T the exponent varies with T , from $\alpha = 0.9$ at 250K to 0.6 at 50K [14], and also the low- T ARPES lineshape does not

sharpen enough to agree with the low- T TL lineshape [10, 15], although it does continue to display quantum critical scaling, a characteristic 1D property [15]. These spectral findings are nicely complemented by the observation of a large departure from the Wiedemann-Franz law [19], interpreted as a signature of charge-spin separation. So far these measurements were not done below 30K. If the normal state just above T_{SC} is indeed of quasi-1D character then the superconductivity could be unconventional, as is also suggested by recent transport studies that find the upper critical field to be much larger than the Pauli limiting value[20]. Furthermore, a sufficiently large magnetic field along the 1D axis appears to induce superconductivity in a sample which is not superconducting[21]. Thus far, it is not known what variable controls whether or not a sample displays superconductivity. The variability of the Li content, which controls the carrier density, is one hypothesis.

A rigorous explanation of all these observations demands the choice of an appropriate electronic model. The basic band structure in the vicinity of the Fermi-energy (E_F) has been known for many years from pioneering tight-binding (TB) calculations based on the extended-Hückel method[22]. There are two approximately 1D bands dispersing across E_F , associated with there being two chains (and two formula units) per primitive cell. They have Mo $4d_{xy}$ character and for stoichiometric $\text{LiMo}_6\text{O}_{17}$ they are each half filled. There are also two filled bands not far below E_F . This basic picture agrees with the first local density-functional (DFT-LDA) calculation [23], performed with the linear muffin-tin orbital method (LMTO), and has been confirmed by ARPES. Higher-resolution low-temperature ARPES data and more accurate LDA-NMTO calculations show agreement even on the details [24] of the filled bands.

There are two seminal many-body models which start from the zigzag arrangement ($\backslash_{\text{Mo1}}/\text{Mo4}\backslash$) of the Mo atoms forming a chain and regard the two chains per cell as a ladder [25][26]. Guided by LDA-LMTO band structures [23, 27], both models construct a TB model with xy orbitals on Mo1 and Mo4, i.e. with four orbitals per cell, and hopping between nearest orbitals in a chain ($\tau \sim 0.8\text{ eV}$)[28, 29], in a ladder (t_\perp), and in neighboring ladders (t'_\perp). This one-body part of the Hamiltonian is augmented by Coulomb repulsions: on-site ($U = 6.4\text{ eV}$ [23]) as well as intra- and inter-ladder ($V, V_\perp, V'_\perp, \dots$). The two models use similar values for the inter-site repulsions ($V \sim V_\perp \sim 1\text{ eV}$) and, within a factor two, for the perpendicular hoppings ($t_\perp \sim 20\text{ meV}$).

In both of these models [25][26] there is great emphasis on viewing the chain bands as quarter filled rather than half filled, with a conduction electron for every *second* Mo atom along a chain. In this view Mo1 and Mo4 are regarded as equivalent, the primitive translation is taken as $\mathbf{b}/2$ rather than \mathbf{b} , and the gap at the boundary of the proper Brillouin zone, $\pm\mathbf{b}^*/2$, around the middle of the xy bands (1.5 eV above E_F), judged to be merely a few per cent of the bandwidth $\sim 3.6\text{ eV}$ [26],

is neglected. The motivation is to make contact with a property of quarter-filled Hubbard models [1], that an insulating Mott state cannot be achieved with a local U alone, but requires also a nonlocal V interaction, which can then favor localization and so-called $4k_F$ charge ordering of an electron to every other site, or at least charge fluctuations toward this situation. In the case of ladders or a lattice of ladders, including also the Coulomb repulsions between the chains, the charge ordering is a checkerboard pattern [25][26]. For the half filled band below the dimerization gap a Mott state can be achieved with U alone, but with localization to the bond orbitals appropriate to this band (see below), rather than to site orbitals. Also a $2k_F$ CDW or SDW, which would double the unit cell from \mathbf{b} to $2\mathbf{b}$ is in principle possible (but has never been found in x-ray diffraction, as noted already above). Dimerization is known to greatly diminish the tendency toward $4k_F$ charge ordering [30], and presumably V must be sufficiently large relative to the dimerization gap in order for the quarter filled scenario to have relevance. In fact the dimerization gap is actually 0.7 eV, i.e. 20% of the entire bandwidth, an order of magnitude greater than estimated in Ref. 26, but still somewhat less than the largest of the V -values that are contemplated in these models.

The quarter filled ladder model has been used for a number of theoretical discussion of the properties of LiPB[31–35]. Ref. 26 derived a low-energy TL theory which attempted to understand the experimental observations down to an energy scale of perhaps 30 K. In this work, the combination of having a ladder, nonlocal V -interactions, and especially renormalization due to the $4k_F$ chain and ladder interactions, was crucial for rationalizing the large value of $\alpha > 0.5$ in LiPB, because for a single 1D Hubbard chain with U alone the maximum value of α , achieved as U goes to infinity, is $1/8$. Ref. 31 also explored the implications for LiPB of the $4k_F$ charge fluctuations, proposing a mechanism for the resistivity upturn, and rationalizing the LiPB α -value. This study took U values in the range of 1 eV to 2 eV, perhaps influenced by the work described in the next paragraph. In contrast to early theory which took rather generic quasi-1D TB models to discuss the possibility of triplet SC in LiPB [36, 37], three somewhat later papers [32–34] employed the quarter-filled ladder model for theorizing about possible symmetries of the SC order parameter. The most recent work [35] with the quarter-filled ladder model introduces additionally the orbitals that produce the filled bands below E_F , and their antibonding partner bands above E_F , and considers the implications of the possibility that these bands enable a gas of exceptionally long lived excitons that interacts with the electrons in the 1D chain bands to produce the surprising low temperature properties of LiPB described above, including its power-law resistivity upturn, its associated negative magnetoresistance, an interesting magneto-chromatic effect [38], and the low- T departures of the ARPES line-shapes from those of the TL model.

An alternate TB model [39] has been derived without fitting to the LDA band structure, in this case obtained using the full-potential linear augmented-plane wave method (LAPW) method, but by numerically projecting from it four so-called maximally localized Wannier functions. These describe the two occupied bands plus the bonding parts of the two xy bands below their dimerization gaps, which are then half filled. The orbitals of this model are therefore not atomic, but essentially the bonding linear combination of those on Mo1 and Mo4, and the integral for hopping between these xy bond orbitals is only about half the one for hopping between the atomic orbitals considered in the TB models previously used [25][26]. The Coulomb repulsions between two electrons on the same bond-orbital (U) is added to the TB Hamiltonian and the resulting Hamiltonian is solved both using dynamical mean-field theory (DMFT), which neglects the off-site (bond) elements of the self-energy, and using the variational cluster approximation (VCA) with clusters containing up to 8 bond orbitals. Neither of these treatments of the Coulomb interactions is capable of capturing the 1D chain physics, i.e. the charge-spin separation, lack of quasi-particles and presence of collective modes that are manifested in the LiPB spectroscopic and transport measurements, or the interplay between chain physics and lattice physics. Nonetheless it is probably a generically correct conclusion that U has an upper limit in the range of 0.7 to 1.5 eV (depending on the method used) in order that the generally good agreement found between dispersing ARPES peaks and the authors' LDA bands not be upset. This is of course broadly consistent with the expectation for a 3D material that for a half-full band, a U -value larger than the bandwidth causes localization. Considering the fact that the interacting Hamiltonian is expressed in terms of bond-orbitals, this is not necessarily in conflict with the quarter-filled ladder models, but it does preclude a description of the site-based $4k_F$ charge fluctuations that motivate these models, and whether it can be used as a basis for a successful low-energy TL theory of LiPB has not been investigated. This study [39] also provides a simplified two-band TB Hamiltonian by folding the two occupied bands down into the two xy bands and *fitting* their hybridization such as to modify the t_\perp parameters. The result is said to be in good agreement with those discussed in Ref. [26].

Besides the choice of an appropriate electronic model, with quarter or half filling, a second major issue concerns the precise values and origins of the t_\perp hopping parameters. Within the usual theory of quasi-1D metals, the 1D to 3D crossover temperature is controlled by the magnitude of electron hopping between the coupled chains. This hopping is characterized by a single-particle matrix element t_\perp , or more generally by several different such t_\perp values, depending on the range of the hopping. Crossover is expected as T decreases below the scale set by t_\perp . However, theory suggests that Luttinger liquid fluctuations on the chains can strongly suppress the single-particle

hopping and consequently the crossover T . In the case of one chain per primitive cell and hopping only to the nearest chain, the suppression is to an effective value $t_\perp(t_\perp/\tau)^{\alpha/(1-\alpha)}$, where τ is the nearest neighbor intra-chain hopping integral [1]. LDA calculations to date have suggested values of $t_\perp = 20$ meV and $\tau = 0.8$ eV for LiPB. With the low- T value of $\alpha = 0.6$, one obtains [10] a very small effective t_\perp -value of 0.62 meV or 7.1 K, only a few degrees larger than the value of T_{SC} . Such a small value might thus account for the exceptional stability of 1D physics in this material, and should be manifest in the low- T single-particle electronic structure. Of great additional interest is the validity of the ladder picture, which involves the relative magnitudes of the hoppings within and between unit cells. There is thus a strong motivation to characterize the perpendicular dispersion as well as possible, but up to now this has not been done with ARPES and has not been scrutinized theoretically as carefully as is possible when using the chemically most sound set of Wannier functions, as summarized in the next paragraph.

The present paper presents the results of new theory applied to interpret new ARPES experiments for the electronic structure of LiPB, directed at the various issues set forth above. We need –and therefore present in Section III – an overview of the electronic structure and an improved 3D visualization of the crystal structure, with an associated wording: ribbons containing Mo1, Mo2, Mo4, and Mo5 for zigzag chains and bi-ribbons for ladders (see FIG. 1). In the new theory, we perform an LDA Wannier-function calculation (Sections II B and IV) with the full-potential version [40, 41] of the Nth-order muffin-tin orbital (NMTO) method [42]. We obtain the set of all three (per formula unit) t_{2g} Wannier Orbitals (WOs), not only the xy orbitals, but also the xz and yz orbitals. Also the latter form 1D bands, but with primitive translations $(\mathbf{c} \pm \mathbf{b})/2$ until the dimerization to $\mathbf{c} \pm \mathbf{b}$ gaps them around E_F (see FIGs. 5, 6, and 9). Indeed, the structural reason why LiPB is 1D while (most) other Mo bronzes are 2D [43, 44] is exactly this $\mathbf{c}/2$ to \mathbf{c} dimerization of the ribbons (zigzag chains) into bi-ribbons (the two zigzag chains are not related by a translation). Note that this dimerization of the xz and yz bands causing them to gap at $2k_F$ is distinct from the $\mathbf{b}/2$ to \mathbf{b} dimerization causing the xy bands to gap at $4k_F$. Hybridization between the resulting valence and conduction bands and the metallic xy bands [45] induces the striking $k_\perp = k_c$ -dependent features seen in FIG. 12 and described in Sect. VI: Around the zone center, $k_c = 0$, a *reduced* splitting of the two xy bands and a flattening of the lower band. Near $k_c = 0.25$, a peak in the upper xy band caused by repulsion from (resonance with) the valence band. Around the zone boundary, $k_c = 0.5$, a bulge in the lower xy band caused by the $\mathbf{c}/2$ to \mathbf{c} dimerization. These structures depend strongly on the energy position in the gap and therefore cause Fermi-surface warping and splitting which depend strongly on the value of E_F , as set by the effective Li stoichiometry

(see summary FIG. 13 and FIG. 16, third row left column). The resonance structures near $k_c=0.25$ and the bulge around $k_c=0.5$ prevent $2k_F$ instabilities, and only for doping beyond $\text{Li}_{\sim 1.05}$ gapping around $k_c=0$ might be possible (Sect. VIE). This E_F dependence of the perpendicular dispersion cannot be captured with a Wannier basis containing only one, e.g. the bonding, xz/yz function [39]. We therefore include WOs which account not only for the valence but also for the conduction bands, leading to a very accurate and yet portable (i.e. analytical) t_{2g} six-band TB Hamiltonian (Sect. IV and App. A). Subsequent analytical Löwdin downfolding to a two-band Hamiltonian which has resonance- rather than TB form (Eq. (B2) in App. B), enables a new and detailed understanding of all the various microscopic contributions to the perpendicular dispersion, and of their relation to the crystal structure (App. B1, summarized in App. B1g, and FIG. 16).

The theory is validated in detail by new higher-resolution ARPES experiments (Sect. IIA) for two different samples, down to temperatures of 6K and 26K. Because the low- T lineshapes are too broad to be well described by TL theory [10, 15], the resulting data have been analyzed for dispersion by model independent procedures (App. C). The data and the analysis results are presented (FIGs. 7-11, 14, and 17) at appropriate places in the course of the presentation of the theory. As found previously [24][39] there is very good general agreement with LDA dispersions up to 150 meV below E_F (FIGs. 7 and 9). Refinement (Sect. VIC and Fig. 11) of the LDA-derived parameters of the six-band Hamiltonian yields an accurate and detailed description of the ARPES low-energy band structure, including the reduced splitting, resonance, and bulge features of the xy bands and associated distinctive Fermi-surface features. The direct observation of these features (Sects. VIB, VID, and FIGs. 7(b2), 11(c2), and 14), not identified in our previous ARPES studies, is enabled partly by the low temperature and general goodness of the new data, but more importantly by the recognition and application of an ARPES selection rule (Sect. VB and Figs. 8-10) that is based on the approximate $\mathbf{c}/2$ -translational symmetry and allows us, for the first time, to separate the two quasi-1D xy bands near and at E_F .

Our set of generalized Wannier functions has been chosen as small as possible for an intelligible and accurate description of the covalency effects, but like in the previous study [39], this leads to orbitals which are not atomically localized and therefore not suited to describe the site-based $4k_F$ charge fluctuations envisioned in the quarter filled models. It should however be straight forward to augment our set of six Mo1-centered t_{2g} WOs with the those on Mo4, thus arriving at a 12-orbital Hamiltonian with sufficiently localized WOs (Sect. IVB), which could be a starting point for future studies including both resonance- and Coulomb-correlation effects on the same footing. However, whether or not such a picture is actually needed depends very much on whether the strong

effects of covalency are actually overcome by the magnitudes of the V -type Coulomb repulsions, which have so far only been estimated.

Nonetheless the results of our 6-orbital description of the new ARPES data have important implications for the issues set forth above and these are detailed in the final section VII of the paper. We will propose possible key alternatives to various aspects of the current models in the literature, flowing from our results for the perpendicular dispersion and the details of the FS. The resonance features of the dispersion are extremely long range and do not have tight-binding form. Therefore they are missing from all the previous TB and TL models and so these models will not be sufficient for any property that may be sensitive to the resonance FS features or to their strong dependence on the stoichiometry, for example the SC. The magnitude and long range character of the resonance contributions also argue against a ladder visualization of the electronic structure. Another general sense of our proposals is that the Coulomb interactions may be both weaker and more long range than have been contemplated in the current models, in essence that perhaps LiPB is better viewed as a weak coupling material. Finally, the strong low temperature LL renormalization of the perpendicular dispersion, that is part of usual LL theory, does not occur for LiPB down to 5K. In spite of these changes in viewpoint, we can nonetheless account for the large value of α in LiPB and we can offer a strong rationalization of its robust 1D nature.

II. METHODS

A. ARPES

We measured several samples for the conclusions presented in this work. The samples came from two different crystal growers and were all prepared by a temperature gradient flux growth technique [46]. In the text, we refer to two samples G (M. Greenblatt) and H (J. He) representing the variation detectable in our experiments.

Photoemission measurements were performed at the MERLIN endstation (BL 4.0.3) of the Advanced Light Source with a Scienta R4000 electron detector. The polarization was set to linear vertical, i.e. in FIG. 9 the vector of the electric field horizontal. The temperature was set to $T = 26\text{ K}$ for sample G and $T = 6\text{ K}$ for sample H and the samples were cleaved while attached to the cold manipulator at $p \approx 4e-11$ torr. The overall energy resolution was set to around 16 meV at photon energy $h\nu=30\text{ eV}$ going up to around 40 meV at $h\nu = 100\text{ eV}$. At $h\nu = 30\text{ eV}$, the momentum resolution in the \mathbf{b}^* -direction (which will be defined in Section IIIA) is 2% of k_{Fb} at half-filling (i.e. at nominal Li_1 stoichiometry). With the solid-state definition of reciprocal space, see between Eqs (6) and (7) in Sect. IIIA, this is 0.006 \AA^{-1} . The polarization vector in sample coordinates is:

$$\frac{\mathbf{E}}{|\mathbf{E}|} = \begin{pmatrix} e_a \\ e_b \\ e_c \end{pmatrix} = \begin{pmatrix} \sin(75^\circ - \phi) \cos \theta \\ \sin(75^\circ - \phi) \sin \theta \\ \cos(75^\circ - \phi) \end{pmatrix}. \quad (1)$$

Here, ϕ is the polar rotation and the θ the tilt angle. In our measurements, $|\phi| \lesssim 5^\circ$ and $|\theta| \lesssim 5^\circ$ resulting overall in a strong component along the **a**-axis, a weak component along the **c**-axis, and a very weak component along the **b**-axis.

LiMo₆O₁₇ is susceptible to oxygen loss caused by intense ultraviolet light where the desorption is due to the Knotek-Feibelman mechanism including a core level excited resonant Auger decay [47]. It shares this behavior with, i.e. NaMo₆O₁₇[48], K_{0.3}MoO₃[44], or oxides like TiO₂[49] and SrTiO₃[50]. We were not able to prevent this damage by oxygen dosing, as i.e. possible for SrTiO₃[51]. A small oxygen loss causes a slight electron doping, but, as time progresses, the ARPES signal eventually blurs. In order to prevent the loss, one concept might be to keep the photon energy below that of the lowest energy core level resonance. However, often there is higher order light that still causes a slow degradation (with timescale in the hours instead of minutes) and therefore our concept is to use a large homogenous area and slightly alter the position of the beam-spot when the sample degradation begins.

Even though the ARPES lineshapes have the general 1D holon-peak and spinon-edge features mentioned already above, they were analyzed by a model free method described in detail in App. C. This procedure was necessitated because the low- T ARPES lineshape is not sharp enough to agree in detail with the low- T TL lineshape[15]. If the TL lineshape is broadened ad hoc it can be made to fit[10], but we did not want to use that ad hoc procedure in the current work.

B. NMTO full-potential calculations

The electronic-structure calculations were performed for the stoichiometric crystal with the structure determined for 2(LiMo₆O₁₇) [9]. Doping –which is small due to the opposing effects of Li intercalation and O deficiencies– is treated in the rigid-band approximation.

For the DFT-LDA [52] calculations, including the generation of Wannier functions and their TB Hamiltonian, we used the recently developed selfconsistent, full-potential version [40, 41] of the Nth-order muffin-tin orbital (NMTO) method [42, 53, 54]. Since NMTO Wannier functions are generated in a very different way than maximally localized Wannier functions [55] making them useful for many-body calculations also for d - and f -electron atoms at low-symmetry positions [56], and since NMTOs were hitherto generated for MT potentials imported from selfconsistent LMTO-ASA or LAPW calculations [57, 58] rather than selfconsistently in full-

potential calculations, here follows a fairly complete description of the new method as applied to LiPB:

We first generated the full potential by LDA calculation using a large basis set consisting of the Bloch sums of the two Li $2s$ NMTOs per primitive cell, containing 2(LiMo₆O₁₇), of all 60 Mo $4d$ NMTOs, of all 136 O $2s$ and $2p$ NMTOs, plus of all 1s NMTOs on interstitial sites with MT radius larger than 1 Bohr radius. This large basis set thus contained over 200 NMTOs. After each iteration towards selfconsistency, the full potential is least-squares fitted [59] to the form of an overlapping MT potential. Such a potential is a constant, the MT zero, plus a superposition of spherically symmetric potential wells, $\sum_R v_R(|\mathbf{r} - \mathbf{R}|)$, centered at the atoms and the larger interstitials. The ranges of the potential wells, the MT radii, s_R , were chosen to overlap by 25%. Specifically: $s_{\text{Mo}}=2.34\text{--}2.55$, $s_{\text{O}}=1.72\text{--}1.89$, $s_{\text{Li}}=2.87$, and $s_{\text{E}}=1.03\text{--}2.48$ Bohr radii. The overlap considerably improves the fit to the full potential. This overlapping MT potential is now used to generate the NMTO basis set for the next iteration towards charge selfconsistency and, after selfconsistency has been reached, to generate a basis set of merely the 6 Bloch sums of the Mo1 $4d(t_{2g})$ NMTOs which, after symmetrical orthonormalization and Fourier transformation to real space, becomes our set of Wannier functions describing the 6 bands around the Fermi level.

Next, we describe the construction of the NMTOs: For each MT well, $v_R(r)$, and energy, E , the radial Schrödinger [60] equations for $l=0, \dots, l_{\text{max}}$ are integrated outwards from the origin to the MT radius thus yielding the radial functions, $\varphi_{Rl}(E, r)$, and their phase-shifts, $\eta_{Rl}(E)$. Continuing the integration smoothly inwards – this time over the MT zero – yields the phase-shifted free wave, $\varphi_{Rl}^o(E, r)$, which is truncated inside the so-called hard-sphere with radius, $a_R \approx 0.65s_R$. The difference, $\varphi_{Rl}(E, r) - \varphi_{Rl}^o(E, r)$, often referred to as a *tongue*, goes smoothly to zero at the MT sphere and jumps to $\varphi_{Rl}(E, r)$ inside the hard sphere. After multiplication by the appropriate cubic harmonic, $Y_{lm}(\hat{\mathbf{r}})$, these partial waves will be used to form the NMTOs. Partial waves with the same Rlm as one of the NMTOs in the basis set are called *active*, and the remaining partial waves *passive*. Since $l_{\text{max}}=4, 3, 3$, and 2 for respectively Mo, O, Li, and E, the vast majority of partial waves were passive.

In order to combine the many partial waves into the basis set of NMTOs, $\chi_{Rlm}(\mathbf{r})$, we first form their envelope functions: the active set of wave-equation solutions, $\psi_{Rlm}(E, \mathbf{r})$, so-called screened spherical waves, which satisfy the boundary conditions that any cubic-harmonic projection around any site, $\hat{P}_{R'l'm'}(r_{R'})\psi_{Rlm}(E, \mathbf{r})$, has a node at the hard-sphere radius if $R'l'm'$ is active and differs from Rlm , and has the proper phase shift, $\eta_{R'l'}(E)$, if $R'l'm'$ is passive. The node-condition is what makes the screened spherical wave localized –and the more, the larger the basis set, i.e. the number of active channels. The input to a screening calculation is the energy, the hard-sphere structure, and the passive phase shifts. The output is the screened structure- or slope

matrix whose element, $S_{R'l'm', Rlm}(E)$, gives the slope of $\psi_{Rlm}(E, \mathbf{r})$ at the hard sphere in the active $R'l'm'$ channel. The set of screened spherical waves is then augmented by the partial waves to become the basis set of energy-dependent MTOs (EMTOs) [61], $\phi_{Rlm}(E, \mathbf{r})$. The EMTO has a head formed by the active partial wave with the *same* Rlm plus passive waves, and a tail, which inside the other MT spheres is formed solely by passive partial waves. Hence, all active projections, except the own, vanish. Such an EMTO is localized, everywhere continuous, and everywhere a solution of Schrödinger's equation for the MT potential –except that it has *kinks* at all hard spheres in the active channels, and is therefore also called a *kinked partial wave* [42, 62]. The kink, $K_{R'l'm', Rlm}(E)$, at the hard sphere in channel $R'l'm'$ is

$$S_{R'l'm', Rlm}(E) - \delta_{R'l'm', Rlm} \left. \frac{\partial \ln \varphi_{Rl}^o(E, r)}{\partial \ln r} \right|_{a_R}. \quad (2)$$

This kink matrix also equals the MT Hamiltonian minus the energy in the EMTO representation, $\langle \phi(E) | -\nabla^2 + \sum_R v_R - E | \phi(E) \rangle$. Any linear combination of EMTOs with the property that the kinks from all heads and tails cancel, is a solution with energy E of Schrödinger's equation for the overlapping MT potential –except for the tongues sticking into neighboring MT spheres and thereby cause errors of 2nd and higher order in the potential overlap. This kink-cancellation condition gives rise to the screened KKR equations of band theory.

For a Hamiltonian formulation, however, we need an energy-independent basis set. Analogous to the linearization well-known from LAPWs and LMTOs [63], this set is arrived at by Nth-order polynomial interpolation in the Hilbert space of EMTOs with energies at a chosen mesh of $N+1$ energies, $\epsilon_0, \dots, \epsilon_N$:

$$\chi_{R'l'm'}(\mathbf{r}) = \sum_{\nu=0}^N \sum_{Rlm}^{\text{active}} \phi_{Rlm}(\epsilon_\nu, \mathbf{r}) L_{Rlm, R'l'm'}(\epsilon_\nu). \quad (3)$$

Here, $\chi_{R'l'm'}(\mathbf{r})$ is the set of Nth-order MTOs and $L(\epsilon_\nu)$ is the matrix of Lagrange coefficients which is given by the kink matrix (2) evaluated at the points of the energy mesh. For an NMTO, the kinks are reduced to discontinuities of the $(2N+1)$ st derivatives at the hard spheres. Also the MT-Hamiltonian- and overlap matrices in the NMTO representation, $\langle \chi | -\nabla^2 + \sum_R v_R | \chi \rangle$ and $\langle \chi | \chi \rangle$, are given by the kink matrix (plus its first energy derivative) evaluated at the energy mesh.

The NMTO set may be arbitrarily small and, nevertheless, it spans the exact solutions at the $N+1$ chosen energies of Schrödinger's equation for the MT potential to 1st order in the potential overlap [64]. Specifically, a set with n orbitals yields n eigenfunctions and eigenvalues, E , whose errors are proportional to respectively $(E - \epsilon_0) \dots (E - \epsilon_N)$ and $(E - \epsilon_0)^2 \dots (E - \epsilon_N)^2$. The choice of NMTO set, i.e. which orbitals to place on which atoms, merely determines the prefactors of these errors and the range of the orbitals. But only with chemi-

cally sound choices, will the delocalization of the EMTOs caused by the N-ization in Eq. (3) be negligible.

In order to explain this, we now consider the simple example [58] of NiO: Placing the three p -orbitals on every O, the five d -orbitals on every Ni, and letting the energy mesh span the 10 eV region of the pd -bands, generates a basis set of eight atomic-like NMTOs yielding the eight pd -bands and wave functions. Placing merely the three p -orbitals on every O and letting the mesh span the 5 eV region of the O p -bands, generates a basis set, consisting of O p -like NMTOs with bonding d -like tails on the Ni neighbors, which yields accurate p -bands and wave functions. Placing, instead, the five d -orbitals on every Ni and letting the mesh span the 4 eV region of the Ni d -bands, generates a basis set of Ni d -like NMTOs which have antibonding p -like tails on the O neighbors and yields accurate d -bands and wave functions. With the five d -orbitals on Ni, *but* a mesh spanning the three O p -bands, we get three $d(t_{2g})$ -like Ni NMTOs, xy , xz , and yz , with large $pd\pi$ -bonding p -tails on the four O neighbors in the plane of the t_{2g} -orbital, plus the two $d(e_g)$ -like Ni NMTOs with huge $pd\sigma$ -bonding tails – on the two apical oxygens for $3z^2 - 1$, and on the four oxygens in the xy plane for $x^2 - y^2$. These fairly delocalized Ni d -NMTOs clearly exhibit the Ni-O bonding, but they form a schizophrenic basis set which yields the three O p -bands connected across the pd -gap to two of the five Ni d -bands by steep "ghost" bands.

This example indicates how the NMTO method can be used to explore covalent interactions in complex materials. Other examples may be found in Refs. 65 and 66. Note that the fewer the bands to be picked out of a manifold, i.e. the more diluted the basis set, the more extended are its orbitals because the set is required to solve Schrödinger's equation in all space. As a consequence, the smaller the set, the more complicated its orbitals.

Generalized Wannier functions are finally obtained by orthonormalization of the corresponding NMTO set. Symmetrical orthonormalization yields a set of Wannier functions, which we refer to as *Wannier orbitals* (WOs) because they are atom-centered with specific orbital characters. The localization of these WOs hinges on the fact that each EMTO in the set vanishes inside the hard sphere of any other EMTO in the set. This condition essentially maximizes the on-site and minimizes the off-site Coulomb integrals and has the same spirit as the condition of minimizing the spread, $\langle \chi | |\mathbf{r} - \mathcal{R}|^2 | \chi \rangle$, used to define maximally localized Wannier functions [55].

For LiPB, we used quadratic $N(=2)$ MTOs and for the large-basis-set calculation chose the three energies $\epsilon_\nu = \pm 1$ and 0 Ry with respect to the MT zero, i.e. -22 , -8 and 6 eV with respect to the center of the gap, which is approximately the Fermi level (see FIG. 2). For the six-orbital calculation, we took $\epsilon_\nu = -0.8$, -0.4 , and 0.2 eV with respect to the center of the gap (see FIG. 7).

To the MT Hamiltonian, we finally add the correction for the tongue-overlap and the full-potential perturbation [41, 53]. Products of NMTOs –as needed for evaluation

of matrix elements and the charge density—are evaluated as products of partial waves limited to their MT spheres plus products of screened spherical waves [53, 54]. The latter are smooth functions and are interpolated across the interstitial from their first three radial derivatives at the hard sphere [40]. In order to make it trivial to solve Poisson’s equation, this interpolation uses spherical waves which—in order to make the matching at the hard spheres explicit—are screened to have all phase shifts with $l \leq 4$ equal to those of hard spheres..

The band structure obtained from our full-potential LDA calculation with the large NMTO basis set agrees well with LDA and GGA control calculations performed with the LAPW method. We did not include the spin-orbit coupling in the NMTO calculation, but by doing so with the LAPW method, we saw that the crossings between the 3rd and 4th bands along ΓZ and ZC and between the 1st and 2nd bands between $Y\Gamma$ and AB are spin-orbit split by about 80 meV. We shall return to this when discussing FIG.s 11 and 12.

For the low-energy electronic structure of $2(\text{LiMo}_6\text{O}_{17})$ we need to pick from the sixty Mo 4d bands above the O 2p – Mo 4d gap (see FIG. 2) a conveniently small and yet separable set of bands around the Fermi level. In this case, where no visible gap separates such bands from the rest of an upwards-extending continuum, the NMTO method is uniquely suited for picking a subset of bands for which the Wannier set is intelligible and as localized as possible. This direct generation of WOs (through trial and error by inspecting the resulting bands like we discussed above for NiO) differs from the procedure for projecting maximally localized Wannier functions [55] from the entire band structure using some large basis set. We shall return to it in Sect. IV after the crystal structure and the basic electronic structure of LiPB have been discussed.

Since the resulting set of six NMTOs may have fairly long range, all LDA calculations were performed in the representation of Bloch sums,

$$\chi_{Rm}(\mathbf{k}, \mathbf{r}) \equiv \sum_{\mathbf{T}} \chi_{Rm}(\mathbf{r} - \mathbf{T}) e^{2\pi i \mathbf{k} \cdot \mathbf{T}}, \quad (4)$$

of orbitals translated by the appropriate lattice vector, \mathbf{T} . Specifically, the screening of the structure matrix was done \mathbf{k} -by- \mathbf{k} . In order to obtain printable WOs and a portable Hamiltonian whose $H_{R'm', R+Tm}$ element is the integral for hopping between the WOs centered at respectively \mathbf{R}' and $\mathbf{R} + \mathbf{T}$, we need to Fourier transform back to real space:

$$H_{R'm', R+Tm} = \frac{1}{BZV} \int_{BZ} d^3k e^{-2\pi i \mathbf{k} \cdot \mathbf{T}} H_{R'm', Rm}(\mathbf{k}), \quad (5)$$

where $1/BZV = |\mathbf{a} \cdot \mathbf{b} \times \mathbf{c}|$. For $\mathbf{T}=\mathbf{0}$ and $\mathbf{R}'=\mathbf{R}$, this is the energy of the orbital when $m=m'$, and the crystal-field term when $m \neq m'$.

III. CRYSTAL STRUCTURE AND BASIC ELECTRONIC STRUCTURE

The crystal structure of LiPB was determined and described by Onoda et al [9]. Shortly thereafter, Whangbo and Canadell [22] used the extended Hückel method to calculate and explain the basic electronic structure, but it took almost twenty years before a DFT calculation for this complicated structure was published. This was done by Popović and Satpathy [23] who used the LDA-DFT and the LMTO method. In the following we will repeat and also expand on these works, because in order to predict the perpendicular dispersion of the quasi-1D bands in detail and for unveiling it by ARPES, we need to describe not only the xy bands, but also the xz and yz bands, and this in a particular representation, the so-called $\{\mathbf{k}, \mathbf{k} + \mathbf{c}^*\}$ reciprocal-lattice representation.

A. Crystal structure

The structure of LiPB is shown in FIG. 1. There are two $\text{LiMo}_6\text{O}_{17}$ units in the primitive cell spanned by the translations \mathbf{a} , \mathbf{b} , and \mathbf{c} shown in (a). Whereas \mathbf{b} is orthogonal to both \mathbf{c} and \mathbf{a} , the latter has a tiny component along \mathbf{c} . The relative lengths of the primitive translation vectors are: $a/b \approx 2.311$ and $c/b \approx 1.720 \sim \sqrt{3} \approx 1.732$, with $b = 5.523 \text{ \AA}$. Since \mathbf{a} , \mathbf{b} , and \mathbf{c} are nearly orthogonal, so are the primitive translations, \mathbf{a}^* , \mathbf{b}^* , and \mathbf{c}^* , of the reciprocal lattice. They are defined by:

$$\begin{pmatrix} \mathbf{a} \cdot \mathbf{a}^* & \mathbf{a} \cdot \mathbf{b}^* & \mathbf{a} \cdot \mathbf{c}^* \\ \mathbf{b} \cdot \mathbf{a}^* & \mathbf{b} \cdot \mathbf{b}^* & \mathbf{b} \cdot \mathbf{c}^* \\ \mathbf{c} \cdot \mathbf{a}^* & \mathbf{c} \cdot \mathbf{b}^* & \mathbf{c} \cdot \mathbf{c}^* \end{pmatrix} \equiv \begin{pmatrix} 1 & 0 & 0 \\ 0 & 1 & 0 \\ 0 & 0 & 1 \end{pmatrix}, \quad (6)$$

where we use the crystallographic definition (cd) of the scale of reciprocal space without the factor 2π on the right-hand side used in the solid-state definition (ssd). The cd is traditionally used in diffraction and the ssd in spectroscopy. In this paper we use the cd, unless otherwise stated. The top of FIG. 2 shows half the Brillouin-zone (BZ) with origin at Γ and spanned by $\pm \mathbf{a}^*/2$ (B), $\pm \mathbf{b}^*/2$ (Y), and $\mathbf{c}^*/2$ (Z). The Bloch vector,

$$\mathbf{k} = k_a \mathbf{a}^* + k_b \mathbf{b}^* + k_c \mathbf{c}^*, \quad (7)$$

is specified by its (k_a, k_b, k_c) -components which, according to Eq.s (6) and (7), are the projections onto respectively \mathbf{a} , \mathbf{b} , and \mathbf{c} in units of respectively a^{-1} , b^{-1} , and c^{-1} . Occasionally, we shall use the ssd where the k components are the same, but \mathbf{a}^* , \mathbf{b}^* , \mathbf{c}^* , and \mathbf{k} are 2π larger, e.g. k_{Fb} is approximately $(\pi/2)b^{-1} = 0.2844 \text{ \AA}^{-1}$ instead of $(1/4)b^{-1}$.

The most relevant symmetry points have $k_a=0$, and are: $(k_b, k_c)=Z(0, \frac{1}{2})$, $Y(\frac{1}{2}, 0)$, $\Gamma(0, 0)$, $C(\frac{1}{2}, \frac{1}{2})$, $W(\frac{1}{2}, \frac{1}{4})$, $\Lambda(0, \frac{1}{4})$, plus their equivalents. Higher BZs are shifted by reciprocal lattice vectors, which means that k_a , k_b , and k_c are shifted by integers, which we name respectively L , M , and N and shall use in Sect.s IV, V, A 1, and A 2.

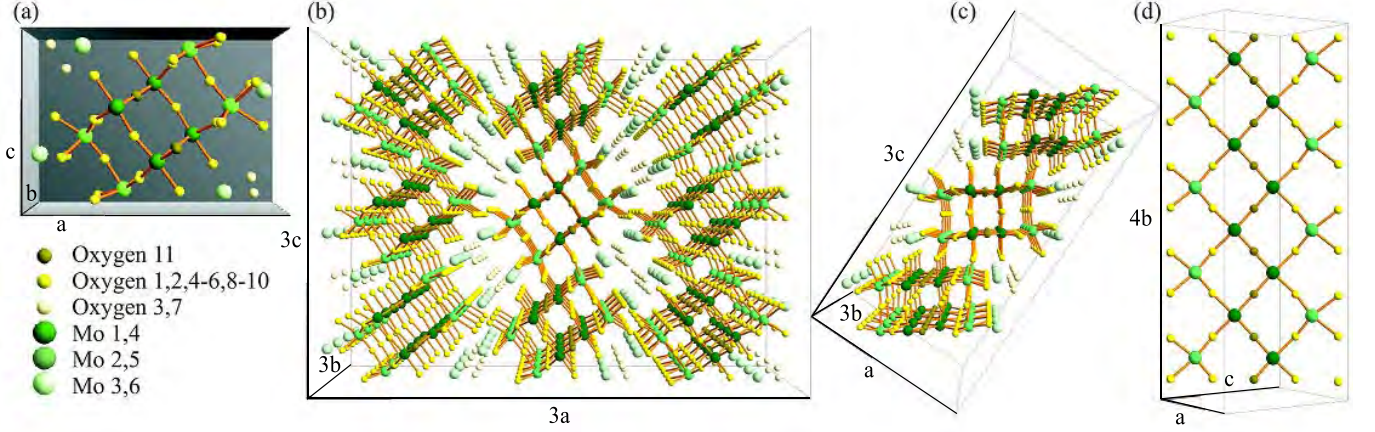


FIG. 1. Crystal structure of $\text{LiMo}_6\text{O}_{17}$. Li (not shown) is intercalated in the hollows near the light-green Mo and light-yellow O atoms. (a) primitive cell spanned by the translation vectors, \mathbf{a} , \mathbf{b} , and \mathbf{c} . Whereas \mathbf{b} is orthogonal to both \mathbf{c} and \mathbf{a} , the latter has a one-per-cent component along \mathbf{c} . The relative lengths of the translation vectors are: $a/b \approx 2.31$ and $c/b \approx \sqrt{3}$. The primitive cell contains two strings: (Mo3) - Mo2 - Mo1 - Mo4 - Mo5 - (Mo6) and the inverted one: (Mo6) - Mo5 - Mo4 - Mo1 - Mo2 - (Mo3). When we need to distinguish between two equivalent sites (related by inversion), we use upper-case letters for the one in the upper string. Together, the two strings form a bi-string. (b) a $3 \times 3 \times 3$ supercell showing bc -slabs translated by $\pm \mathbf{a}$. The slabs are separated by Mo3 and Mo6 (light green). (c) A single slab, rotated such that six-fold coordinated Mo (green and dark green) have their bonds to O in the vertical, z , and two horizontal, x and y , directions. Oriented this way, the slab is seen to form a staircase running up the c -direction. One can recognize horizontal bi-strings which form bi-ribbons by infinitely many \mathbf{b} -translations. A bi-ribbon is a step which through infinitely many \mathbf{c} -translations form the staircase. (d) A single ribbon.

A simplifying –hitherto overlooked– approximate view of the complicated structure in FIG. 1 is that all Mo atoms are on a sublattice spanned by the primitive translations:

$$\frac{\mathbf{c} + \mathbf{a}}{6} \mp \frac{\mathbf{b}}{2} \equiv \frac{\mathbf{x}}{\mathbf{y}} \quad \text{and} \quad \frac{2\mathbf{c} - \mathbf{a}}{6} \equiv \mathbf{z}. \quad (8)$$

These are orthogonal to within a few degrees and their lengths, 3.82\AA , are equal to within 0.3%. This means that all Mo atoms approximately form a cubic lattice. In FIG. 1(c), the structure is turned to have \mathbf{z} in the vertical direction, and \mathbf{x} and \mathbf{y} in the horizontal plane.

As specified in FIG. 1(a) and seen in (b)-(d), of the twelve Mo sites in the primitive cell, six are inequivalent. Four of these (dark green Mo1 and Mo4, and green Mo2 and Mo5) are six-fold coordinated in the $\pm x$, $\pm y$, and $\pm z$ directions with O (dark yellow and yellow) and form a network of *corner-sharing* MoO_6 octahedra. The remaining two types of Mo (light green Mo3 and Mo6) are four-fold coordinated with O (yellow and light yellow). The latter, tetrahedrally coordinated Mo atoms (light green, set in parentheses in the following) form double layers perpendicular to \mathbf{a} , which separate the network of corner-sharing MoO_6 octahedra into *slabs*.

Such a slab has the form of a *staircase* with steps of *bi-ribbons* stacked with period \mathbf{c} as seen in (c). Schemat-

ically, this is:

$\begin{matrix} \mathbf{c} & \nearrow \\ \mathbf{a} & \searrow \\ \mathbf{z} & \uparrow \end{matrix}$	2	1	4	5	2	1	4	
	1	2			5	4	1	2
	4	5			2	1	4	5
					5	4	1	2
					2	1	4	5
	5	4	1	2	5	4	1	
	2	1	4	5	2	1	4	

where the octahedral molybdenums lying in the same ac -plane, separated by $\mathbf{b}/2$, are either normal- or bold-faced. A *single ribbon* is four octahedral molybdenums wide and, as seen in (a) and (d), lies in the horizontal xy -plane containing the vectors $\mathbf{c} + \mathbf{a} = 3(\mathbf{x} + \mathbf{y})$ and $\mathbf{b} = \mathbf{y} - \mathbf{x}$, and extends indefinitely in the b -direction. The lower half of a bi-ribbon consist of (Mo3) - Mo2 - Mo1 - Mo4 - Mo5 - (Mo6) *strings* separated by \mathbf{b} and can be taken either (see (a)) as a zigzag line changing translation between \mathbf{y} and \mathbf{x} and thus running along $\mathbf{c} + \mathbf{a}$, or as a nearly straight line running along \mathbf{x} , or as one running along \mathbf{y} (see (d) and the picture below). In the following, we shall refer to these as respectively $(\mathbf{c} + \mathbf{a})$ -zigzag, \mathbf{x} -, and \mathbf{y} strings. Such a ribbon is as shown schematically below

to the left:

$$\begin{array}{c}
 \mathbf{b} \\
 \mathbf{c} + \mathbf{a} \\
 \mathbf{y} \\
 \mathbf{x}
 \end{array}
 \begin{array}{c}
 \uparrow \\
 \rightarrow \\
 \nearrow \\
 \searrow
 \end{array}
 \begin{array}{|c|c|}
 \hline
 2 & 4 \\
 \hline
 1 & 5 \\
 \hline
 2 & 4 \\
 \hline
 1 & 5 \\
 \hline
 \end{array}
 \begin{array}{|c|c|}
 \hline
 5 & 1 \\
 \hline
 4 & 2 \\
 \hline
 5 & 1 \\
 \hline
 4 & 2 \\
 \hline
 \end{array}$$

The upper half of the bi-ribbon, lying \mathbf{z} above the lower half, is shown to right. Its Mo sequence, (MO6) - MO5 - MO4 - MO1 - MO2 - (MO3), is *inverted* such that e.g. MO4 is on top of Mo1. Note that when we need to distinguish between two equivalent sites (related by inversion), we use upper-case letters for the one in the upper ribbon. The vectors from Mo1 to its two nearest MO1 neighbors inside the same bi-ribbon, are:

$$\mathbf{R} \equiv -0.012\mathbf{a} + 0.5\mathbf{b} + 0.467\mathbf{c}. \quad (9)$$

These vectors are not too far from *half* the translation vectors $\mathbf{c} \pm \mathbf{b}$ to a nearest Mo1 in the next bi-ribbon, whereby the intra and inter bi-ribbon vectors are nearly the same.

Due to the stacking into a staircase of bi-ribbons, Mo4 and Mo5 differ from respectively Mo1 and Mo2 by having *no* neighbor belonging to the next bi-ribbon, i.e. they have only *one* octahedral Mo neighbor along \mathbf{z} .

It may be noted that the sequence along the vertical, almost straight lines along \mathbf{z} is: (MO6) - Mo5 - MO2 - Mo1 - MO4 - (Mo3) and that Li, which is not shown in FIG. 1, intercalates between the Mo₃O₄ tetrahedron and the MO₃O₄ tetrahedron right above it [9].

The midpoint between Mo1 and a nearest MO1 in the same bi-ribbon is a center of inversion. The planes perpendicular to \mathbf{b} containing Mo1 and Mo5, as well as those containing Mo4 and Mo2, are mirror planes.

B. Basic electronic structure

In FIG. 2 we show the LDA energy bands over a range of ± 9 eV around the Fermi level together with their density of states projected onto O (green) and onto tetrahedrally- (blue) and octahedrally- (red) coordinated Mo. The bands between -8 and -2 eV have predominantly O $2p$ character and those extending upwards from -0.7 eV have predominantly Mo $4d$ character and, at high energies, Mo $5s$ and $5p$ characters. The states in the O $2p$ band are bonding linear combinations with Mo $5s$, $5p$, and $4d$ orbitals, the more bonding, the lower their energy. The states in the Mo $4d$ band are antibonding linear combinations with O $2s$ and $2p$ orbitals, the more antibonding, the higher their energy.

The 2 eV gap between the O $2p$ -like and Mo $4d$ -like bands is –for the purpose of counting– ionic with Li donating one and Mo six electrons to and O acquiring two electrons from the Mo $4d$ -like bands above the gap, which thereby hold $2(1 + 6 \times 6 - 17 \times 2) = 6$ electrons

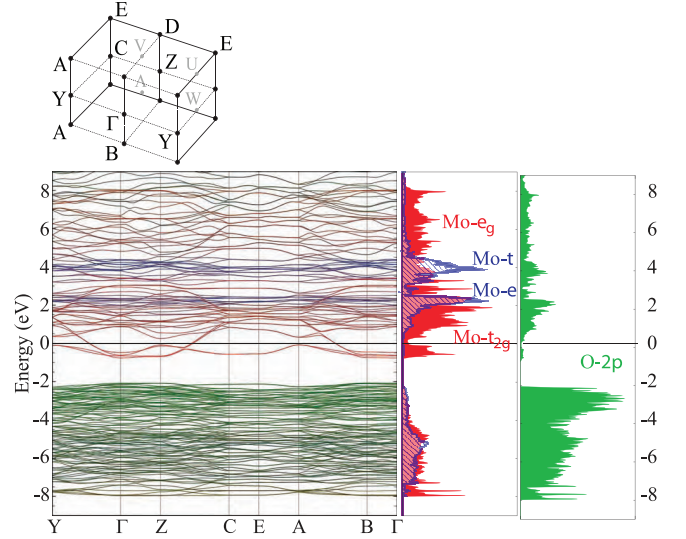


FIG. 2. The top shows half ($k_c \geq 0$) the (1st) Brillouin-zone of LiMo₆O₁₇ with the labeling of the symmetric points for P2₁/m obtained from the Bilbao crystal server [67]. Below is the LDA band-structure (left) with its partial densities of states (right) over a wide energy range. The zero of energy is the Fermi level of the stoichiometric compound.

per 2(LiMo₆O₁₇). Had this charge been spread uniformly over all molybdenums, this would correspond to a Mo $d^{0.5}$ occupation.

The $4d$ orbitals forming the most antibonding and bonding states with O are the e_g orbitals, $3z^2 - 1$ and $x^2 - y^2$, on octahedrally coordinated Mo because their lobes point respectively *towards* the two O neighbors along \mathbf{z} and the four O neighbors in the xy plane and thereby form $pd\sigma$ bonds and anti-bonds. Not only the e_g orbitals on octahedrally coordinated Mo, but all $4d$ orbitals (t and e) on tetrahedrally coordinated Mo form filled bonding and empty antibonding states with their O neighbors, and thereby contribute to the stability of the crystal. However, as seen from the projected densities of states in FIG. 2, none of them contribute to the LDA bands within an eV around the Fermi level, which are the ones of our primary interest. So as long as there are no additional perturbations or correlations with energies in excess of this, which is assumed in the $\frac{1}{2}$ -filled models, the Mo t and e orbitals are uninteresting for the low-energy electronics, and so are the Li $2s$ orbitals which only contribute to bands several eV above the Fermi level.

Although the MoO₄ tetrahedra do not contribute any electrons near the Fermi level, their arrangement in double layers perpendicular to \mathbf{a} , separating the staircases of corner-sharing octahedra, has an important impact on the low-energy electronic structure: It suppresses the hopping between the low-energy orbitals, across the double layer, to the extent that we shall neglect it in our TB model for the six lowest bands [68].

The remaining $4d$ orbitals on octahedrally coordinated Mo are the t_{2g} orbitals, xy , xz , and yz , whose lobes

point *between* the four O neighbors in respectively the xy , xz , and yz planes and therefore form relatively weak $pd\pi$ bonds and antibonds, e.g. $\text{Mo } xy \pm \text{O } y$ on the $\mathbf{x}/2$ bond. Whereas the bonds are dominated by oxygen and form bands which are part of the O $2p$ continuum below about -4 eV, the antibonds are dominated by Mo and form $4 \times 2 \times 3 = 24$ bands which extend from $+3.0$ eV down to the bottom of the Mo $4d$ continuum at -0.8 eV. This spread in energy is conventionally described as due to hopping between *dressed* $\text{Mo } t_{2g}$ orbitals, where the dressing consists of the $pd\pi$ antibonding tails on the four oxygens in the plane of the orbital. Since the dressed orbitals are planar, the strongest hoppings are between *like* t_{2g} orbitals which are nearest neighbors in the same plane; these hoppings are $dd\pi$ -like.

An example is shown in the right-hand panel of FIG. 3 which, apart from being the xy WO to be described in the next section, is approximately that $|k_b| = \frac{1}{4} \sim k_F$ standing-wave state of the xy band which behaves like $\cos \frac{\pi}{2} r_b$, i.e. is even around the $\mathbf{c} + \mathbf{a}$ line through Mo1 and Mo5 and has nodes at the Mo1-Mo5 lines translated by $\pm \mathbf{b}$ (see Sect. III A). We see that the amplitude of the dressed xy orbitals is largest at Mo1 and that the signs of the dressed orbitals on the four nearest neighbors (Mo4 at \mathbf{x} and \mathbf{y} , and Mo2 at $-\mathbf{x}$ and $-\mathbf{y}$) are antibonding (nearest-neighbor lobes have different colors). This is the reason why the overlap from the neighboring dressed xy orbital weakens the O y (or x) amplitude on the common oxygen such that its contour merges with that of the weaker Mo neighbor. Hence, O p is $pd\pi$ antibonding with Mo1 xy and bonding with Mo4 xy and Mo2 xy . The result is essentially $pd\pi$ non-bonding.

If we then imagine going to the xy state with $|k_b| = \frac{3}{4} = \frac{1}{4} [\text{mod } \frac{1}{2}]$ and energy ~ 2.3 eV above E_F , i.e. the state in the next xy band, the signs (colors) of the dressed xy orbitals on the four neighbors will have changed, whereby the overlaps on the common oxygens will have their amplitudes enhanced. Now, the O y (or x) contour will be separated by a node not only from the stronger Mo1- xy contour, but also from the weaker Mo4 (or Mo2) xy contour. In the following we shall refer to the t_{2g} band with the lower/higher energy as the bonding/antibonding band although both of these $pd\pi$ bands are $pd\pi$ non- or anti-bonding, but the one with the higher energy has more $pd\pi$ nodes.

The dressed xy orbitals lie in the plane of a ribbon with nearest neighbors along $\pm \mathbf{y}$ and $\pm \mathbf{x}$. Hence, their $dd\pi$ -like hopping integral is the largest ($\tau \sim -0.8$ eV) and the xy orbitals on the infinite zigzag chain, $\overset{\mathbf{y}}{\leftarrow} \text{Mo1} \overset{\mathbf{y}}{\rightarrow} \text{Mo4} \overset{\mathbf{x}}{\leftarrow} \text{Mo5} \overset{\mathbf{x}}{\rightarrow} \text{Mo2} \dots$, with pseudo translation $(\mathbf{y} - \mathbf{x})/2 = \mathbf{b}/2$ form the well-known quasi-1D band with dispersion [69]:

$$\varepsilon_{xy}(\mathbf{k}) \sim 2\tau \cos \left(2\pi \frac{\mathbf{k} \cdot \mathbf{b}}{2} \right) = 2\tau \cos \pi k_b. \quad (10)$$

Remember that τ is negative. Since \mathbf{b} , and not $\mathbf{b}/2$, is a lattice translation, the band must be folded from the large pseudo-BZ bound by the midplanes to the

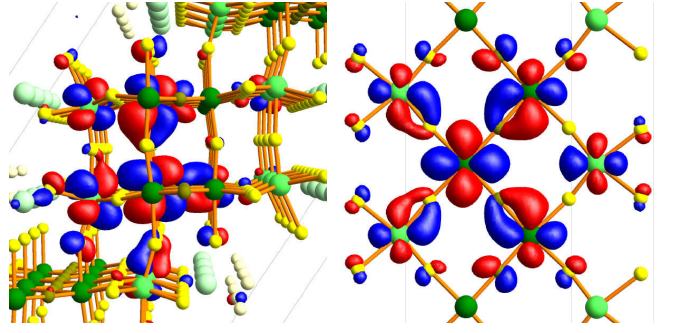


FIG. 3. The yz (left) and xy (right) Mo1-centered WOs (see Sect. IV A) which belong to the *set of six* t_{2g} WOs describing the six lowest Mo $4d$ -like bands above the pd gap (see FIGs.4-6). The yz and xy WOs are viewed along respectively \mathbf{b} as in FIG. 1(c) and along $-\mathbf{z} \sim \mathbf{a} - \mathbf{c}$ as in (d). The positions and numberings of the octahedrally coordinated Mo atoms are described in Sect. III A and shown in FIG. 6. The contour contains 70% of the WOs charge and the color indicates the sign of the lobe. The WO cut-off contour is usually chosen higher, e.g. at 90% for the t_{2g} bands in NiO [58]. But in LiPB this choice would lead to obscurely large overlaps because the t_{2g} WOs are spread over more atoms.

reciprocal-lattice vectors, $\pm 2\mathbf{b}^*$, into the proper, small BZ bound by the midplanes to $\pm \mathbf{b}^*$, whereby it becomes $-2\tau \cos \pi k_b$. An equivalent prescription—more useful than BZ-folding as we shall see for the xz and yz bands—is to say that if \mathbf{k} must be limited to the proper, small BZ, then we must also consider the band translated by the proper reciprocal lattice vector:

$$\varepsilon_{xy}(\mathbf{k} + \mathbf{b}^*) \sim 2\tau \cos [\pi (k_b + 1)] = -2\tau \cos \pi k_b.$$

Finally, the *inequivalence* of (or dimerization *into*) Mo1 and Mo4, couples the $xy(\mathbf{k})$ and $xy(\mathbf{k} + \mathbf{b}^*)$ bands, and where they cross—which is for $|k_b| = \frac{1}{2}$, i.e. at the boundaries of the proper BZ (the YCEA planes in FIG. 2)—they are gapped in the middle by ± 0.4 eV. Since this gap is relatively large, the $xy(\mathbf{k})$ band is bonding and the $xy(\mathbf{k} + \mathbf{b}^*)$ band antibonding between Mo1 and Mo4 for \mathbf{k} inside the proper BZ. The latter, high-energy xy band, we shall usually neglect.

Degenerate with the Mo1-Mo4 bonding and antibonding xy bands running along the lower ribbon are MO1-MO4 bonding and antibonding XY bands running along the upper ribbon. Their $|k_b| = \frac{1}{4} \sim k_F$ standing-wave state looks like the one shown on the right-hand side of FIG. 3, but is inverted around \mathbf{R} (9), and may be seen in the second panel of FIG. 6. The xy and XY states viewed along \mathbf{b} are also shown in this figure, from where we realize that these flat, parallel states are well separated onto ribbons, with no contribution on the oxygens in between. The $dd\delta$ -like hops [28] between the xy and XY orbitals inside the same bi-ribbon ($t_1 + u_1 \sim -14$ meV) and between the XY and xy orbitals in different bi-ribbons ($t_1 - u_1 \sim -8$ meV), give the bands a perpendicular k_c -dispersion, which is two orders of magnitude smaller

than the k_b -dispersion given by Eq. (10). If all ribbons were translationally equivalent, i.e. if the primitive translations were $\mathbf{x} + \mathbf{z} = (\mathbf{c} - \mathbf{b})/2$ and $\mathbf{y} + \mathbf{z} = (\mathbf{c} + \mathbf{b})/2$ with reciprocal-lattice translations $\mathbf{c}^* - \mathbf{b}^*$ and $\mathbf{c}^* + \mathbf{b}^*$, the $dd\delta$ hopping would add

$$2t_1 [\cos \pi (k_c - k_b) + \cos \pi (k_c + k_b)] = 4t_1 \cos \pi k_b \cos \pi k_c$$

to $\varepsilon_{xy}(\mathbf{k})$. But since the primitive translations are really \mathbf{b} and \mathbf{c} , we must –if we want to confine \mathbf{k} to the proper BZ– add also the equivalent term translated by \mathbf{c}^* (which differs from $\mathbf{c}^* \pm \mathbf{b}^*$ by merely a reciprocal lattice vector). As a result:

$$\varepsilon_{xy} \left(\begin{smallmatrix} \mathbf{k} \\ \mathbf{k} + \mathbf{c}^* \end{smallmatrix} \right) \sim 2\tau [1 \pm (2t_1/\tau) \cos \pi k_c] \cos \pi k_b. \quad (11)$$

As long as \mathbf{k} is inside the 1st BZ ($|k_c| \leq \frac{1}{2}$), the $xy(\mathbf{k})$ band is bonding and the $xy(\mathbf{k} + \mathbf{c}^*)$ band antibonding between ribbons, i.e. between xy and XY . In the 2nd BZ ($|k_c - 1| \leq \frac{1}{2}$), the opposite is true. The translational inequivalence of the two ribbons –i.e. the dimerization into bi-ribbons– finally splits the degeneracy of the $xy(\mathbf{k})$ and $xy(\mathbf{k} + \mathbf{c}^*)$ bands at the BZ boundaries $|k_c| = \frac{1}{2}$ (the ZCED planes) by $\pm 2\sqrt{2}u_1 \cos \pi k_b$.

In the planes perpendicular to the bi-ribbons and cutting them along the \mathbf{x} -strings, lie the dressed xz orbitals, and in the planes cutting along the \mathbf{y} -strings, lie the dressed yz orbitals (left-hand panel of FIG. 3). Whereas the xy orbitals on Mo1 and Mo4, as well as –due to the inversion symmetry around \mathbf{R} (9)– the XY orbitals on MO1 and MO4, are nearly equivalent, the yz orbitals on Mo1 and the YZ orbitals on MO1 are *special* because Mo1 and MO1 are the only octahedral molybdenums which in the yz plane have 4 octahedral Mo-neighbors. Due to the stacking into a staircase of bi-ribbons, Mo4, MO4, Mo2, and MO2 have only 3 octahedral neighbors, and Mo5 and MO5 have merely 2. As a result, the yz and YZ orbitals on the Mo1- and MO1-sharing zigzag chains, $\overset{\text{Mo2}}{\text{Mo1}} \xrightarrow{\text{y}} \text{Mo1} \xrightarrow{\text{z}} \text{MO4} \xrightarrow{\text{y}} \text{MO1} \xrightarrow{\text{z}} \text{Mo1} \xrightarrow{\text{y}} \text{Mo4} \xrightarrow{\text{z}} \text{MO1} \xrightarrow{\text{y}} \text{MO2} \xrightarrow{\text{z}}$, running up the staircase with pseudo translation $\mathbf{y} + \mathbf{z} = (\mathbf{c} + \mathbf{b})/2$ form a quasi-1D band dispersing like:

$$\varepsilon_{yz}(\mathbf{k}) \sim 2A_1 \cos \left(2\pi \mathbf{k} \cdot \frac{\mathbf{c} + \mathbf{b}}{2} \right) \sim 2A_1 \cos \pi (k_c + k_b), \quad (12)$$

with an effective hopping integral, $A_1 \sim -0.3 \text{ eV}$, numerically smaller than $\tau/2$ [28]. Similarly, the xz and XZ orbitals on the infinite zigzag chains with pseudo translation $\mathbf{x} + \mathbf{z} = (\mathbf{c} - \mathbf{b})/2$ form a quasi-1D band dispersing like:

$$\varepsilon_{xz}(\mathbf{k}) \sim 2A_1 \cos \left(2\pi \mathbf{k} \cdot \frac{\mathbf{c} - \mathbf{b}}{2} \right) = 2A_1 \cos \pi (k_c - k_b), \quad (13)$$

What is shown in the left-hand panel of FIG. 3 is approximately the Mo1-centered part of that $|k_c + k_b| = \frac{1}{2}$ standing-wave state of the yz band which behaves like

$\cos \pi (r_c + r_b)$, i.e. is even around Mo1 and vanishes in the MO1-containing planes which are perpendicular to $\mathbf{c}^* + \mathbf{b}^*$. Like for xy , the amplitudes of the dressed yz orbitals are seen to be largest at Mo1 and the sign at the four nearest neighbors (MO4 at \mathbf{z} , Mo4 at \mathbf{y} , Mo2 at $-\mathbf{y}$, and MO2 at $-\mathbf{z}$) are seen to be antibonding with it. Here again, the amplitudes at the two Mo4 are larger than at the two Mo2. Degenerate with this state is the one inverted in \mathbf{R} (9) and the hopping integral A_1 is the effective one between the two states. But because the hopping between ribbons, xz - XZ or yz - YZ , proceeds via Mo4 inside the bi-ribbon and via Mo2 between bi-ribbons, the corresponding hopping integrals are different, respectively $A_1 + G_1 \sim -0.4 \text{ eV}$ and $A_1 - G_1 \sim -0.2 \text{ eV}$.

Since $(\mathbf{c} - \mathbf{b})/2$ is not a lattice translation, but \mathbf{c} is one, the $xz(\mathbf{k} + \mathbf{c}^*)$ band with dispersion

$$\varepsilon_{xz}(\mathbf{k} + \mathbf{c}^*) \sim -2A_1 \cos \pi (k_c - k_b) \quad (14)$$

is equivalent with the $xz(\mathbf{k})$ band, and where they cross, i.e. for $|k_c - k_b| = \frac{1}{2}$, the *translational inequivalence* of the lower and upper ribbons –i.e. the dimerization into bi-ribbons– makes the bands gap by $4|G_1| \sim 0.4 \text{ eV}$, i.e. by 30% of the bandwidth, whereby they become

$$\varepsilon_{xz} = \pm \sqrt{[2A_1 \cos \pi (k_c - k_b)]^2 + [2G_1 \sin \pi (k_c - k_b)]^2}. \quad (15)$$

For \mathbf{k} between the $|k_c - k_b| = \frac{1}{2}$ planes, the $xz(\mathbf{k})$ and $xz(\mathbf{k} + \mathbf{c}^*)$ bands are respectively bonding and antibonding between neighboring ribbons.

Equivalently, the 1D $yz(\mathbf{k})$ and $yz(\mathbf{k} + \mathbf{c}^*)$ bands, dispersing like respectively $+$ and $-2A_1 \cos \pi (k_c + k_b)$, gap by $4G_1$ where they cross, i.e. where $|k_c + k_b| = \frac{1}{2}$. These $yz(\mathbf{k})$ and $yz(\mathbf{k} + \mathbf{c}^*)$ bands are respectively bonding and antibonding between neighboring ribbons for \mathbf{k} between the $|k_c + k_b| = \frac{1}{2}$ planes. Note that neither of the ZYAD-planes, $|k_c \mp k_b| = \frac{1}{2}$, are BZ boundaries. Nevertheless, together with $\pm \mathbf{b}^*/2$, each pair may be taken as a zone boundary for respectively the xz band and the yz band, as we shall explain in Sect. IV D.

From now on we shall usually disregard the upper 18 (=24-6) t_{2g} bands which are more antibonding than the 6 low-energy bands along respectively a $\mathbf{c} + \mathbf{a}$ zigzag, an \mathbf{x} , or a \mathbf{y} string and have energies in the 0.6-3.0 eV range above the Fermi level (FIG. 2).

The bottom of the degenerate xz and yz bands and that of the degenerate xy bands are all at $\Gamma(\mathbf{k}=\mathbf{0})$ and the energy (B) of that linear combination of the dressed xz , yz , or xy orbitals which is least antibonding between all octahedrally coordinated molybdenums. As seen in FIG. 2, $B \sim -0.7 \text{ eV}$ for all 4 bands. Since the $4A_1$ -width of the xz and yz bands is only about one third the 4τ -width of the xy bands, the $4G_1$ -gap halfway up in the xz and yz bands, extending from $B + 2|A_1 - G_1| \sim -0.3 \text{ eV}$ to $B + 2|A_1 + G_1| \sim 0.1 \text{ eV}$, is lined up with the Fermi level in the quarter-filled xy bands, i.e. in the half-filled, lower xy bands. This LDA low-energy t_{2g} band

structure, $E_m(k_b, k_c)$, is shown together with its Fermi level in FIG. 4.

In summary, since the 6 lowest bands are t_{2g} like, the 6 electrons would half fill them in case of weak Coulomb correlations, thus corresponding to a t_{2g}^3 configuration. Covalency between the xz and XZ orbitals, as well as between the yz and YZ orbitals, together with the availability of one xz and one yz electron per string, result in the covalent bonds which dimerize the ribbons into bi-ribbons and thereby gap the xz and yz bands into filled bonding and empty antibonding bands. The remaining one xy electron per string finally half fills the quasi-1D band dispersing strongly along \mathbf{b} .

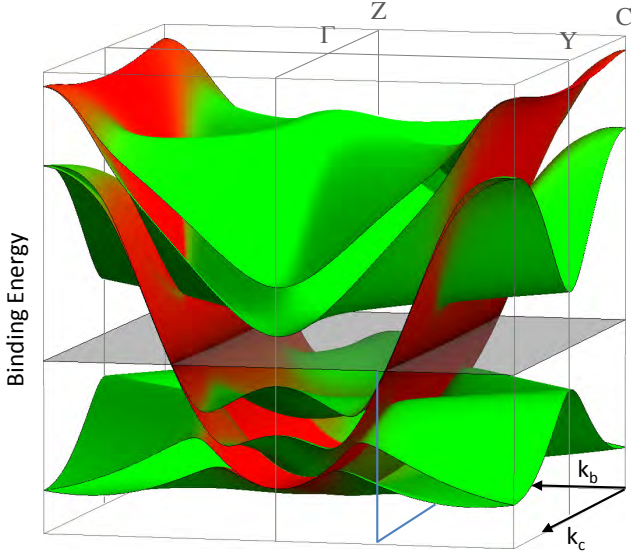


FIG. 4. LDA t_{2g} energy band structure and Fermi level at half filling. Red and green colors indicate respectively xy and xz/yz characters. The energy region is from 0.8 eV below to 1 eV above E_F (see FIG. 2) and the \mathbf{k} -space region is the BZ (see FIG. 5). The LDA TB parameters listed in Tables (A8)-(A12) in the Appendix were used.

FIG. 5 shows the double zone, $|k_b| \leq \frac{1}{2}$ and $|k_c| \leq 1$, and –schematically– the straight-line constant-energy contours (CECs) for the degenerate $xy(\mathbf{k})$ and $xy(\mathbf{k} + \mathbf{c}^*)$ bands (green), the $xz(\mathbf{k})$ bands (blue), and the $yz(\mathbf{k})$ (red) bands. The bottoms of these four bands are along respectively the green, blue and red lines passing through $\Gamma(0,0)$. The top of the degenerate xy bands is along the BZ boundary $|k_b| = \frac{1}{2}$ (green) and the tops of the $xz(\mathbf{k})$ and $yz(\mathbf{k})$ bands are along respectively the blue and red lines through passing through $\Gamma'(0, \pm 1)$. For the degenerate xy bands, we also show the CECs for three energies close to the Fermi level corresponding to half-filling (green dot-dash), 10% hole- (brown dot-dash), and 10% electron (olive dot-dash) doping. For the gapped $xz(\mathbf{k})$ and $xz(\mathbf{k} + \mathbf{c}^*)$ bands we show the coinciding CECs for the valence- and conduction-band edges (blue dot-dash), and similarly for the yz -band edges (red dot-dash). The CECs for the $xz(\mathbf{k} + \mathbf{c}^*)$ and $yz(\mathbf{k} + \mathbf{c}^*)$

bands of course equal those for respectively the $xz(\mathbf{k})$ and $yz(\mathbf{k})$ bands, but translated along k_c by an odd integer. FIG. 4 shows the LDA t_{2g} band structure in the single BZ, $|k_b| \leq \frac{1}{2}$ and $|k_c| \leq \frac{1}{2}$, and FIG. 9 compares the LDA and experimental APPEs CECs for the occupied bands.

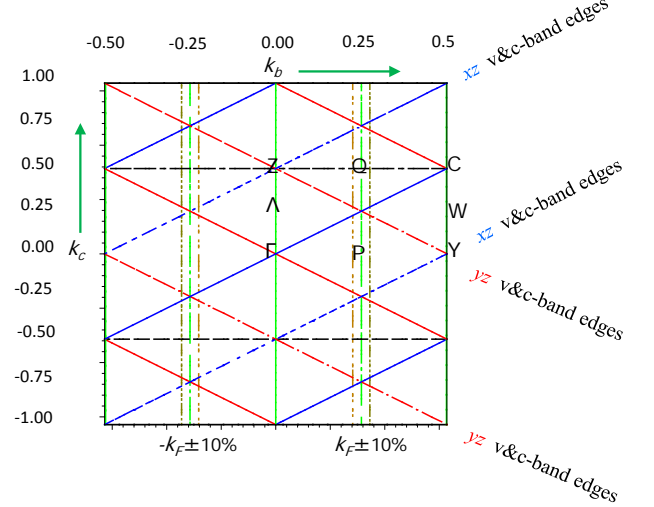


FIG. 5. The double zone: $-0.5 < k_b \leq 0.5$ and $-1 < k_c \leq 1$. The BZ is limited by the black dashed lines and has $-0.5 \leq k_c \leq 0.5$. The irreducible BZ has $0 \leq k_c \leq 0.5$. The green, blue, and red straight lines are schematic constant-energy contours (CECs) of respectively the xy , xz , and yz bands. LDA and ARPES CECs may be seen in FIG. 9. Full lines correspond to energies at the minimum or maximum of the corresponding band and dot-dashed lines to energies at half filling. See text.

As hinted by FIG. 9, the xy bands in the gap hybridize with the xz and yz valence-band edges running along $|k_c \mp k_b| = \frac{1}{2}$ (ZY and ZY') thus causing resonance “fingers” pointing towards Z in the inner sheets of the quasi-1D FS, $|k_b| = k_F \sim \frac{1}{4}$. Hybridization with the remote xz and yz bands reduces the $dd\delta$ -like splitting (11) between the inner and outer sheets near $k_c=0$ (ΓY) and $k_c=1$ ($\Gamma' Y'$) to become almost a crossing. Hybridization with the xz and yz conduction bands finally makes the outer FS sheets bulge outwards around the BZ boundary, $k_c = \frac{1}{2}$ (ΓC). The detailed study of this splitting and perpendicular dispersion of the quasi-1D xy bands near E_F will be the main topic of the present paper.

IV. WANNIER ORBITALS AND HAMILTONIAN

In the previous section, our view moved from the energy scale of the Li $2s$, Mo $5sp4d$, and O $2p$ atomic shells to the decreasing energy scales of Li^+ , Mo^{6+} , and O^{--} ions, to covalently bonded MoO_4 tetrahedra and MoO_6 octahedra and, finally, to the low-energy bands of the MoO_6 octahedra condensed into strings, ribbons, and

staircases by sharing of the $pd\pi$ -bonded O corners. This change of focus from large to small energy scales and, concomitantly, from small to large structures, we followed computationally with the NMTO method in the LDA by using increasingly narrow and fine energy meshes and increasingly sparse basis sets as described in Sect. IIB.

The *six lowest Mo 4d bands*, i.e. those within ± 0.8 eV around the Fermi level, we found to be completely described by the basis set consisting of the xy , xz , and yz NMTOs centered on Mo1 and MO1, i.e. of *one t_{2g} -set per string*, which is per $\text{LiMo}_6\text{O}_{17}$. Symmetrical orthonormalization yielded the corresponding set of WOs whose xy and yz orbitals are what was actually shown in FIG. 3. The centers of the t_{2g} WOs were chosen at Mo1 and MO1 because those are the only octahedral molybdenums whose 6 nearest molybdenum neighbors are also octahedrally surrounded by O. The t_{2g} low-energy band structure was illustrated in FIG. 4.

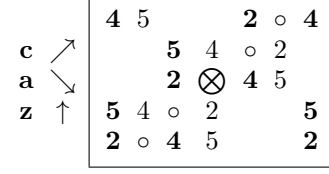
This part of the band structure –rather than one which includes the Mo1-Mo4 antibonding states needed when long-ranged Coulomb correlations are at play– suffices to explain the ARPES dispersions in detail, as we shall demonstrate by comparison with the new $T = 26$ and 6 K ARPES data for energies until 20 meV below E_F (Sect. VI). But first, we shall discuss the WOs and their low-energy TB Hamiltonian, which we shall transform to the $\{\mathbf{k}, \mathbf{k} + \mathbf{c}^*\}$ representation needed to analyze the ARPES data.

A. Low-energy t_{2g} Wannier orbitals (WOs)

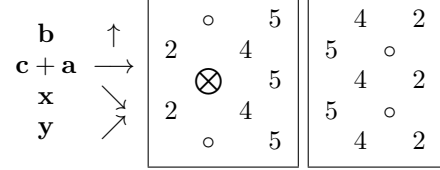
Our set of Wannier functions has been chosen as centered on Mo1 (and MO1) and to have t_{2g} symmetry around that site. This means that a WO spreads out to the 4 nearest octahedral molybdenums in the plane of the orbital and, as described in the previous section, leads to almost half the WO charge being on Mo1, slightly less on Mo4, considerably less on Mo2, and much less on Mo5. There is no discrepancy between the t_{2g}^3 configuration and the Mo $d^{0.5}$ occupancy mentioned at the beginning of Sect. IIIB: The latter is an average over all 6 molybdenums in a string of which only 4 carry t_{2g} partial waves, which are combined into *one* set of t_{2g} WOs, each one being effectively spread onto 3 molybdenums. So the occupation is perhaps more like Mo d^1 .

What *localizes* a t_{2g} NMTO in the set of t_{2g} NMTOs on all Mo1s and MO1s is the boundary condition that its projections onto all t_{2g} partial waves on all Mo1 and MO1, except the own, must *vanish*. On the other hand, the NMTO spreads out onto any *other* partial wave in the crystal in such a way that the NMTO set spans the solutions of Schrödinger's equation for the $N+1$ energies

chosen. This is schematically (see Sect. III A):



and



where \otimes indicates the site (head) of the NMTO, and \circ the sites where all t_{2g} characters vanish, i.e. the sites of the other NMTOs in the basis set. This was explained technically in Sect. IIB.

Our t_{2g} NMTOs are insensitive to the exact orientation chosen for the cartesian system –we took the one given by Eq. (8)– because they have all partial waves *other than xy , xz , and yz* on Mo1 and MO1 downfolded [70]. The contents of these partial waves are thus determined uniquely by the requirement that the NMTO basis set solves Schrödinger's equation exactly at the chosen energies for the LDA potential used to construct the NMTOs. In this way, the downfolding procedure ensures that the shape of t_{2g} orbitals is given by the chemistry rather than by the choice of directions. Specifically, the downfolded content of partial waves with e_g character rotates the directions of the t_{2g} lobes into the proper “chemical” directions [66]. Moreover, the downfolded partial-wave contents on the remaining Mo2, Mo4, and Mo5 atoms in the string ensures that their relative phases are the proper ones for the energies chosen. Also, an NMTO on the upper string is correctly inverted with respect to the one on the lower string. Similarly, the downfolded partial-waves on all oxygens give the proper O $2p$ dressing.

The WOs are obtained by symmetrical orthonormalization of the NMTO set and this causes a delocalization which, however, for our t_{2g} set is small and invisible in FIG. 3. What we do see, and was noted in the previous section, is that each t_{2g} WO has tails with the same t_{2g} character as that of the head on the 4 nearest molybdenums in the plane of the orbital. These tails are connected to the head via $pd\pi$ tails on the 4 connecting oxygens such that the sign is antibonding with the t_{2g} head and bonding with the t_{2g} tail. In effect, this results in a weak $dd\pi$ anti-bond between the oxygen-dressed t_{2g} orbitals forming the WO head and tail.

Since the xy and XY WOs lie *in* the plane of their respective ribbon, they only spread onto a neighboring ribbon via a weak covalent interaction of symmetry $dd\delta$. In contrast to the inter-ribbon $dd\pi$ -spread of the xz , XZ , yz , and YZ WOs seen in FIG. 6 when viewed along \mathbf{b} ,

the $dd\delta$ interaction causes no visible tails on a neighboring ribbon. The consequences for the 6-band Hamiltonian are that the xy - XY inter-ribbon hopping integral t_1 in Eq. (11) and its dimerization u_1 , are about 30 times smaller than the respective xz - XZ inter-ribbon integrals A_1 and G_1 in Eq. (15).

Knowing now, that the right-hand panel of FIG. 3 shows the WO, $xy(\mathbf{r})$, or rather the contour containing 70% of its density, let us imagine building the 1D Bloch sum $xy(k_b\mathbf{b}^*, \mathbf{r})$ of WOs (4) through integer translations by $n\mathbf{b}$, multiplication with $e^{2\pi i n k_b}$, and superposition: Around Mo1 and Mo5, only $xy(\mathbf{r})$ contributes (neglecting the tail outside the 70% contour), but around Mo2 and Mo4, also $xy(\mathbf{r} + \mathbf{b})e^{-2\pi i k_b}$ and $xy(\mathbf{r} - \mathbf{b})e^{2\pi i k_b}$ contribute. As a result, at the bottom of the band, $k_b=0$, the amplitudes around Mo1 and Mo4 are nearly equal and antibonding between Mo1 and Mo4, whereas the amplitude around Mo2 is smaller, but also antibonding to Mo1 so that the $p\pi$ character on all 4 oxygens vanishes. At the Fermi level, $|k_b|=\frac{1}{4}$, whereby the *sum* of the Bloch waves with positive and negative k_b has the same shape as $xy(\mathbf{r})$ near Mo1 and Mo5, and a node at the neighboring Mo1 and Mo5 (i.e. those translated by $\pm\mathbf{b}$). This is the standing-wave state described in the previous section. The shape of the *difference* between the waves with k_b positive and negative is the same, but shifted by \mathbf{b} . At the top of the band, $|k_b|=\frac{1}{2}$, whereby the Bloch waves change sign upon translation by \mathbf{b} so that there is a node through Mo2 and Mo4 for one of the linear combinations, and through Mo1 and Mo5 for the other. If we finally build the Bloch sums with $|k_b|=\frac{3}{4}$, we find that they are identical with those for $|k_b|=\frac{1}{4}$, because in order to form both the low-energy bonding and the high-energy antibonding Mo1-Mo4 states, we would need a set containing two xy WOs, one centered at Mo1 and the other at Mo4. In order for a single WO to describe merely the bonding part near $\frac{1}{4}$ filling of a 4 eV wide band gapped in the middle by a mere 0.8 eV, it must have long range in the direction of the dispersion. For the xy WO, this is not seen in FIG. 3 in the b -direction due to the contour cut-off at 70%, but in the Hamiltonian [Eq.s (A1), (A2), and (A8) in Appendix A], it gives rise to xy - xy hopping integrals, τ_n , which we need to carry to $n=12$.

In a similar way, we can imagine building the states of the two 1D yz bands (12)-(15) from pseudo-Bloch sums of the yz and YZ WOs (FIG.s 3 and 6) through pseudo translations by $n(\mathbf{c} + \mathbf{b})/2$, multiplication with $e^{2\pi i n(k_c + k_b)/2}$, and superposition. These WOs have their proper positions and we use $yz[\mathbf{r} - n(\mathbf{c} + \mathbf{b})/2]$ for n even and $YZ[\mathbf{r} - (n-1)(\mathbf{c} + \mathbf{b})/2]$ for n odd. They are so localized that each one spills over only to its neighboring \mathbf{y} -string, and the integrals for intra and inter bi-ribbon hops, $A_1 \pm G_1$, whose complicated hopping paths between elementary $pd\pi$ orbitals were described above Eq. (12), are simply those between nearest-neighbor yz and YZ WOs. All farther-ranged hopping integrals between yz WOs, $A_{n>1}$ and $G_{n>1}$, which would have been appeared in the Bloch sum A3, are negligible. We shall return to

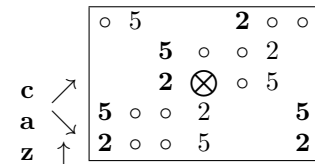
the pseudo Bloch sums in Sect. IV D.

The square of a WO, summed over all lattice translations yields the charge density obtained by filling that band, neglecting its hybridization with the other bands. Summing this charge density over all six WOs yields the charge density obtained by filling all six t_{2g} bands, hybridizations now included. As an example: Squaring the xy WO in FIG. 3 will remove the colors and enhance the density on Mo1 with respect to that on the two Mo4s, and even more with respect to that on the two Mo2s, and mostly with respect to that on Mo5. Translating this charge density by $\pm\mathbf{b}$ and summing, doubles the charge density on Mo4 and on Mo2 due to overlap. As a result, the charge density on Mo1 and Mo4 will be nearly equal and larger than that on Mo2, while the one on Mo5 will be the smallest. This charge density compares well with the one obtained for the quasi-1D band by filling it in a narrow range around the Fermi level by Popovic et al [23] and shown in their FIG. 5 in the plane of the lower ribbon. That their density on Mo2 is smaller than the one on Mo5 is presumably due to an erroneous exchange of their Mo1 and Mo4 labels.

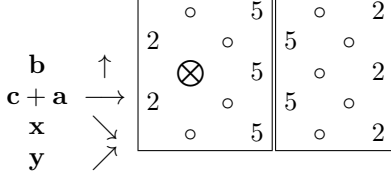
B. Other sets of Wannier-functions (WFs)

Nuss and Aichhorn [39] described merely the 4 lowest bands, i.e. the two xy bands and the xz and yz valence bands with a set of maximally localized WF's obtained numerically by minimizing the spread, $\langle \chi | |\mathbf{r} - \mathbb{R}|^2 | \chi \rangle$. While their yz WF is basically our $yz(\mathbf{r}) + YZ(\mathbf{r})$, and similarly for xz , their xy WF is centered at the bond between Mo1 and Mo4. This WF, shown in their FIG. 4, extends along the zigzag line $\backslash_{\text{Mo1}}/\text{Mo4}\backslash_{\text{Mo1}}/\text{Mo4}\backslash$ with similar-sized contours on all four central Mo sites, with smaller contours on the Mo2 and Mo5 sites closest to bond, and much smaller contours on the next Mo2 and Mo5 sites. This bond-centered WF is extended along the chain, but as judged from the contour plots, it has about the same degree of localization as our disc-shaped xy WO in FIG. 3.

In order to have the possibility of describing a Mott transition due to long-ranged Coulomb correlations causing localization of the xy electron onto the Mo1 or Mo4 sites, one needs a basis set with independent Mo1 and Mo4 xy WF's. For this we would generate a set of 12 NMTOs per cell by putting all three t_{2g} orbitals on all four Mo1 and Mo4 sites and use an energy mesh spanning the t_{2g} bands from -0.8 to 3 eV. In this set of 12, each Mo1-centered WO is schematically:



and



Inversion around \mathbf{R} gives the MO1-centered WO on the upper ribbon. Similarly for the Mo4- and MO4-centered WOs. The Mo1-centered xy WO spills xy character over to the two nearest-neighbor Mo2 sites, but hardly any further, and is therefore very well localized. Similarly, the Mo4-centered xy WO spills a bit of xy character over the two nearest-neighbor Mo5 sites. The yz WOs are very well localized, too: The Mo1-centered yz WO spills yz character over merely to the nearest Mo2 and the nearest MO2 sites. Similarly, the Mo4-centered yz WO spills yz character over merely to the nearest Mo5 and the nearest MO5 sites.

In order to generate a set of *atomically*, i.e. octahedrally, localized t_{2g} WOs, we would need to put a t_{2g} NMTO on each of the 12 octahedrally-coordinated molybdenums and use a 2- or 3-point energy mesh spanning the lowest 4 eV of the Mo d band (see FIG. 2). This set would thus contain 24 WOs per primitive cell.

C. Six-band t_{2g} Hamiltonian

The Hamiltonian (5) in the representation of the six low-energy t_{2g} WOs, is described in App. A 1 and is given by Eq. (A1) together with the definitions (A2)-(A7) and the values of the hopping-integrals in Tables (A8)-(A12) for all distances less than a . This includes the shells of the six 1st, the six 2nd, and the six 3rd nearest neighbors and is consistent with our choice of not including the weak k_a -dispersion. Bloch-summing (4) these hopping integrals yields the six-band TB Hamiltonian whose eigenvalues are the energy bands shown in FIG. 7(a). Due to the truncation of hops longer than a , the effective value of k_a is not 0, but the one for which $\cos 2\pi k_a = 0$, i.e. $\frac{1}{4}$. The truncation also means that our LDA TB bands are a bit more wavy and smoother than those obtained from the original LDA NMTO Hamiltonian downfolded in \mathbf{k} -space.

The hopping integrals given in Tables (A8)-(A12) are far more numerous than those few ($\tau, t_1 \pm u_1, A_1 \pm G_1$ and B) used in the simplified description given above in Sect. IIIB; a description which, nevertheless, suffices to understand the CECs and bands measured by ARPES and shown in respectively FIG.s 9 and 10. The LDA low-energy TB bands shown in FIG. 7(a) have much more detail and their surprisingly good agreement with the bands measured with ARPES for the occupied bands (grey circles and black dots) proves this detail to be real. This

is emphasized by the nearly perfect agreement obtained by shifting merely the on-site energy, τ_0 , of the xy WOs upwards by 100 meV with respect to the energy of the degenerate xz and yz WOs, see FIG. 7(b).

D. $\{\mathbf{k}, \mathbf{k} + \mathbf{c}^*\}$ representation

In connection with Eq.s (10) and (13), we noted that the numerical values of the most important inter-ribbon hoppings have smaller dimerizations than mean values, e.g.: $t_1 \pm u_1 \sim -11 \pm 3$ meV for the xy band and $A_1 \pm G_1 \sim -0.3 \pm 0.1$ eV for the xz and yz bands. If such electronic c -axis dimerizations are neglected, the two strings are translationally equivalent and we can use the pseudo translations $(\mathbf{c} + \mathbf{b})/2$ and $(\mathbf{c} - \mathbf{b})/2$ instead of the proper primitive translations \mathbf{b} and \mathbf{c} . The natural way of describing the electronic structure, i.e. the representation in which the off-diagonal block (A20) of the TB Hamiltonian (A18) is relatively small, is therefore in terms of basis functions which are pseudo Bloch sums of WOs with respect to this –too short– lattice periodicity [66]. Specifically in LiPB, the xy pseudo-Bloch orbital is:

$$|xy; \mathbf{k}\rangle \equiv \frac{1}{\sqrt{2}} \sum_{\mathbf{T}} e^{2\pi i \mathbf{k} \cdot \mathbf{T}} \left[xy(\mathbf{r} - \mathbf{T}) + e^{\pi i \mathbf{k} \cdot (\mathbf{c} + \mathbf{b})} XY(\mathbf{r} - \mathbf{T}) \right], \quad (16)$$

where the T -sum is over the proper lattice translations, xy is the WO on Mo1, and XY the one on MO1. If the XY orbital were equal to the xy orbital translated by $(\mathbf{c} + \mathbf{b})/2$ and not inverted, i.e. if $XY(\mathbf{r}) = xy[\mathbf{r} - (\mathbf{c} + \mathbf{b})/2]$, then the pseudo Bloch sum (16) would be a proper Bloch sum *in the double zone*. Although this is not so –but almost, as seen from FIG. 6,– the pseudo Bloch sum (16) is a periodic function of \mathbf{k} in the *sparse* reciprocal lattice spanned by $\mathbf{c}^* + \mathbf{b}^*$ and $\mathbf{c}^* - \mathbf{b}^*$, i.e.

$$|\mathbf{k}\rangle = |\mathbf{k} + M'(\mathbf{c}^* - \mathbf{b}^*) + N'(\mathbf{c}^* + \mathbf{b}^*)\rangle \equiv |\mathbf{k} + M\mathbf{b}^* + N\mathbf{c}^*\rangle, \quad (17)$$

with M' and N' any integers, which means: with $M + N$ *even*. The correct, long periodicity in real-space can now be described by including in the basis set the pseudo Bloch sum with \mathbf{k} translated to the other sublattice (we may think of reciprocal space as a checkerboard) and finally restricting \mathbf{k} to the proper, small zone. This second set of Bloch waves is thus $|\mathbf{k} + \mathbf{c}^*\rangle$, for which $M + N + 1$ is even, i.e. $M + N$ *odd*. The basis set $\{|xy; \mathbf{k}\rangle, |xy; \mathbf{k} + \mathbf{c}^*\rangle\}$ is simply a unitary transformation of the set $\{xy(\mathbf{k}, \mathbf{r}), XY(\mathbf{k}, \mathbf{r})\}$ of proper Bloch sums (4) of the xy and XY WOs, individually:

$$\begin{aligned} \{|xy; \mathbf{k}\rangle, |xy; \mathbf{k} + \mathbf{c}^*\rangle\} &= \\ \{xy(\mathbf{k}, \mathbf{r}), XY(\mathbf{k}, \mathbf{r})\} &\begin{pmatrix} 1 & 1 \\ e^{\pi i(k_c + k_b)} & -e^{\pi i(k_c + k_b)} \end{pmatrix} \frac{1}{\sqrt{2}}. \end{aligned} \quad (18)$$

We may check that translation of \mathbf{k} by \mathbf{c}^* exchanges the functions on the left-hand side, leaves the proper Bloch

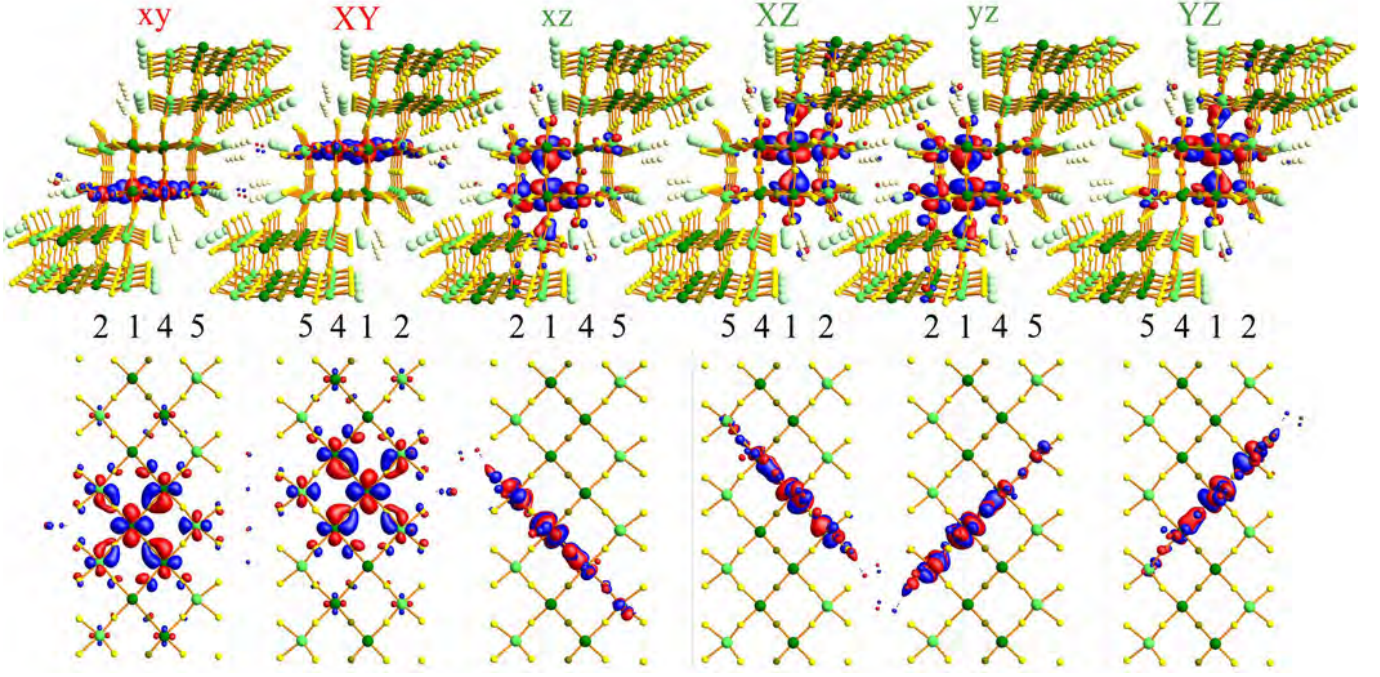


FIG. 6. The six t_{2g} Wannier orbitals (WOs) that span the low-energy band structure of $2(\text{LiMo}_6\text{O}_{17})$ obtained from the LDA NMTO calculation. Shown are constant-density (or amplitude) surfaces containing 70% of the WO charge and the color giving the sign. There is one WO per string and, as shown in FIG. 1(a), two inversion-related strings of corner sharing MoO_6 octahedra per primitive cell. The Mo1-centered WOs, xy , xz , and yz , are on the lower string and the MO1-centered XY , XZ , and YZ WOs are on the upper string. Each of the XY , XZ , and YZ WOs approximately equals the corresponding xy , xz , and yz WO, translated by $(\mathbf{c} + \mathbf{b})/2$. The numbering of the octahedrally-coordinated molybdenums is as in Sect. III A.

functions on the right-hand side invariant, and changes sign for the second row of the matrix, which correctly exchanges its columns. Analogously for $|xz; \mathbf{k}\rangle$ and $|yz; \mathbf{k}\rangle$.

This is the representation used for the TB Hamiltonian (A18)-(A21) in Sect. A 2. The symmetry-breaking terms, e.g. G_1 and u_1 , contained in the off-diagonal block, Δ (A20), mixes the two sets of pseudo Bloch waves. If we neglect this mixing, we can use the extended zone scheme with a double zone centered at Γ ($M'=N'=0$) and being the sum of the 1st and 2nd BZs centered at respectively Γ ($M=N=0$) and Γ ($M=0, N=1$) $\equiv \Gamma'$. But if we include the mixing between $|\mathbf{k}\rangle$ and $|\mathbf{k} + \mathbf{c}^*\rangle$, we must diagonalize the Hamiltonian in the space of the basis functions $|\mathbf{k}\rangle$ and $|\mathbf{k} + \mathbf{c}^*\rangle$. Said differently: we must first translate the double zone by $-\mathbf{c}^*$, i.e. by -1 along k_c , whereby the 2nd BZ ($\frac{1}{2} \leq k_c \leq \frac{3}{2}$) falls on top of the 1st ($-\frac{1}{2} \leq k_c \leq \frac{1}{2}$), and then diagonalize \mathbf{k} restricted to the 1st BZ.

We would like to emphasize that Bloch waves are characterized by their translational symmetry in reciprocal space and that the choice of zone (cell) is arbitrary as long as it contains each \mathbf{k} -point once and only once. It may be convenient to choose the zone compatible with the electronic structure, i.e. such that the gaps occur at the zone boundaries. For the familiar nearly-free-electron model, the best choice is the standard BZ – i.e. the Wigner Seitz cell for the reciprocal lattice – because for a weak pseudopotential we can for $|\mathbf{k}\rangle$ use the

plane wave, $\exp(2\pi i \mathbf{k} \cdot \mathbf{T})$, or an orthogonalized plane wave, in which case the coupling is strong only between $|\mathbf{k}\rangle$, $|\mathbf{k} + \mathbf{G}_1\rangle$, ..., and $|\mathbf{k} + \mathbf{G}_n\rangle$, where $\mathbf{G}_1, \dots, \mathbf{G}_n$ are the shortest, inequivalent reciprocal lattice vectors [66]. For LiPB the situation is different –but even simpler– because rather than being nearly isotropic, the low-energy electrons are quasi 1D in three different directions, one for each t_{2g} symmetry, m , so that we only have two pseudo Bloch waves, $|\mathbf{k}\rangle$ and $|\mathbf{k} + \mathbf{c}^*\rangle$ for each m . Moreover, the “physical” zones are different for the different bands; the zone boundaries are $|k_b| = \frac{1}{2}$ and $|k_c| = \frac{1}{2}$ for the xy bands, $|k_b| = \frac{1}{2}$ and $|k_c - k_b| = \frac{1}{2}$ for the xz bands, and $|k_b| = \frac{1}{2}$ and $|k_c + k_b| = \frac{1}{2}$ for the yz bands. Hence, with the dispersions as described in Sect. III B, the lowest (bonding) m band has $|\mathbf{k}\rangle$ character well inside its zone and $|\mathbf{k} + \mathbf{c}^*\rangle$ character well outside, while the highest (antibonding) band has $|\mathbf{k} + \mathbf{c}^*\rangle$ character well inside and $|\mathbf{k}\rangle$ character well outside. Here, “inside” means where $\Gamma(0,0)$ is located and “outside” means where $\Gamma(0,1)$ or $\Gamma(0,-1)$ is located. While the xy band is half full, the highest xz and yz bands are empty. This physical description will prove useful also for describing the ARPES intensity variations in the following. For the purpose of calculating the electronic structure, i.e. when diagonalizing the 6×6 Hamiltonian (A18) or the Löwdin downfolded 2×2 Hamiltonian (B2), we normally use the rectangular zone: $|k_b| = \frac{1}{2}$, $|k_c| = \frac{1}{2}$, which is –actually– the BZ.

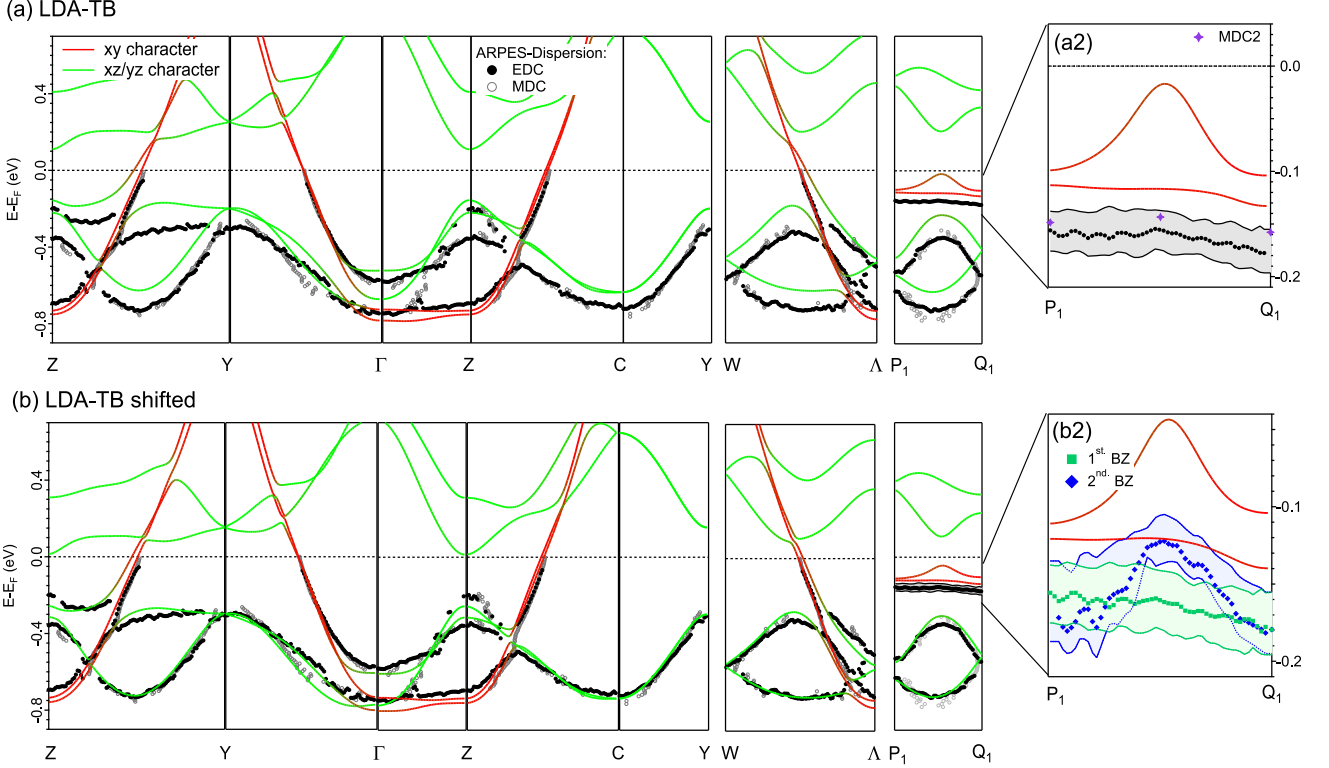


FIG. 7. LDA (xy red and xz/yz green characters) and ARPES (black dots and grey circles) band structures. The line P_1Q_1 has $k_b=0.225$, see FIG.s 5 and 10(a). (a) The LDA bands are the eigenvalues of the six-band TB Hamiltonian defined in App. A 1 with the parameters listed in Tables (A8)-(A12). The Fermi level is pinned to the red xy -like bands and was determined by the effective stoichiometry $\text{Li}_{1.02}$ estimated by ARPES (see App. C), whereby $E_F \approx 0$ which is the common energy of the xz and yz WOs, i.e. the center of the gap. (b) As above, but with the energy of the xy WOs shifted 100 meV upwards. Now $E_F \approx 100$ meV. The experimental dispersion comes from the symmetrized ARPES measurements of sample H ($T=6\text{K}$, $h\nu=30$ eV) displayed in FIG. 10 and was determined by searching the zero in the first derivative either along the momentum direction (MDC, grey circles) or in energy direction (EDC, black dots). The magnifications along P_1Q_1 in (a2) and (b2) –note the different scales– compare the theory with the experimental dispersion determined from (a2) the symmetrized data, or (b2) the individual data coming from respectively the 1st and 2nd BZ. The colored regions indicate the uncertainty. The diamonds, label 'MDC2', indicate the dispersion determined from the momentum direction perpendicular to P_1Q_1 .

V. ARPES INTENSITY VARIATIONS AND ENERGY BANDS

We expect the two xy bands crossing the Fermi level to have by far the largest dispersion along the ribbon, weak dispersion up and down the staircase, weak splitting caused by direct inter-ribbon hopping and by hybridization with the gapped xz and yz bands, and essentially no dispersion with k_a due to the lack of hopping between staircases. In the following, we want to demonstrate that this strong one-dimensionality is indeed confirmed by our ARPES experiment, and also pay attention to strong variations of the ARPES intensity between equivalent zones. These variations will later be exploited to resolve the splitting and warping of the quasi-1D FS. Intensity variations and one-dimensionality are also features of the ARPES xz and yz bands, but of course not near the Fermi level where they are gapped, and not with k_b , but with respectively $k_c - k_b$ and $k_c + k_b$.

A. FS intersection with planes where $k_c=\text{const}$

We begin by showing ARPES for photoelectrons coming from slightly below the Fermi level, i.e. for the xy electrons. FIG. 8 shows as a grey-scale intensity the photoelectron yield in the three a^*b^* -planes indicated at the left. We see the traces of the two FS sheets which separate the occupied states between the sheets ($|\kappa_b| < k_F$) from the empty states outside the sheets ($|\kappa_b| > k_F$). These traces appear as straight lines and are thus consistent with being the intersections of a 1D FS, $|\kappa_b| = k_F \approx \frac{1}{4}$, with an a^*b^* -plane. This FS is periodic in reciprocal space, but has strong intensity variations. That there are two xy bands at E_F –and the FS therefore has two close-lying k_F s which disperse slightly with κ_c and hardly with κ_a (see Eq. (11))– cannot be seen. Here and in the following, we use κ to denote the momentum as measured in ARPES and \mathbf{k} to denote the Bloch vector in the single or the double zone.

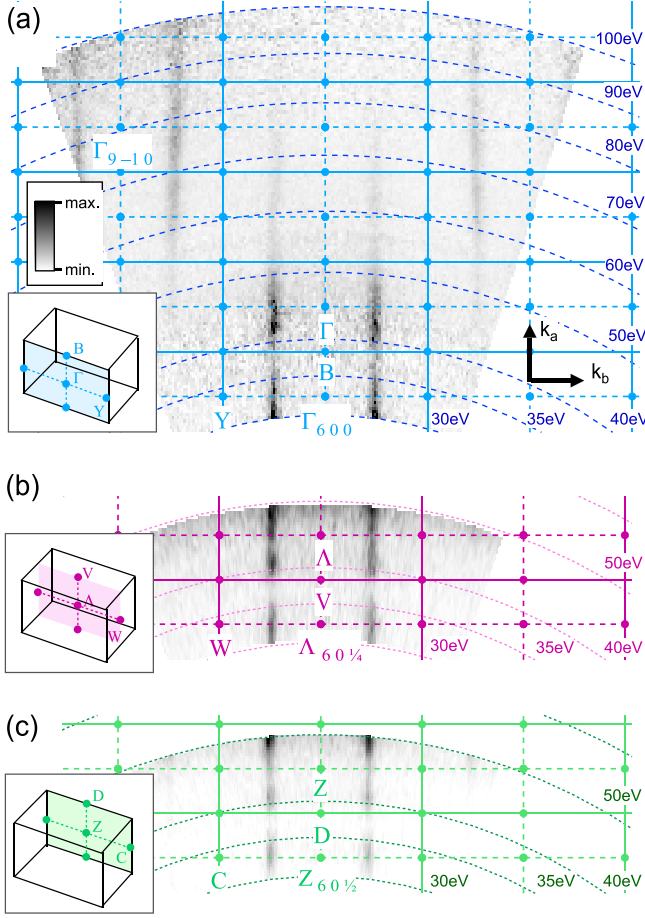


FIG. 8. ARPES FS of sample H at $T = 6\text{K}$ in the a^*b^* -plane: (a) FS map through ΓBY , (b) ΛWV , and (c) ZDC . The vertical lines represent the 1D FS showing no change in the κ_a -direction. There is a "Brillouin-zone selection" effect which makes the ARPES intensity strong/weak near the reciprocal lattice points (L, M, N) for which $M+(L+N)/3$ is even/odd.

The FS yield shown in FIG. 8 is from sample H at $T = 6\text{K}$. FIG. (a) shows the yield in a plane through ΓBY with $\kappa_c=0$. For the orientation within the BZ, see the blue plane on the left. The horizontal axis is along the wave vector κ_b probing the ΓY direction whereas the vertical axis is along the wave vector κ_a in the ΓB direction. The κ_a direction is perpendicular to the cleaving plane of the sample and must therefore be experimentally accessed by variation of the photon energy, $\hbar\nu \sim \hbar(2\pi\kappa)^2/2m + V_0$. For presenting these measurements, we have converted our raw data as a function of angle and photon energy to momentum space, taking the inner potential to be $V_0=6\text{eV}$. With this choice, the reciprocal-lattice point $(L, M, N)=(6, 0, 0)$, denoted Γ_{600} in (a), is reached with $\hbar\nu \sim 32\text{eV}$. In FIG.s 8 (b) and (c), the yields are also shown for planes through ΛWV and ZDC having respectively $\kappa_c=-\frac{1}{4}$ and $-\frac{1}{2}$.

All three FS maps show intensity variations between

equivalent BZs: Strong intensity is seen in a region between Γ_{500} and Γ_{700} , and then again above $\Gamma_{9\pm10}$. Moreover, the maps for $\kappa_c = 0, -\frac{1}{4}$, and $-\frac{1}{2}$ show the intensity to weaken with decreasing κ_c . The intensity variations can be understood along the following lines: As explained in more detail in Refs. 71–73 the photoemission signal includes a so-called photoemission structure factor (PSF), similar to the geometrical structure factor in x-ray diffraction, but depending on the electronic wave functions. A particularly prominent literature example is graphite [74] where the interference pattern formed by photoelectrons coming from the two equivalent C atoms per primitive cell causes a strong zone-selection effect: the same bands appear with different intensity in otherwise equivalent parts of reciprocal space. In LiPB, the two equivalent strings per primitive cell cause similar effects which can be understood more simply because the WOs for the two strings, $XY(\mathbf{r})$ and $xy(\mathbf{r})$ translated to $xy[\mathbf{r} - (\mathbf{c} + \mathbf{b})/2]$, are nearly identical, and similarly for xz and yz . This can be seen in FIG. 6 and was discussed in Sect. IV. Hence, in LiPB the so-called BZ-selection effect is primarily a *sublattice effect* giving rise to orbital-dependent zone-selection. For the xy orbitals, the result to be derived below is that the ARPES intensity is strong or weak around the reciprocal lattice points for which $M + (L + N)/3$ is respectively even or odd, and FIG.s 8 (a), (b), and (c) are consistent herewith. So although the structure of $2(\text{LiMo}_6\text{O}_{17})$ is far more complicated than that of a single sheet of C_2 , the ARPES intensity variations are easier to understand. This will now be explained in more detail:

B. Simple theory of ARPES intensity variations

We start from the expression,

$$I(\kappa, \omega) \propto \sum_j \sum_{\mathbf{k} \in \text{BZ}} \left| \langle e^{2\pi i \kappa \cdot \mathbf{r}} | \mathbf{p} \cdot \mathbf{E} | \psi_j(\mathbf{k}, \mathbf{r}) \rangle \right|^2 \delta[\omega - E_j(\mathbf{k})], \quad (19)$$

for the photoemission intensity in the one-electron approximation with initial-state wave functions $\psi_j(\mathbf{k}, \mathbf{r})$ and energy bands $E_j(\mathbf{k})$ (with respect to E_F). The sum is over all occupied states, $j\mathbf{k}$, with \mathbf{k} in the BZ. For simplicity and lack of knowledge, the final state is taken as a free-electron plane wave, $e^{2\pi i \kappa \cdot \mathbf{r}}$, with energy $\hbar(2\pi\kappa)^2/2m + V_0$, whereby $\omega \equiv \hbar(2\pi\kappa)^2/2m + V_0 - \hbar\nu$. Effects of the surface and the photo-electron escape are thus neglected. For our purpose, it suffices to express the matrix element as:

$$\langle e^{2\pi i \kappa \cdot \mathbf{r}} | \mathbf{p} \cdot \mathbf{E} | \psi_j(\mathbf{k}, \mathbf{r}) \rangle \propto (\kappa_a e_a + \kappa_b e_b + \kappa_c e_c) \sum_{\mathbf{G}} u_j(\mathbf{k}, \mathbf{G}) \delta(\kappa - \mathbf{k} - \mathbf{G}), \quad (20)$$

as obtained by, first of all, operating with $\mathbf{p} \cdot \mathbf{E}$ to the left, and then by pulling the polarization-dependent factor from Eq. (1) outside the integral, exploiting the fact

that the photon wavelength is long compared with inter-atomic distances. Since κ_a is six times larger than κ_b and κ_c , and since also e_a is much larger than e_b and e_c , we can neglect the effect of the polarization.

From the matrix element (20) there remains the Fourier transform of the Bloch function, and this reduces to the sum over the reciprocal lattice points, \mathbf{G} , of an intensity-modulating function, $u_j(\mathbf{k}, \mathbf{G})$, times a delta function. The result for $I(\kappa, \omega)$ is then that the momentum, $\kappa(\omega)$, yields the constant-energy contours (CECs) of the occupied part of the band structure in the periodic zone scheme, but with intensities varying from zone to zone. Here, $u_j(\mathbf{k}, \mathbf{G})$ are the coefficients in the Fourier-series expansion of the periodic part, $e^{-2\pi i \mathbf{k} \cdot \mathbf{r}} \psi_j(\mathbf{k}, \mathbf{r}) \equiv \sum_{\mathbf{T}} u_j(\mathbf{k}, \mathbf{r} - \mathbf{T})$, of the Bloch function, $\psi_j(\mathbf{k}, \mathbf{r})$.

For a *single band* with Wannier function $\chi(\mathbf{r})$, this simplifies to: $u(\mathbf{k}, \mathbf{r}) = \chi(\mathbf{r}) e^{-2\pi i \mathbf{k} \cdot \mathbf{r}}$, and by Fourier transformation to: $u(\mathbf{k}, \mathbf{G}) = \chi(\mathbf{k} + \mathbf{G})$. Here, we denote a function and its Fourier transform, e.g. $\langle e^{2\pi i \mathbf{k} \cdot \mathbf{r}} | \chi(\mathbf{r}) \rangle \equiv \chi(\kappa)$, by the same symbol, χ . As a result, for *independent* (non-hybridizing) bands, the ARPES intensity (19) reduces to:

$$I(\kappa, \omega) \propto \sum_m |\chi_m(\kappa)|^2 \times \int_{BZ} d^3k \sum_{\mathbf{G}} \delta(\kappa - \mathbf{k} - \mathbf{G}) \delta[\omega - E_m(\mathbf{k})]. \quad (21)$$

This means more generally that Eq. (21) describes those parts of the CECs for which inter-band hybridization can be neglected.

This simple result can now be used for LiPB if, as explained in the previous Sect.s III B and IV, we approximate its low-energy band structure by three independent t_{2g} bands ($j \equiv m = xy, xz, yz$), each one periodic in the reciprocal lattice, $\mathbf{G} = L\mathbf{a}^* + M\mathbf{b}^* + N\mathbf{c}^*$, with $M + N$ even. This holds for all three bands, but with band-dependent zones as explained in Sect. IV D. Hence, from this we expect to see the three $|\mathbf{k}\rangle$ -bands in the double zone, and periodically repeated, but blurred and possibly discontinuous near the band-dependent single-zone boundaries, $|k_c - k_b| = \frac{1}{2}$ for xz , $|k_c + k_b| = \frac{1}{2}$ for yz , and $|k_c| = \frac{1}{2}$ for xy . For the equivalent $xz(\mathbf{k})$ and $yz(\mathbf{k})$ bands the intensity should vanish discontinuously when going outside the common part of their physical single zones, because the respective band jumps by $4|G_1|$ at the zone boundary and ends up well above E_F . For the $xy(\mathbf{k})$ band well below E_F , we expect to see the behavior given by Eq. (11) with an tiny, blurred discontinuity $\propto u_1$ at $|k_c| = \frac{1}{2}$. This band remains occupied also in the 2nd zone.

On top of this, there are band-dependent intensity variations from the factor $|\chi_m(\kappa)|^2$ caused by the atomic-scale structure of the t_{2g} WOs on the cubic Mo sublattice (see Eq.8). Specifically, a t_{2g} WO (FIG. 6) has tails with essentially *the same* t_{2g} character as that of its head on primarily the 4 nearest Mo neighbors in the plane of the WO. For the present purpose we can neglect the details

of the oxygen $pd\pi$ antibonding with the head and bonding with the tail; what is important is that the head has a partial-wave shape, $\varphi(r) Y_m(\hat{\mathbf{r}})$, which, multiplied by a factor $\sim 1/4$, is *translated* without change of sign to the four nearest neighbors. This makes the Fourier transform of the WO,

$$\chi_m(\kappa) \propto \mathcal{S}_m(\kappa) Y_m(\hat{\kappa}) \left(\int_0^s r^2 j_2(2\pi\kappa r) \varphi(r) dr \right), \quad (22)$$

factorize into an orbital-dependent structure factor, $\mathcal{S}_m(\kappa)$, times the t_{2g} angular dependence, $Y_m(\hat{\kappa})$, times the Fourier transform of the Mo $4d$ radial function, $\varphi(r)$, limited by the nodes to the antibonding oxygens to a radius $s \approx \frac{1}{2}$ (in units of the Mo-Mo distance, 3.82Å). This last, orbital-independent radial factor has a broad peak around $\kappa \sim \sqrt{3}$ and a node at ~ 2.5 , followed by decaying oscillations. Here, $\sqrt{3}$ is the length of the vector $(\kappa_a, \kappa_b, \kappa_c) = (6, 0, 0)$ (see Eq. (24) or (26)) in the above-mentioned Mo-Mo unit.

For the xy WO, the 4 nearest neighbors are at $(x, y, z) = (\pm 1, 0, 0)$ and $(0, \pm 1, 0)$. As a consequence, its structure factor,

$$\mathcal{S}_{xy}(\kappa) \sim \frac{1}{2} + \frac{1}{4} (\cos 2\pi\kappa_x + \cos 2\pi\kappa_y), \quad (23)$$

is independent of κ_z and as a function of κ_x and κ_y peaks (with value 1) at all 2D points, $\kappa = I\mathbf{x}^* + J\mathbf{y}^*$, of the lattice reciprocal to the Mo sublattice (8). The ARPES intensity variations measured in the planes of the $a^*b^*c^*$ system (such as those in FIG. 8) can now be understood by cutting the structure factor (23) by the appropriate 2D plane, using the transformation:

$$\begin{aligned} 2\kappa_x &= (\kappa_a + \kappa_c)/3 \mp \kappa_b, \text{ and } 2\kappa_z = (2\kappa_c - \kappa_a)/3, \end{aligned} \quad (24)$$

which is the same as Eq. (8). This shows that $\mathcal{S}_{xy}(\kappa)$ peaks with value 1 at the points $\kappa = L\mathbf{a}^* + M\mathbf{b}^* + N\mathbf{c}^*$ for which

$$M + (L + N)/3 = \text{even}. \quad (25)$$

In the range of the measurement in FIG. 8, this means peaking at the points $(6, 0, 0)$ and $(9, \pm 1, 0)$. Extrapolating into the 2nd BZs along κ_c , it means at the points $(7, 0, -1)$ and $(5, 0, 1)$. The angular factor,

$$Y_{xy}(\hat{\kappa}) \propto \frac{\kappa_x \kappa_y}{\kappa_x^2 + \kappa_y^2 + \kappa_z^2} = \frac{[(\kappa_a + \kappa_c)/3]^2 - \kappa_b^2}{(\kappa_a^2 + 2\kappa_c^2)/3 + 2\kappa_b^2}, \quad (26)$$

finally suppresses the intensity around $(7, 0, -1)$ and enhances it around $(5, 0, 1)$ compared with the intensity around $(6, 0, 0)$. In the range relevant for FIG. 8, which is centered at the structure-factor peak at $(6, 0, 0)$, the angular factor squared increases nearly linearly with κ_c in the range $(-1|1)$ by a factor 4, while the variation with κ_b in the range $(-\frac{1}{4}|\frac{1}{4})$ is comparatively small. Hence,

whereas $|\chi_{xy}(6, \kappa_b, \kappa_c)|^2$ according to Eq. (22) gets reduced by a mere 30% for $|\kappa_b|$ increasing from 0 to $\frac{1}{4} \approx k_F$, it has a strong κ_c -dependence with a peak at $\kappa_c \sim \frac{1}{2}$, decreasing by a mere 10% when going to $\kappa_c=1$, but by a factor 4 when going to $\kappa_c=-1$. Although this strong behavior is smeared out in reality, the trend is consistent with the intensity variation seen in FIG. 8 as a function of κ_c when proceeding from (a) to (b) to (c), *provided that* the κ_c -values in (b) and (c) are negative. It is in particular consistent with the drop-off of intensity in the 2nd BZ ($-1 \leq \kappa_c \leq -\frac{1}{2}$) seen in FIG. 9 (b) and in FIG. 10 for the xy band as measured.

The structure factors for the equivalent xz and yz WOs are given by (23) with respectively y and x replaced by z . The result of using transformation (24) is then that both $\mathcal{S}_{xz}(\kappa)$ and $\mathcal{S}_{yz}(\kappa)$ peak with value 1 at the points for which $M + (L + N)/3$ and $N + (L + N)/3$ are both even. In the neighborhood of the range relevant for FIG.s 9 and 10 are the points $(6, 0, 0)$, $(6, \pm 1, \pm 3)$ and $(6, \pm 2, 0)$. The angular factor, $Y_{xz}(\hat{\kappa})$ or $Y_{yz}(\hat{\kappa})$, now suppresses all these peaks, except $(6, 0, 0)$, $(6, -1, -3)$, and $(6, -2, 0)$ for xz , and $(6, 0, 0)$, $(6, 1, -3)$, and $(6, 2, 0)$ for yz , whereby the maximum at $(6, 0, 0)$ gets shifted to $(6, -0.2, -0.2)$ for xz and to $(6, 0.2, -0.2)$ for yz . As we shall see, this is roughly consistent with the intensity variations as measured for the xz and yz bands in FIG.s 9 and 10.

C. Constant-energy surfaces in the $(6, k_b, k_c)$ plane

Apart from the observed intensity variations, we confirm that slightly below the Fermi level there is no dispersion along κ_a , i.e. there is strongly reduced dimensionality in the a^* -direction, which we shall therefore neglect from now on. In the c^* -direction, i.e. from plane to plane of the three FS maps, the dispersion is very weak, although we shall later demonstrate in detail that this perpendicular dispersion is not zero and that the two bands are slightly split, very much as predicted by the LDA. Taking together the behavior along a^* and c^* , this implies a quasi-1D metal.

We now come to ARPES measurements in the b^*c^* -plane and for energies, ω , extending from slightly below the Fermi level to a bit above the bottom of the Mo $4d$ bands. The photon energy is $h\nu=30$ eV and controls the value of $\kappa^2 = (\kappa_a^2 + 2\kappa_c^2)/3 + 2\kappa_b^2$, such that the CECs for $\kappa_a=6$ are obtained in the range $-\frac{1}{2} \leq \kappa_b \leq \frac{1}{2}$ and $-1 \leq \kappa_c \leq 0$. With reference to FIG. 9 (a), that is the upper half of the BZ centered at $\Gamma_{600} \equiv \Gamma$, plus the lower half of the one centered at $\Gamma_{60-1} \equiv \Gamma'$. We shall refer to these small BZs as respectively the 1st and the 2nd BZ. Together, they form the upper part of the double zone centered at Γ . Here, "upper" and "lower" refer to the orientation chosen in the figure, which has $-\kappa_c$ pointing upwards. Since the band structure –but not the ARPES intensity– has inversion symmetry, we shall for simplicity, but inconsistent with Eq.s (19)-(21), flip the signs of k_b

and k_c such that $k_b \equiv -\kappa_b$ points to the right and $k_c \equiv -\kappa_c$ upwards. The dispersion with $k_a \equiv \kappa_a - 6$ will be neglected.

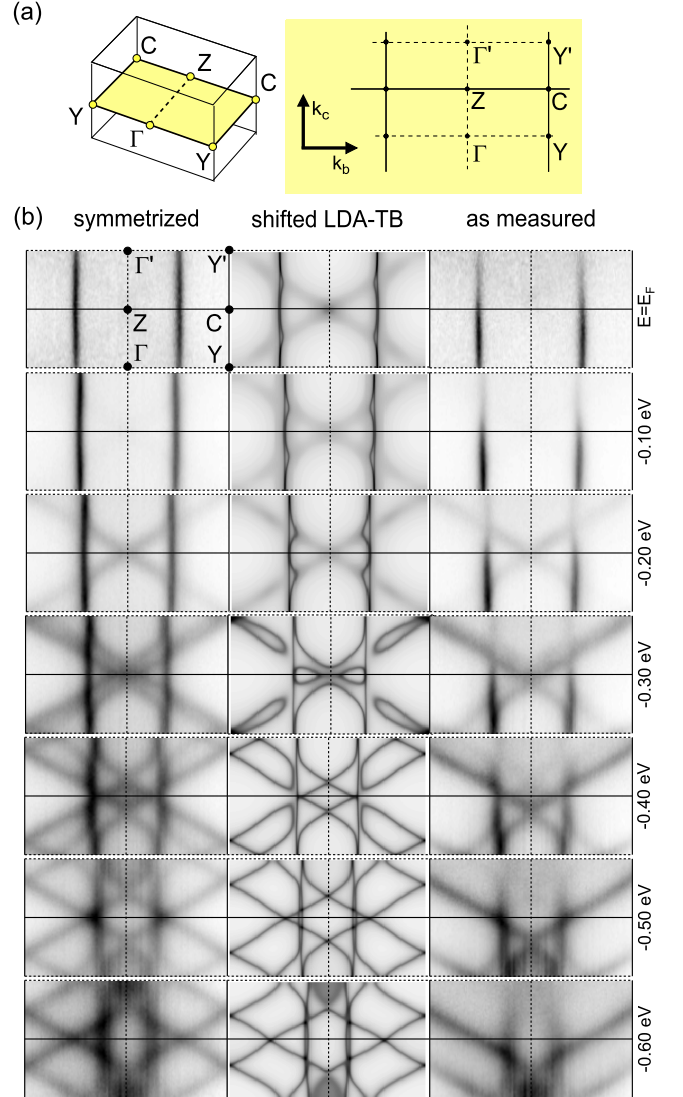


FIG. 9. (a) Orientation in the BZ of the $k_b k_c$ -plane. The constant energy contours (CECs) are shown in the upper part of the 1st and the lower part of the 2nd BZ: $-0.5 \leq k_b \leq 0.5$, $0 \leq k_c < 1$. (b) Comparison of the CECs computed from the shifted LDA-TB parameters with those measured by ARPES for sample H ($T = 6$ K, $h\nu = 30$ eV). The match with the ARPES CECs symmetrized with respect to the line ZC ($k_c=1/2$) is nearly perfect. Indicated on the right are the energies with respect to the Fermi level, which is 100 meV above the centre of the gap.

The right-hand panel in FIG. 9 (b) shows ARPES as measured and the left-hand panel shows ARPES with the intensity variations symmetrized away by averaging the data mirrored in the CZC ($k_c=\frac{1}{2}$)-line. The middle panel shows the results of the LDA with the valence bands shifted downwards by 0.1 eV in order to improve the agreement with ARPES as shown in FIG. 7 (b). In or-

der to mimic a spectral-function broadening of the dispersion, we used a Lorentzian with energy-independent width to broaden the LDA bands.

In ARPES as measured, slightly below E_F we recognize the quasi-1D FS as the straight lines $(k_b, k_c) \sim (\pm \frac{1}{4}, k_c)$. When the energy decreases to the bottom of the xy band at $B \sim -0.7$ eV, which is 0.1 eV above the lowest energy in FIG. 9, the distance between the straight-line CECs,

$$k_b(E) \sim \pi^{-1} \arccos[1 + (E - B)/2\tau], \quad (27)$$

(see Eq. (10)) decreases to zero. The intensity drop-off in the 2nd BZ ($\frac{1}{2} \leq k_c \leq 1$) is consistent with the effect of the angular factor $Y_{xy}(\hat{\mathbf{k}})$ discussed in the preceding Sect. VB. Also the quasi-1D xz and yz bands, whose dispersions are given approximately by Eq.s (13) and (12), have their bottom at -0.7 eV. At this energy, their CECs are doubly degenerate and run, respectively, along the lines ΓC ($k_c - k_b = 0$) and $-\Gamma C$ ($k_c + k_b = 0$), which cross at $\Gamma(0,0)$. See also FIG.s 5 and 4. When the energy increases from the bottom and into the respective band, each of these CECs stays straight and keeps its direction, but splits in two such that the xz and yz CECs now cross at $(0, k_c(E))$, i.e. along the ΓZ -line on either side of Γ . Here, $k_c(E)$ is given by Eq. (27) with τ replaced by A_1 . Due to the parabolic band shape this splitting is substantial already at the lowest energy displayed in FIG. 9 (b). Actually, this splitting is $\sqrt{\tau/A_1} \sim \sqrt{3}$ times the one between the xy CECs for the same energy. The intensity variations displayed by ARPES as measured are roughly consistent with what was said at the end of Sect. VB.

As can be imagined from the LDA in FIG. 9 (b), or from the symmetrized ARPES by use of Eq. (14), the CECs from the $xz(\mathbf{k} + \mathbf{c}^*)$ and $yz(\mathbf{k} + \mathbf{c}^*)$ bands start off at -0.7 eV as doubly-degenerate straight lines which cross at $\Gamma'(0,1)$ and run respectively along $-\Gamma' C$ ($k_c - k_b = 1$) and $\Gamma' C$ ($k_c + k_b = 1$). Remember from Sect. IVD that $|\mathbf{k} - \mathbf{c}^*\rangle = |\mathbf{k} + \mathbf{c}^*\rangle$, because $|\mathbf{k} + \mathbf{c}^* + M\mathbf{b}^* + N\mathbf{c}^*\rangle = |\mathbf{k} + \mathbf{c}^*\rangle$ for $M+N$ even. When the energy increases, each of these CECs splits in two, stays straight, and keeps its direction. The $xz(\mathbf{k} + \mathbf{c}^*)$ and $yz(\mathbf{k} + \mathbf{c}^*)$ CECs cross at $(0, 1 + k_c(E))$, i.e. along the $\Gamma' Z$ -line on either side of Γ' . Finally the parallel straight-line CECs from the $xz(\mathbf{k} + \mathbf{c}^*)$ and the $xz(\mathbf{k})$ bands meet at the line $-Y'Z$ ($k_c - k_b = \frac{1}{2}$), and so do those from the $yz(\mathbf{k} + \mathbf{c}^*)$ and the $yz(\mathbf{k})$ bands, but at the line $Y'Z$ ($k_c + k_b = \frac{1}{2}$). The energy at which this happens is not the common center [69], $E_0 = B + 2|A_1| \sim -0.1$ eV, of the xz and yz bands for which $k_c(E_0) = \frac{1}{2}$, but at the lower energy $E_0 - 2|G_1| \sim -0.3$ eV, because $|\mathbf{k}\rangle$ and $|\mathbf{k} + \mathbf{c}^*\rangle$ mix to make the two bands gap by $\pm 2|G_1|$. The latter energy is the top of the valence bands forming two ridges running along the two $Y'ZY$ lines and crossing at Z . Associated with the mixing –reaching 50% at the top of the valence bands– is a weakening of the $|\mathbf{k}\rangle$ character which can be seen as a weakening of the measured ARPES intensity already above -0.4 eV, before

the bands empty at -0.3 eV.

That the intensity of the $yz(\mathbf{k})$ band is slightly stronger than the equivalent $xz(\mathbf{k})$ band is presumably due to the small b -component (1) of the electric field.

Only the $xz(\mathbf{k})$ and $yz(\mathbf{k})$ bands are occupied inside their respective physical zone, $|k_c - k_b| < \frac{1}{2}$ and $|k_c - k_b| < \frac{1}{2}$, as defined in Sect. IVD, and only the $xz(\mathbf{k} + \mathbf{c}^*)$ and $yz(\mathbf{k} + \mathbf{c}^*)$ bands are occupied outside. But in ARPES as measured, we *do not see* the latter bands and, as will be demonstrated in the next section, the same holds for ARPES as measured in FIG.s 10 (d) and (e). The reason why *ARPES measures only the $|\mathbf{k}\rangle$ character* and not the $|\mathbf{k} + \mathbf{c}^*\rangle$ character is the sublattice effect explained in Sect.s IVD and VB.

For all energies in FIG. 9, both xy bands are occupied and, from Eq. (11), we would expect that a CEC for the $xy(\mathbf{k})$ band oscillates by $\delta k_b/k_b \sim (2t_1/\tau) \cos \pi k_c$, outwards in the 1st and inwards in the 2nd BZ, and that a CEC for the $xy(\mathbf{k} + \mathbf{c}^*)$ band has the opposite oscillation. This fine splitting is *not* detected in ARPES as measured. That could be a problem of resolution, but is rather the above-mentioned sublattice effect as we shall see and exploit in Sect. VI.

The xy , xz , and yz bands hybridize, and we are particularly interested in the hybridization of the xy band near E_F with the xz and yz valence and conduction (V&C) bands [45]. Although bands –and not CECs– hybridize, we can easily see the effect of this hybridization in the LDA part of FIG. 9 as four “fingers” pointing towards Z , and we can follow them as the energy is lowered into the valence bands. The origin of the fingers is clearly the energy repulsion between the hybridizing valence-band edge and *one* of the two degenerate xy bands; the other band is unaffected (because this is the way a perturbation turns the eigenvectors of two degenerate states). Since the finger is sharp, it can only come from a nearby band peak, i.e. the edge of an xz or yz band (not from a far-away yz or xz band), with a weak matrix element, and as long as the finger points towards Z rather than Y , it comes mainly from the edge of the valence- rather than from the edge of the conduction band. The corresponding peak in the xy band we shall call the *resonance peak*. Taking the nearly dispersionless k_a -dimension into account, the peak is actually a sharp fold or mountain ridge extending along \mathbf{a}^* .

D. Energy bands, $E_j(k_b, k_c)$

FIG. 10 (b) displays the “as measured” ARPES band structure on the faces of a cube with the basal plane $(6, k_b, k_c)$ extending like in FIG. 9 over the $0 \leq k_c \leq 1$ half the double zone, i.e. over the $0 \leq k_c \leq \frac{1}{2}$ half of the 1st and the $\frac{1}{2} < k_c \leq 1$ half of the 2nd BZ. On the top face, i.e. for $E \sim E_F$, we recognize from FIG. 9 the 1D xy FS, $(k_b, k_c) \sim (\pm \frac{1}{4}, k_c)$, whose intensity drops with k_c increasing from 0 to 1, presumably due to the angular factor (26). Not only the xy bands are quasi 1D, but

also the xz and the yz bands: Had the cube been cut at the top of the valence band, i.e. a bit above -0.3 eV, we would have recognized its ridges as the straight-line CECs YZY' and $Y'ZY$ crossing at all Z and Y points.

The band structures displayed in (c)-(e) are obtained by cutting the data along the lines colored in (a). In order to avoid the intensity variations, we first show –like in the left-hand panel of FIG. 9– the band structure symmetrized (averaged) over the 1st and 2nd BZs, i.e. folded into the 1st BZ [75]. Below, we show the bands as measured in the 1st BZ –the lower one in (a)– and at the bottom, those measured in the 2nd BZ –the upper one in (a). The common boundary is ZQ_1C . For comparison with the LDA bands in FIG. 7, the benefit of symmetrization is evident, but the intensity variations hold the key which will allow us to resolve the splitting and warping of the quasi-1D xy FS.

But first, let us relate the bands as measured and shown in FIG. 10 (b), (d), and (e) to the CECs as measured in the right-hand panel of FIG. 9. There, we observed –as expected– that the xz and yz bands are essentially the $|\mathbf{k}\rangle$ -projection of the bands extending over the double zone. We shall therefore use that zone in a guided tour and, hence, mentally glue the bands separated into 2nd and 1st BZs together across the common ZQ_1C boundary:

Along $\Gamma Z\Gamma'$ we see the flat bottom of the $xy(\mathbf{k})$ band at -0.7 eV and the rise of the degenerate $xz(\mathbf{k})$ and $yz(\mathbf{k})$ bands from -0.7 eV at Γ to the highest point, -0.3 eV, of the valence-band ridge at Z , whereafter the $|\mathbf{k} + \mathbf{c}^*\rangle$ characters take over [75]. This results in a drop of ARPES intensities as the energies go back down to -0.7 eV at Γ' , the point at which the bottoms of the $xz(\mathbf{k} + \mathbf{c}^*)$ and $yz(\mathbf{k} + \mathbf{c}^*)$ bands cross. Also the intensity of the $xy(\mathbf{k})$ band has dropped, but this is presumably due to the angular factor (26).

Going next from Γ to Y in the negative k_b direction, we see the $xy(\mathbf{k})$ band disperse parabolically to the Fermi level. Moreover, we see the nearly degenerate positive and negative branches of respectively the $xz(\mathbf{k})$ and $yz(\mathbf{k})$ bands rise to -0.3 eV at Y where the valence-band ridge formed by the hybridizing $xz(\mathbf{k})$ and $xz(\mathbf{k} + \mathbf{c}^*)$ bands crosses the ridge formed by the hybridizing $yz(\mathbf{k})$ and $yz(\mathbf{k} + \mathbf{c}^*)$ bands. Before reaching this far, the intensities of the xz and yz bands decrease due to the dilution of their $|\mathbf{k}\rangle$ character by $|\mathbf{k} + \mathbf{c}^*\rangle$ character. The ΓY cut in the band structure is also showed in (b), on a front face of the cube.

Proceeding now along the straight line YZY' , where the gapped $xz(\mathbf{k})$ and $xz(\mathbf{k} + \mathbf{c}^*)$ bands form a ridge. This ridge can barely be seen between Y and Z , but better between Z and Y' . The reason for this difference is connected with the fact –shown by the green line in (a)– that the data from Z to Y' were actually taken along the ridge formed by the yz bands, and from the other fact –noted in our discussion of FIG. 9 and blamed on a small b -component of the electric field– that the $yz(\mathbf{k})$ band appears with increased intensity compared with the

$xz(\mathbf{k})$ band. Returning now to the valence-band ridge at Y and going towards Z , we see the $yz(\mathbf{k})$ band fall, reach its bottom halfway towards Z , and then rise again to the highest point on the ridge at Z . At this point, the yz band not only attains $|\mathbf{k} + \mathbf{c}^*\rangle$ character, but also hybridizes with the xz band. We also see the parabolic rise of the $xy(\mathbf{k})$ band towards Y , from its bottom at Z to E_F at $\sim (\pm\frac{1}{4}, \frac{1}{4})$. Towards Y' , the xy intensity is reduced due to the angular factor.

Going along the zone boundary from Z to C , seen also on a front face of the cube in (b), the $xy(\mathbf{k})$ band rises to the Fermi level and the $xz(\mathbf{k})$ band falls from the highest point on the ridge to the bottom at C . Almost degenerate with –and indistinguishable from– the $xz(\mathbf{k})$ band is the $yz(\mathbf{k} + \mathbf{c}^*)$ band, but its intensity is presumably much lower.

Now, going into the 2nd BZ from C to Y' , we see the $xz(\mathbf{k})$ band increase to the ridge, and –degenerate herewith, but with little intensity– the $yz(\mathbf{k} + \mathbf{c}^*)$ band. Going instead into the 1st BZ from C to Y , we see the other branches of the degenerate $xz(\mathbf{k})$ and $yz(\mathbf{k} + \mathbf{c}^*)$ bands doing the same thing.

Along ΛW ($k_c = \frac{1}{4}$) we see the $xy(\mathbf{k})$ band rise parabolically from its bottom to the Fermi level, which is reached half the way to W , and the same is seen with reduced intensity along $\Lambda'W'$ ($k_c = \frac{3}{4}$). The bottom of the $xz(\mathbf{k})$ band is seen midway between Λ and W , i.e. at $(\frac{1}{4}, \frac{1}{4})$, and the $yz(\mathbf{k})$ band –which is degenerate with the $xz(\mathbf{k})$ band at Λ – increases until at $(\frac{1}{4}, \frac{3}{4})$ it reaches the top of the ZY ridge where it mixes with the $yz(\mathbf{k} + \mathbf{c}^*)$ band coming from W and thereby loses its intensity. Going now from Λ' towards W' , it is the $xz(\mathbf{k} + \mathbf{c}^*)$ band which –with weak intensity– increases until at $(\frac{1}{4}, \frac{3}{4})$ it reaches the top of the ZY' ridge where the $|\mathbf{k}\rangle$ character takes over and the $xz(\mathbf{k})$ band continues with full intensity downhill.

The $P_1Q_1P'_1$ -line is perpendicular to the ΛW and $\Lambda'W'$ lines and is parallel to, but slightly inside the FS so that the trace of the xy band is ~ 170 meV below the Fermi level and thereby clearly visible in ARPES –albeit with the usual angular-factor reduction of the xy intensity towards P'_1 . Starting from P_1 , we see the bottom of the $xz(\mathbf{k})$ band and –above it, with slightly less intensity– the $yz(\mathbf{k})$ band rising to the ZY ridge where it attains $|\mathbf{k} + \mathbf{c}^*\rangle$ character and vanishes on the downhill side towards Q_1 . In the 2nd BZ towards P'_1 , we see the continuation of the $xz(\mathbf{k})$ band which now rises to the ZY' ridge where it attains $|\mathbf{k} + \mathbf{c}^*\rangle$ character and finally vanishes on the downhill side towards P'_1 .

The resonance peaks in the xy bands, predicted by the LDA in FIG.s 7 (a) and (b), and seen in the CECs in FIG. 9 (b) at approximately $(\frac{1}{4}, \frac{3}{4})$ and $(\frac{1}{4}, \frac{1}{4})$, are due to the repulsion caused by hybridization with the top of respectively the xz valence band –most clearly seen in FIG. 10 (e) when leaving the xz zone, $|k_c - k_b| \leq \frac{1}{2}$, going from Q_1 to P'_1 – and with the top of the yz valence band –most clearly seen in (d) when leaving the yz zone, $|k_c + k_b| \leq \frac{1}{2}$ going from P_1 to Q_1 . The two other peaks

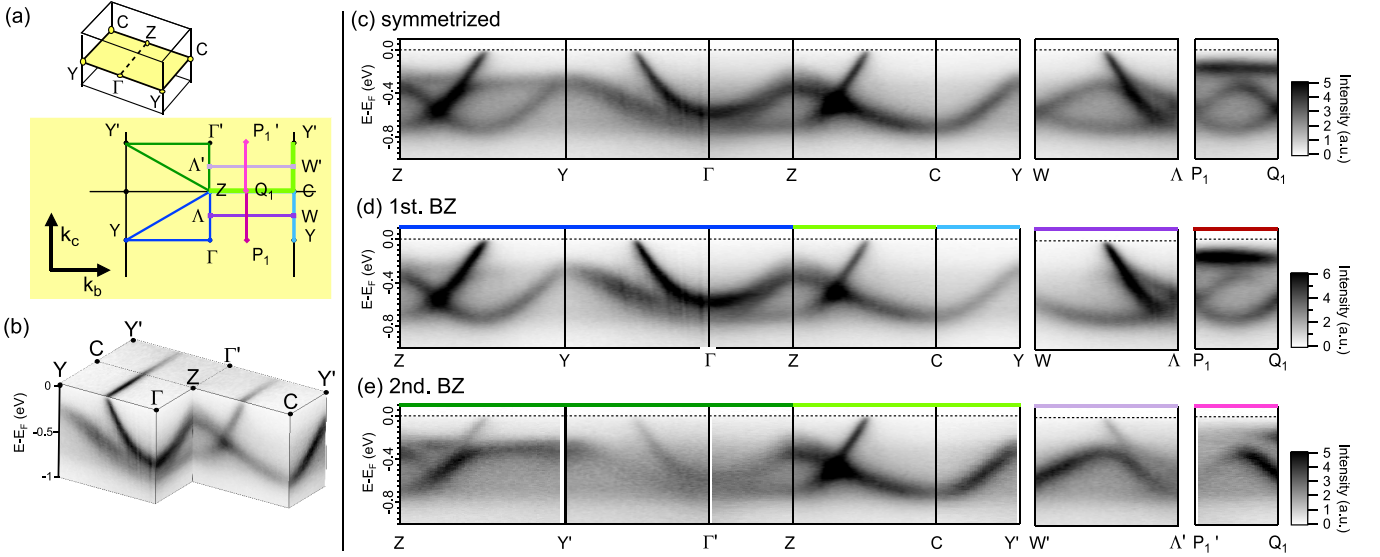


FIG. 10. ARPES band structure. (a) Orientation of half the 1st BZ in $k_a k_b k_c$ -space and, in the $k_b k_c$ -plane, half the 1st BZ centered at Γ (0,0) and half the 2nd BZ centered at Γ' (0,1). (b) Data as measured from sample H ($T = 6$ K, $h\nu = 30$ eV) presented in an $E(k_b, k_c)$ -cube from which cuts along the \mathbf{k} -paths colored in (a) produce the band structures shown in (c)-(e). (d) Some features can be better seen in the 1st BZ, (e) while others are more pronounced in the 2nd BZ, and vice versa. (c) The symmetrized band structure shows all spectral features.

at approximately $(-\frac{1}{4}, \frac{3}{4})$ and $(-\frac{1}{4}, \frac{1}{4})$ are caused by hybridization with the top of the yz and xz valence bands, respectively.

Still, we have seen none of this fine resonance structure in the experiments, but before attempting to let the LDA guide the analysis of the ARPES data beyond the 100 meV scale, we need to assess the degree of agreement between the LDA and ARPES.

E. Agreement between the LDA and ARPES

The band structure derived from the symmetrized ARPES data points is shown in FIG. 7 (a), (a2), and (b). Those indicated by black dots were extracted by finding the maximum intensity in cuts along appropriate momentum directions, traditionally called a momentum distribution curve (MDC). The other procedure used is to find the maximum intensities in the energy distribution curves (EDCs), the results indicated by grey circles. Technically, the maxima in these curves were found from the zeros in the smoothed first partial (along one momentum direction) derivatives of the BZ-symmetrized ARPES data and the conditions that the smoothed second partial derivative is smaller than zero.

The bands resulting from the first-principles LDA calculation in the truncated TB representation of the six t_{2g} low-energy WOs (Sect.s IV and A) are shown in (a), with the sum of the xz and yz characters in green and the xy character in red. Note the strong hybridization of the nearly degenerate bottoms of the two xy and the xz and yz valence bands near Γ . Note also the hybridiza-

tions between Z and Y and between W and Λ . Near the middle of the latter line where the two degenerate xy bands in the gap come close to the valence and conduction bands, and their repulsion is therefore strong—but in opposite directions—one of the xy states stays unaffected and the other is pushed up or down in energy depending on whether the repulsion from the valence or the conduction band is stronger. Since this balance tips as we move up through the gap, the hybridization shifts from the upper to the lower xy band and causes the resonance peak to shift from upwards pointing in the upper band, to downwards pointing in the lower band. The fact that the matrix element, $\alpha(\mathbf{k}) + a(\mathbf{k})$, for hybridization (A19) of the xy and xz/yz bands decreases with increasing k_b (see FIG. 16, left-hand sides in the 6th row) causes the rather unusually-looking dispersion of the two xy bands in the gap. This asymmetry will be explained in App. B1, specifically in connection with Eq. (B4). Along P_1Q_1 , we clearly see the resonance peak in the upper xy band.

Overall, there is good agreement between the occupied LDA and ARPES bands, the main discrepancy being that the valence bands lie 100 meV too high with respect to the xy bands and thereby with respect to the Fermi level. This may be partly a surface effect: the xz and yz WOs reach farther into the vacuum and therefore feel a higher LDA potential than the xy WOs which are well inside the staircase. In addition, there is undoubtedly an LDA error; for instance are LDA bandgaps in semiconductors too small, and FS measurements for bulk 4d metals indicate that the accuracy with which the LDA describes the energy separation between inequivalent t_{2g} levels is ~ 50 meV [76]. For LiPB we therefore

correct the bulk LDA bands in the TB representation by shifting the common energy of the xz , XZ , yz , and YZ WOs downwards by 100 meV [more precisely, we shift the on-site energy, τ_0 , of the xy and XY WOs 100 meV upwards, from 47 to 147 meV in Table (A8)] and recalculate the Fermi level. As we have seen already in FIG. 9, the resulting band structure shown in FIG. 7 (b) agrees very well with ARPES, except near Z where the splitting of the valence-band is too small and the lowest conduction band almost touches the Fermi level, thus asking for a fine-adjustment of the TB parameters. That the shifted LDA bands lie above the ARPES bands along P_1Q_1 is an artefact caused by the uncertainty about the filling of the metallic band. The filling was exactly 50% in the calculation for the stoichiometric crystal, but Li and O vacancies makes the filling uncertain in the experiment, where it is estimated from the measured k_{Fb} value (App. C) to be 51 ± 1 %, i.e. to have the effective stoichiometry $Li_{1.02 \pm 0.02}$. Using the measured Fermi-velocity, this gives a Fermi level which, with respect to the band structure, is between 50 and 0 meV above the one for the stoichiometric crystal assumed in the calculation. In order to ensure that the states measured with ARPES are fully occupied, the P_1Q_1 line in the experiment was chosen to have $k_b=0.225$, which corresponds to k_{Fb} for $Li_{0.90}$. We took the same value of k_b in the calculation.

Considering the good agreement between the widths of the occupied part of the metallic xy bands in the ARPES and in the LDA (where this width is independent of the our energy shift), we realize that the magnitude of the on-site Coulomb interaction U cannot be large, because the LDA bandwidth should be renormalized by the strength of U , as was actually done in Ref. 39 using the dynamical mean-field approximation (DMFT), and where the same conclusion was drawn.

VI. THE QUASI-1D BANDS IN THE GAP

A. Seeing the resonance peak in ARPES

FIG. 7 (a2) shows a blow up along P_1Q_1 of the two bands in the gap, 0.16 eV below E_F . The ARPES bands were traced from the symmetrized data shown in FIG. 10 (c). Whereas the three purple diamonds labeled 'MDC2' are from MDCs along respectively ΓY , WL , and ZC , perpendicular to P_1Q_1 , the black dots are from EDCs. The grey region indicates the uncertainty of the experiment, as well as the uncertainty in determining the dispersion of all the bands. No resonance peak is seen here!

However, in the preceding Sect.s IV and V we have learned that ARPES measures the occupied t_{2g} bands nearly as if the two ribbons were *translationally* equivalent. This means that ARPES sees the occupied part of the three $|\mathbf{k}\rangle$ bands in the double zone and little more. Said in another way, ARPES sees the two gapped $xz(\mathbf{k})$ and $yz(\mathbf{k})$ bands inside the common part of their physical zones and the metallic $xy(\mathbf{k})$ band throughout the

double zone. The decrease of the ARPES intensity of the $xy(\mathbf{k})$ band in the 2nd BZ, we ascribe to merely the angular factor in Eq (26) and it should therefore be possible to "look through" this and see the resonance peak in the $xy(\mathbf{k})$ band, not only along P_1Q_1 at $(k_b, \frac{1}{2} - k_b) = (0.225, 0.275)$ where it is caused by the hybridization with the edge of the yz valence band, but also along $Q_1P'_1$ at $(k_b, \frac{1}{2} + k_b) = (0.225, 0.725)$ where it is caused by the edge of the xz valence band.

This has been attempted in FIG. 7(b2) which shows the ARPES dispersions extracted *separately* from the two different BZ's, with the uncertainties indicated in a similar way as in (a2). It is seen to work beautifully! According to what was said above, we interpret (b2) –with details to be given later– as the $xy(\mathbf{k})$ -like band in the double zone, but with the part in the 2nd BZ translated into the 1st irreducible BZ as $xy(\mathbf{k} + \mathbf{c}^*)$, and colored blue. The large resonance peak seen in the blue band at $(0.225, 0.275)$ thus originates from the resonance with the edge of the yz valence band at $(0.225, -0.725)$. Actually, what the folding procedure [75] brings into the irreducible part of the 1st BZ from the 2nd BZ, is the resonance peak from the xz valence band at $(0.225, 0.725)$. Since the peak points upwards, the hybridization with the valence band prevails. In the green band, we see no trace of the resonance with the edge of the yz valence band at $(0.225, 0.275)$, but in the red TB band, it is the cause of the faint maximum of the lower band, slightly closer to Q_1 than the peak in the upper band.

ARPES should show the $xy(\mathbf{k})$ - and $xy(\mathbf{k} + \mathbf{c}^*)$ -like bands with a hybridization between them which vanishes at P_1 ($k_c=0$) and has its maximum at the BZ boundary, Q_1 ($k_c=0.5$). The apparent crossing of the two ARPES bands near P_1 , as well as their apparent lack of splitting at Q_1 , is not inconsistent with this and the shifted LDA bands have none of these peculiarities. Otherwise, the agreement between ARPES and the LDA bands is astonishingly good. In both cases, the peak caused by the resonance with the yz bands at $(0.225, -0.725)$ comes out clearly in the upper band, and so does the lack of a visible resonance peak in the lower band at $(0.225, 0.275)$. So it seems worth while to refine the TB fit to the ARPES bands, and subsequently use this TB model to describe and seek the origins of the observed k_c -dispersion on the 10 meV-scale and to study the k_c -dispersion as a function of the position of the xy bands in the gap, i.e. of their k_b -value.

B. Refining the six-band TB Hamiltonian to agree with ARPES

Our first-principles LDA TB description of the six lowest energy bands is given in App. A1 and has about 40 TB parameters (WO energies and hopping integrals). Their original values given in Tables (A8)-(A12) yield the band structure shown in FIG. 7(a) and the improved agreement with ARPES seen in (b) is achieved by merely

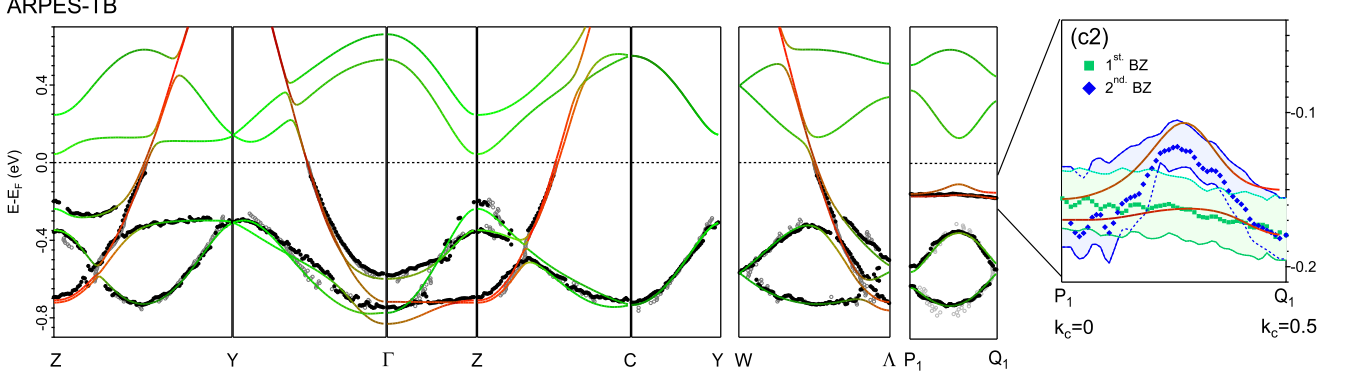


FIG. 11. Band structure obtained as the eigenvalues of the six-band TB Hamiltonian, Eq. (A18) - (A20), with parameter values refined to improve the fit to the ARPES bands and given in the square parentheses in Tables (A8)-(A12). The Fermi level is 75 meV above the center of the gap, see text following Eq. (A14). The ARPES data are those already shown in FIG. 7 (b) and (b2). The P_1Q_1 line had $k_b=0.225$ in ARPES as well as in the calculation.

shifting the value of τ_0 , the energy of the degenerate xy and XY WOs, up with respect to that of the degenerate xz , XZ , yz , and YZ WOs. The latter is the energy at the center of the gap and is taken as the zero of energy in the TB Hamiltonian. Still, the Fermi velocity is too small and the levels near Z , where the V&C bands come closest, remain inaccurate: the splitting of the valence band levels is too small while that of the conduction band levels is too large. This is due to bad convergence and truncation of the xz - yz hybridizations (A5), to our neglect of the spin-orbit coupling mentioned at the end of Sect. II B, and to the LDA yielding too small a gap.

We therefore refine the parameter values, with the result given in square parentheses in Tables (A8)-(A12). Specifically, we found it necessary to modify the values of the intra-ribbon hopping integrals, first of all between respectively the on-site, 1st-, and 2nd-nearest xy WOs, τ_0 , τ_1 , and τ_2 . This increases the Fermi velocity by about 15%, increases the upwards curvature of the bands near half filling, and lowers the half-filling Fermi level to 53 meV above the center of the gap, see App. A 1 Eq.s (A8) and (A13)-(A15). Secondly, we refined the values of the xz - yz hopping integrals, m_1 , λ_2 , and λ_3 in Eq. (A12)[28]. In addition, the value of the gap parameter, G_1 , giving the asymmetry between the forwards and backwards hoppings, $xz \leftrightarrow XZ$ ($yx \leftrightarrow YZ$), as explained after Eq. (12) and given in Eq. (A10), was increased by 10%. The resulting band-structure is displayed in FIG. 11 and is seen to agree nearly perfectly with the experiment. Most important: the blow up (c2) demonstrates that this refinement of merely 7 out of the more than 40 TB parameters to fit the ARPES bands on the 100-meV scale, also achieves nearly perfect agreement for the k_c -dispersion of the quasi-1D bands slightly below the Fermi level. This includes agreement with the size and shape of the resonance peak without having modified any of the 17 (a, g, α, γ)-parameters (A11) needed to describe hybridization between the xy and the xz and

yz bands, parameters which decisively influence the peak structure as is explained in App. B 1.

C. Dispersion and splitting of the bands in the gap

To the perpendicular features of the xy -like bands in the gap seen in FIG. 11(c2), there are contributions from both *direct* hops [28], t and u , between the xy and XY WOs, as well as from *indirect* hops of the xy and XY WOs via the xz and XZ WOs, and via the yz and YZ WOs. While the contribution from the direct hops gives rise to the two 1st and 2nd-nearest-neighbor TB bands shown in green in FIG. 12, addition of the indirect hops results in the two bands shown in black. These bands were calculated with the two-band Hamiltonian (B2) derived in App. B from the six-band Hamiltonian, presented and transformed to the mixed representation (A25) in App. A.

In FIG. 12, \mathbf{k} is limited to the irreducible part of the 1st BZ ($k_b=0.225-0.275$, $0 \leq k_c \leq 0.5$) and the fatness is proportional to the $|\mathbf{k}|$ character. As mentioned above, near $k_c=0.25$ where the xy bands come close to the V&C-band edges formed at the crossings between the $xz(\mathbf{k})$ and $xz(\mathbf{k} + \mathbf{c}^*)$ bands, and between the $yz(\mathbf{k})$ and $yz(\mathbf{k} + \mathbf{c}^*)$ bands, the indirect hops cause resonance structures and, as judged from the sharpness of these structures the indirect hops have exceedingly long range. The peak in the upper band has dominating $|\widetilde{xy}; \mathbf{k} + \mathbf{c}^*\rangle \equiv |\widetilde{xy}; k_b, k_c + 1\rangle$ character, while the weaker resonance feature in the lower band has $|\widetilde{xy}; \mathbf{k}\rangle \equiv |\widetilde{xy}; k_b, k_c\rangle$ character, in agreement with what was said in Sect. VI A. While at $k_c=0$, $|\widetilde{xy}; \mathbf{k}\rangle$ and $|\widetilde{xy}; \mathbf{k} + \mathbf{c}^*\rangle$ cannot mix, at the zone boundary, $k_c=0.5$, they are degenerate and therefore mix completely. Here and in the following, a tilde over the xy WO means that it has the xz and yz characters downfolded.

As seen from the difference between the black and

green bands, not only at resonance, but also near $k_c=0$ and 0.5, where the xz and yz valence bands are degenerate, and the xz and yz conduction bands too, and both are more than 200 meV away from the \tilde{xy} bands (see FIG 16, columns 1, 3, and 5 in the 3rd row), the indirect coupling reduces the splitting between the bands near $k_c=0$, and increases it near $k_c=0.5$ where it creates a bulge in the lower band.

The spin-orbit coupling mentioned in Sect. IIB does not affect the quasi-1D bands in the gap in the stripe $0.225 \leq |k_b| \leq 0.275$ near the FS.

It should be noted that the k_c -dispersion measured with ARPES along P_1Q_1 ($k_b=0.225$), shown together with its simulation by TB in FIG. 11(c2), differs substantially from the dispersion simulated for $k_b=0.250$, the Fermi vector for half filling, and shown in the middle panel of FIG. 12. The latter dispersion itself, differs substantially from the one for $k_b=0.275$ where the energy is just a bit below the bottom of the conduction band, which is 218 meV above the center of the gap. The three k_b -values chosen in FIG. 12 correspond in the rigid-band picture to respectively 10% underdoping ($Li_{0.9}$), half-filling (Li), and 10% overdoping ($Li_{1.1}$) of stoichiometric $LiMo_6O_{17}$ (see brown, green, and olive dot-dashed k_{Fb} lines in FIG. 5). In FIG. 12, the center of gravity of the directly-coupled, green bands is independent of k_c and is given by the 1D-dispersion, $\tau(k_b)$, caused by the direct intra-ribbon xy -hopping and given by Eq.s (A2) and (A13). This is not the case for the directly- and indirectly-coupled black bands. Upon going through the gap from the top of the valence bands at $2G_1=-218$ meV to the bottom of the conduction bands at $-2G_1=218$ meV, the black bands develop from having a strong resonance peak in the upper band and a small downwards bulge around the BZ boundary in the lower band, over having a reduced peak and an increased bulge –and thus minimal width– near midgap, and to having a large bulge in the lower band and the reminiscence of the peak in the upper band. This may also be seen in the left-hand pictures in the 3rd. row of FIG. 16. Near $k_c=0$, the splitting of the bands and the dispersion of the lower band, together with the range over which this band is flat, decrease with doping. This development is far from symmetric around the mid-gap energy, although the valence and conduction bands on either side of the direct gap have the same character, apart from being respectively xz - XZ (or yz - YZ) bonding and antibonding. Appendix B1 shows in didactic detail, that the origin lies in the complicated bi-products forming the residues, $\Gamma(\mathbf{k})$, of the matrix elements for the indirect, resonant couplings [see Eq.s (A25), (B3), (B7), (B8), and FIG. 16].

The asymmetry may also be seen in FIG. 13. On the left-hand side, we show the upper (a), the lower (b), and both (c) quasi-1D \tilde{xy} bands in the gap, which extends from -218 meV to $+218$ meV, as functions of (k_b, k_c) for $0.225 \leq k_b < 0.275$ and $0 \leq k_c \leq 1$ (see FIG.s 4 and 5). Resonance peaks pointing upwards/downwards develop in the upper/lower band near the top/bottom edges of

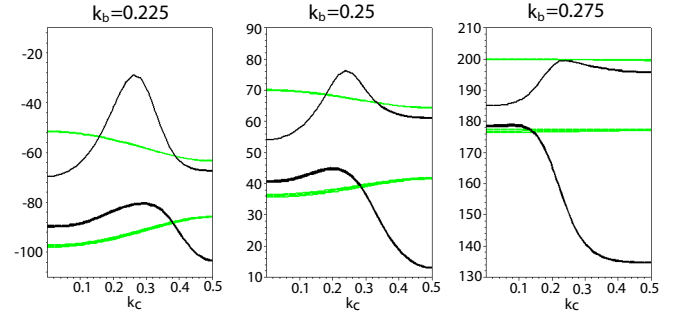


FIG. 12. Quasi-1D bands in the gap for fixed $k_b=0.225$, 0.250, and 0.275 and as functions of k_c in the irreducible BZ ($0 \leq k_c \leq 0.5$). The fatness is proportional to the $|\tilde{xy}; \mathbf{k}|$ character, with the tilde indicating that the xz , XZ , yz , and YZ characters have been downfolded. The green bands include merely the direct hops and are the eigenvalues of the 2×2 xy -block of the six-band Hamiltonian, (A1) or (A21). The black bands are the eigenvalues of the two-band Hamiltonian (B2) with the ARPES-refined parameter values. In the denominators, E equals the eigenvalue, whereby the bands are identical with those from the six-band Hamiltonian. The energy is in meV with respect to the center of the gap. The ARPES samples had $E_F=75$ meV. The top of the valence band and the bottom of the conduction band are $\pm 2G_1 = \mp 218$ meV (neglecting the zx - yz hybridization).

the xz - or yz -like valence/conduction bands. In addition, around the zone boundary ($k_c=0.5$), the lower band develops a downwards bulge which increases, widens, and merges with the resonance peaks as the conduction-band edge is approached. The splitting between the two bands is smallest at the zone center ($k_c=0+\text{integer}$) where $|\mathbf{k}|$ and $|\mathbf{k} + \mathbf{c}^*|$ characters cannot mix and the direct and indirect hoppings work in opposite directions.

D. Fermi surface and velocities

On the right-hand side of FIG. 13, (d) shows CECs, $E_j(k_b, k_c) = E$, for energies in the upper half of the gap. Those for $E = E_F$ and $E_F - 100$ meV were shown already in FIG. 9. This figure, as well as FIG.s 5 and 4, remind us that in addition to the two sheets shown in FIG. 13, there are those symmetric [77] around $k_b=0$. Moreover, that the "fingers" caused by the resonances with the V and C bands point towards respectively Z and Y. Since the quasi-1D bands disperse far more along k_b than along k_c , the shape of two CECs in (d) resembles that of the two energy bands in FIG. 12, with the $E \leftrightarrow k_b$ scaling being approximately: $dk_b = -dE/\tau'(k_b)$, and $\tau'(k_b)$ the dominating part of the Fermi velocity (A13). This resemblance is less good close to the V- or C-band edge where the hybridization with the close edge distorts the two CECs differently and, as seen in FIG. 9, eventually makes the hybridizing CEC fuse with the CEC of the edge. If we interpret a CEC as a doped FS, an energy increase of 50 meV corresponds to a 4% increase of the

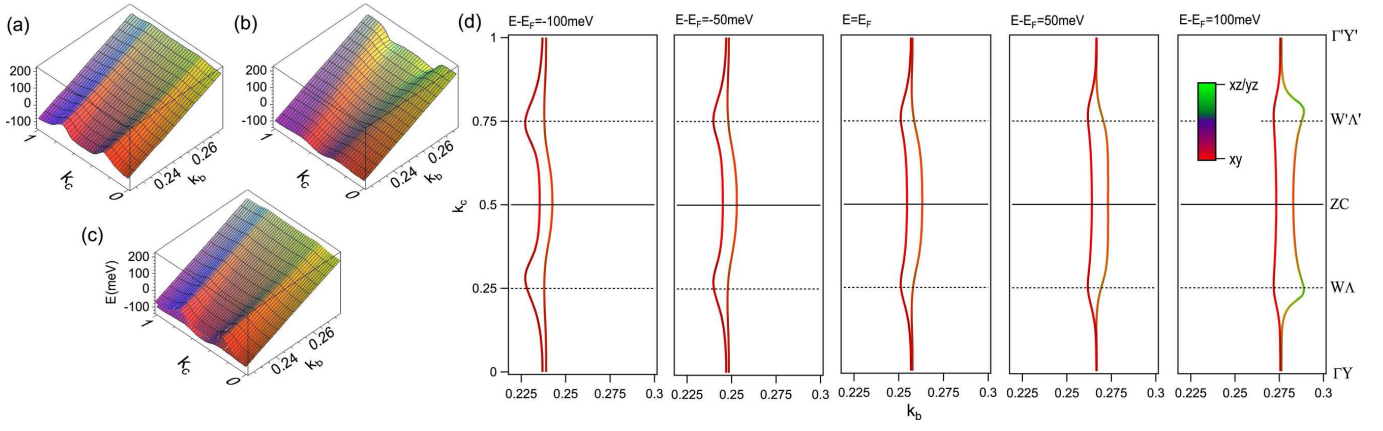


FIG. 13. The two quasi-1D bands in the gap for the six-band Hamiltonian (A1) with the ARPES-refined parameter values (A8)-(A12). The \mathbf{k} -space region considered is $0 \leq k_c \leq 1$ and $0.225 \leq k_b \leq 0.275$. The energies of the upper (a), the lower (b), and both bands (c), relative to the center of the gap. $E_F = 75$ meV. (d) CECs calculated by tracing the roots of the secular determinant $|H(k_a, k_b) - E|$. The colors indicate the orbital characters of the bands. The inner-sheet fingers point to Z and the outer-sheet fingers to Y and Y' (see FIG.s 5 and 9). Note that the ratio between the real k_c -height and the real k_b -width of a panel is $(1.0/0.08) (c/b) = 21.5$, but merely ~ 2 in this distorted figure. In reality, the ratio between k_{Fb} and the warping of each (inner or outer) FS sheet is 0.035. If the indirect coupling to the V&C bands were neglected (corresponding to the green bands for $k_b=0.25$ in FIG. 12), this ratio would be merely 0.007.

electron doping, whereby the undoped FS is the CEC with the average k_b equal to 0.25. This follows from the 1D nature of the band and the value of $\tau'(k_b)$ given by Eq.s (A13) and (A15). Finally, note the large difference between the k_b and k_c scales in (d).

The strong dependence of the non-trivial k_c -dispersion and splitting of the two quasi-1D CECs on their energy-position in the gap is explained in App. B 1.

Below, we shall analyze the ARPES data for energies closer to the Fermi level than the 160 meV studied along the $P_1Q_1P'_1$ -line, and demonstrate that the details shown for $k_b=0.25$ in FIG. 12 are indeed present in the experiment.

In order to extract the experimental Fermi-surface despite the very small splitting of the quasi-1D bands and the ARPES intensity variations, we had to perform the elaborate analysis presented in App. C.

FIG. 14 (a) compares the experimental FS from sample G with the FS calculated using the six-band TB Hamiltonian with the refined parameter values (App. A). The Luttinger volume obtained by the experiment corresponds to an effective $\text{Li}_{1.02}$ stoichiometry, i.e. the average $|k_b|$ is $0.254 \approx 1.02/4$. This places the Fermi level 75 meV above the center of the gap in the calculation. The procedure (Sect. VIB) for refining the values of the TB parameters to fit the ARPES dispersions for energies more than 0.2 eV below E_F in one sample does well in describing the dispersions for energies closer to E_F than 0.2 eV in both samples.

In (b) we show the k_c -dependency of the Fermi velocities projected onto the k_b -direction,

$$\mathbf{v}_{Fj}(k_c) \cdot \mathbf{b}^*/b^* \equiv \partial E_j(k_b, k_c) / (\partial k_b b^*)|_{E_F}, \quad (28)$$

as obtained from the TB Hamiltonian with the refined

parameters (light-blue) and from ARPES (squares, red for $-k_b$ and green for $+k_b$). Referring to the two bands shown in FIG. 12, the TB velocity projections (28) were calculated as differences between the bands for $k_b=0.2505$ and 0.2495 . For k_c values where a FS sheet is normal to the k_b direction the velocity projection (28) has extrema. At the zone center ($k_c=0, 1$) and at the zone boundary ($k_c=0.5$) these extrema are maxima [note that in (b), the velocity increases toward the left]. For the inner-sheet (upper-band) fingertip ($k_c \sim 0.25$ and 0.75) the extrema are minima. Also the outer sheet (lower band) is seen to have minima, but they are slightly closer to the zone boundary than for the fingertips of the inner sheet. Their origin is the weak resonance peak in the lower band seen in FIG. 12 and explained in Eq. (B9), combined with the increase of $|\mathbf{k}| - |\mathbf{k} + \mathbf{c}^*|$ hybridization and concomitant bulge formation as the zone boundary is approached. The magnitudes of the light-blue velocity variations are largest for the outer sheet (contrary to the energy variations, which are strongest for the upper band), decreasing from $4.8 \text{ eV}\text{\AA}$ at $k_c=0$, to a minimum of $3.8 \text{ eV}\text{\AA}$ near $k_c=0.30$, and rising again to a relative maximum of $4.4 \text{ eV}\text{\AA}$ at $k_c=0.5$, the center of the bulge. For the inner sheet, the velocity changes from a relative maximum of $4.5 \text{ eV}\text{\AA}$ at $k_c=0$, to a minimum of 4.0 near the fingertip, and to the maximum of $4.6 \text{ eV}\text{\AA}$ at the zone boundary. These sheet- and k_c -dependent values may be compared with the dominating value $4.6 \text{ eV}\text{\AA}$ of $b\tau'(k_b)$ in Eq.s (A15) and (A13) from the direct hopping along the ribbon. Due to the indirect hops via the valence and conduction bands giving rise to the resonance terms in Eq. (B2) (see App. B), the band- and k_c average of the light-blue velocity projections is smaller than $b\tau'(k_b)$. Although the velocity extraction procedure (see App. C)

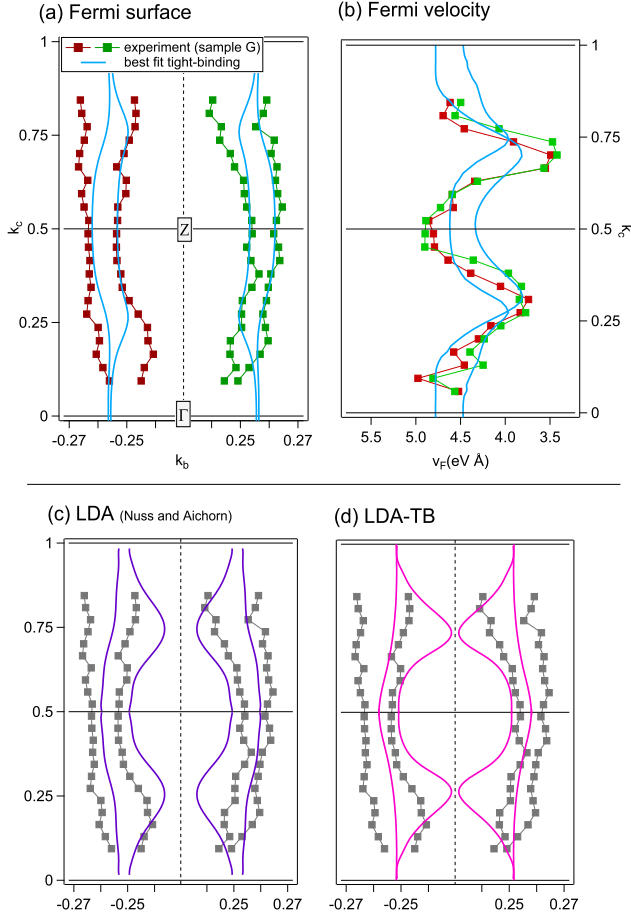


FIG. 14. **(a)** FS from the TB model with the ARPES-refined parameters compared to the experimentally obtained splitting derived by the Sparrow criterium (App. C3) and k_{Fb} from the dispersion analysis (App. C2). **(b)** Average experimental Fermi velocities (28) compared with those from the refined TB model. **(c)** FS compared to Ref. 39, and **(d)** to our LDA TB calculation. The FS calculated with the shifted LDA parameters is intermediate between the magenta FS in (d) and the light-blue FS in (a).

for the ARPES data could not distinguish the two bands, nevertheless the resulting (red and green squares) average experimental variation [78] for the two bands clearly shows both the qualitative behavior and the general magnitude implied by the refined TB velocities (as expected since the latter come from optimizing theory to experiment as specified in Sect. VIB).

It is also interesting for the many-body physics of LiPB to compare the experimental velocities to those for the TB bands based on the LDA parameters. As suggested by the LDA dominant velocity value 4.0 eV\AA from $b\tau'$ (k_b), also given in Eq. (A15), the experimental velocities (and those for the ARPES-refined TB) are generally greater than those for the LDA by about 15% [79]. There are two points to be made. First, for a 3D quasi-particle material the increase of the experimental velocity rela-

tive to the LDA value would seem surprising since the usual effect[80], arising from an energy dependent single particle self energy, caused by e.g. $e-e$ or $e-ph$ interaction, is an increase of the Fermi mass, i.e. a decrease of the Fermi velocity [81]. Indeed such was found in the single-site DMFT quasi-particle treatment of LiPB [39]. However, as we have emphasized in the Introduction, LiPB is a quasi-1D material whose ARPES k -averaged lineshapes show TL-model properties, i.e. quasi-particle suppression and spin-charge separation, specifically, collective mode holon-peak and spinon-edge features that disperse with different velocities, v_ρ and v_σ , respectively. As described in App. C, our model-independent ARPES analysis procedure, performed on a TL lineshape, would yield a dispersion intermediate between v_ρ and v_σ , but tending mostly to that of the holon peak. Within 1D theory, v_ρ and v_σ can just as well be either larger or smaller than the underlying v_F of a non-interacting system, as can be seen, for example, from formulas within the framework of the “g-ology” formulation [82, 83]. So if we identify the LDA value of $v_F = 4.0 \text{ eV\AA}$ as “non-interacting,” which ignores the difficulty of disentangling any many-body contribution already present in LDA, and think of our ARPES lineshape in a TL context, it is well within general theoretical expectations that our experimental velocity is larger than the LDA value. In this view, it may well be that our ARPES-refined TB description is modifying the entire k_b dispersion somewhat in order to reproduce the experimental low-energy scale velocity near E_F .

Second, combining our results with a previous ARPES lineshape analysis [18], we can now be somewhat more precise about the velocity renormalizations for LiPB. At high temperatures, where the LiPB ARPES lineshapes are well described by TL lineshape theory [84] for nonzero T , the best TL description [18] for the Γ -Y ($k_c=0$) ARPES lineshapes was achieved for $v_\rho/v_\sigma=2$. At that time no definitive LDA value of v_F was available. If we now think of our ARPES velocity as being nearly that of v_ρ , and take our LDA velocity as an underlying “non-interacting” v_F , then for Γ -Y at least we would conclude that v_ρ is roughly $1.15v_F$, and that v_σ is roughly $0.6v_F$ [85]. A 1D Hubbard-model analysis [26] estimated $v_\sigma/v_F \approx J/2\tau$ with $J \approx 0.2 \text{ eV}$ being an effective superexchange interaction, and $\tau \approx 0.8 \text{ eV}$ being the primary k_b hopping, implying $v_\sigma/v_F \approx 1/8$.

In (c) we compare with the FS calculated in Ref. 39 using the LDA and $\text{Li}_{1.0}$ stoichiometry, thus yielding a 2% smaller $|k_b|$ -value than in the experiment. The comparison in (d) is also with the LDA FS for $\text{Li}_{1.0}$, but calculated by us with the straight LDA parameters yielding the bands in FIG. 7 (a). These two LDA results obtained with very different techniques, are seen to be quite similar. Compared with ARPES, their FS warping is too big. This is consistent with our finding (Sect. VE) that in the LDA the xy -bands are 100 meV too close to the top of the valence bands, and therefore hybridize too strongly with them. On the other hand, shifting not only the xy

energy, τ_0 , upwards by 100 meV to yield the TB bands shown in FIG.s 7(b) and 9(b), but fine-tuning the TB parameters to fit all ARPES bands further away from E_F than 0.2 eV as explained in (Sect. VIB), yields the FS with slightly too small a warping shown in FIG. 14(a). However, considering the strong dependence of the theoretical CECs on the energy position in the gap (FIG. 13) and the experimental difficulties in obtaining this kind of resolution (App. C), the agreement is, in fact, surprisingly good.

E. Discussion of FS-nesting and gapping

The FS of a metal, quasi-1D in the \mathbf{b}^* -direction, has the propensity for a $\mathbf{q} = 2k_F\mathbf{b}^*$ -instability which could be induced by a sufficiently strong interaction, I . Depending on whether this is the electron-phonon or the exchange interaction, the result would be a charge- or spin-density wave. In case $k_F = \frac{1}{4}$, this wave would be commensurate and could completely gap the FS and thus cause a metal-insulator transition. In case $k_F \neq \frac{1}{4}$, or if the interaction is not sufficiently strong, only part of the FS could be gapped away. As mentioned in the Introduction, such an instability has often been invoked to explain the resistivity upturn below 25 K, followed in most cases by the onset of superconductivity below 2 K, presumably those cases where some part of the FS remains. But despite numerous experimental attempts, no signature of commensurate order has been found. The CDW scenario was convincingly ruled out by recent NMR experiments [11], and this is consistent with our finding that the states at the Fermi level are Mo-Mo *non*-bonding with very little oxygen character (see FIG.s 3 and 2, and Sect.s III B and IV A) and, concomitantly, a very weak electron-phonon coupling. A transition to a SDW near 25 K was ruled out by muon spin-relaxation and Knight-shift measurements [12]. But since the muon appears not to be located near Mo, but near an oxygen ion to which it is bound, we find this evidence less convincing. Below, we therefore use our detailed quasi-1D bands to discuss FS nesting and band gapping. Taken together with the standard value $I = 0.54$ eV of the Stoner-like exchange parameter, calculated [80, 86–89] with local spin-density-functional theory (LSD) [52] for elemental bcc Mo, we shall find that the value, $I_{\text{WO}} \sim I/3 = 0.18$ eV, relevant for our *xy* (or *XY*) WO spreading effectively onto 3 molybdenums, fails to induce a SDW by a factor 2-3 [90].

In linear-response RPA theory the dynamical spin susceptibility of a paramagnet is:

$$\chi(\mathbf{q}, \omega) = \frac{\chi_0(\mathbf{q}, \omega)}{1 - I\chi_0(\mathbf{q}, \omega)}, \quad (29)$$

where the imaginary part of the non-interacting Lindhard susceptibility, for a band with dispersion $E(\mathbf{k})$ and the

neglect of matrix elements, has the form:

$$\text{Im } \chi_0(\mathbf{q}, \omega) = \sum_{\mathbf{k}} f(\mathbf{k}) [1 - f(\mathbf{k} + \mathbf{q})] \delta \{E(\mathbf{k}) - E(\mathbf{k} + \mathbf{q}) + \omega\} \quad (30)$$

with f being the Fermi distribution and $\sum_{\mathbf{k}}$ the average over the BZ. An instability of a paramagnet towards a static SDW with wavevector \mathbf{q} occurs if, as e.g. the temperature is lowered, the denominator in Eq. (29) with $\omega=0$ vanishes. Here, the real part of the non-interacting susceptibility is:

$$\text{Re } \chi_0(\mathbf{q}, 0) = \frac{2}{\pi} \int_0^\infty \frac{1}{\omega} \text{Im } \chi_0(\mathbf{q}, \omega) d\omega \quad (31)$$

by the Kramers-Kronig relation. The FS topology is most clearly exhibited by the value for $\omega=0$ (which is finite) of the integrand in Eq. (31). This is the nesting function, which according to Eq. (30) can be envisaged as the phase-space volume common to the "hole skin" of the \mathbf{k} -FS and the "electron skin" of the $(\mathbf{k} + \mathbf{q})$ -FS. Here, the hole skin is the one enclosed between the CECs, $E(\mathbf{k}) = E_F - \omega$ and $E(\mathbf{k}) = E_F$, and the electron skin is the one between $E(\mathbf{k} + \mathbf{q}) = E_F$ and $E(\mathbf{k} + \mathbf{q}) = E_F + \omega$. A perturbation with wavevector \mathbf{q} and magnitude Δ will couple $E(\mathbf{k})$ to $E(\mathbf{k} + \mathbf{q})$ creating a gap of size Δ around the point where $E(\mathbf{k}) = E(\mathbf{k} + \mathbf{q})$. The FS will thereby reconstruct such that the phase-space common to the hole side of the \mathbf{k} -FS and the electron side of the $(\mathbf{k} + \mathbf{q})$ -FS gets connected with the one common to the electron side of the \mathbf{k} -FS and the hole side of the $(\mathbf{k} + \mathbf{q})$ -FS.

This is illustrated for the FS of LiPB in the top and bottom panels of FIG. 15, which are turned clockwise by 90° compared with FIG. 13 in order to accommodate the correct, identical scale along \mathbf{b}^* and \mathbf{c}^* . Shown in respectively red and blue are the inner- and outer-sheet CECs, $E_j(\mathbf{k}) = E_F \pm 3$ meV, which stem from respectively the upper and lower bands, $j = u$ and l . The distance between the CECs with $E_F \pm 3$ meV is proportional to $|\mathbf{v}_{Fj}|^{-1}$ and the 3 meV is merely a conveniently small value. We have fixed \mathbf{q} at $-\frac{1}{2}\mathbf{b}^*$ ("—" because we want to keep both \mathbf{k} and $\mathbf{k} + \mathbf{q}$ in the small BZ), whereby the SDW is an antiferromagnet (AF). The coupling between the red and blue sheets can be neglected, as we shall explain in a moment. In the top panel, we see that for $E_F=53$ meV the red sheets nest around the near-crossing point, $k_c=0$ (+integer), so that with $\Delta \sim 10$ meV they will gap away for $|k_c| \lesssim 0.1$, leaving behind a long hole pocket which contains the FS fingers and extends over the region $0.1 \lesssim |k_c| \lesssim 0.9$. The blue sheets with $\Delta \sim 10$ meV are fairly unchanged. On the bottom line, we see that for $E_F=40$ meV the blue sheets nest even better than the red sheets did for $E_F=53$ meV, so that with $\Delta \sim 3$ meV they will gap away for $|k_c| \lesssim 0.3$, leaving behind an electron pocket in the region $0.3 \lesssim |k_c| \lesssim 0.7$, of maximal height $|k_b - 0.25| \lesssim 0.015$, and formed by the bulges.

Had the FS been 1D, the CECs would have been straight lines perpendicular to \mathbf{b}^* , separated $\omega/|\mathbf{v}_F|$ and with no k_c -dependence of the Fermi velocity. The nesting function would thus diverge for $\mathbf{q}=2k_F\mathbf{b}^*$ and the system would be unstable, regardless of the strength of the interaction, I . For LiPB, the length $|\mathbf{v}_F(k_c)|$ of the Fermi velocity is seen from FIG. 15 to be fairly constant and the 20% variation of $\mathbf{v}_F(k_c) \cdot \mathbf{b}^*$ shown in FIG. 14(b) is mostly due to the variation of the direction of the vector normal to the FS. The best nesting is therefore clearly for \mathbf{q} along \mathbf{b}^* .

Such a perturbation cannot mix the red upper and blue lower bands where they have pure $|\tilde{x}\tilde{y}; \mathbf{k}\rangle$ and $|\tilde{x}\tilde{y}; \mathbf{k} + \mathbf{c}^*\rangle$ character, i.e. when $k_c=0$ (+integer), and approximately where $|k_c - \text{integer}| \lesssim 0.3$, which includes the resonance regions (see FIG. 12). Moreover, as shown in App. B 2, the upper and lower bands do not mix where the $|\tilde{x}\tilde{y}; \mathbf{k}\rangle$ and $|\tilde{x}\tilde{y}; \mathbf{k} + \mathbf{c}^*\rangle$ bands are degenerate, i.e. when $k_c=0.5$, and approximately where $0.4 \lesssim k_c \lesssim 0.6$ (see top row of FIG. 16). So the mixing of the upper and lower bands via a SDW with \mathbf{q} along \mathbf{b}^* is overall small, and we shall neglect it. These exchange-split bands are given by expressions (B11)-(B13) in terms of the matrix elements (B2) of the two-band Hamiltonian.

With \mathbf{q} fixed at $-\frac{1}{2}\mathbf{b}^*$ we now comment on the doping dependence of the nesting function and, subsequently, study whether I from LSD suffices to cause instabilities. That the slight shift from 53 to 40 meV of the Fermi energy, which corresponds to a 1% decrease of the effective Li-doping, leads to a large increase of the nesting function, indicates how sensitive the nesting function is, but may, nevertheless, be realistic. Similarly, the flat parts around $k_c=0.5$ of the red sheets nest well for $E_F \sim 62$ meV, which corresponds to a 0.7% doping increase, and the bulges of the blue sheets nest a bit less well for $E_F \sim 12$ meV, which corresponds to a 3% doping decrease.

The nesting function is, however, very feeble [91, 92] and what matters for a FS reconstruction is $\text{Re } \chi_0(\mathbf{q}, 0)$, which according to Eq. (31) depends on $\text{Im } \chi_0(\mathbf{q}, \omega)/\omega$ for *all* ω . What often matters is not even the *linear* response, but the bare, static "large-signal" susceptibility, m/Δ , which for a given strength, Δ , of the perturbation (shifting the energy of the $\tilde{x}\tilde{y}$ WO by $\pm\Delta/2$ upon \mathbf{b} -translation from one Mo1 to the next) yields the bare band-structure response, $m(\Delta)$, the sublattice magnetization. The self-consistency condition for a stable solution of the LSD functional is then expressed as: $m(\Delta)/\Delta = 1/I_{\text{WO}}$ in terms of the large-signal susceptibility and the value of the exchange constant. This is illustrated in the middle panel of FIG. 15 which shows the lower and upper bands, in respectively blue and red, as functions of k_b (turned by 90° with respect to the top and bottom panels) for $k_c=0, 0.25$, and 0.50 ; for $\Delta=0$ in weak lines, and for $\Delta=67\pm 3$ meV in thick lines. For the former, non-split bands we recognize from the k_c -dependence of the lower and upper bands, $E_l(k_b=0.25, k_c)$ and $E_u(k_b=0.25, k_c)$ in the middle panel

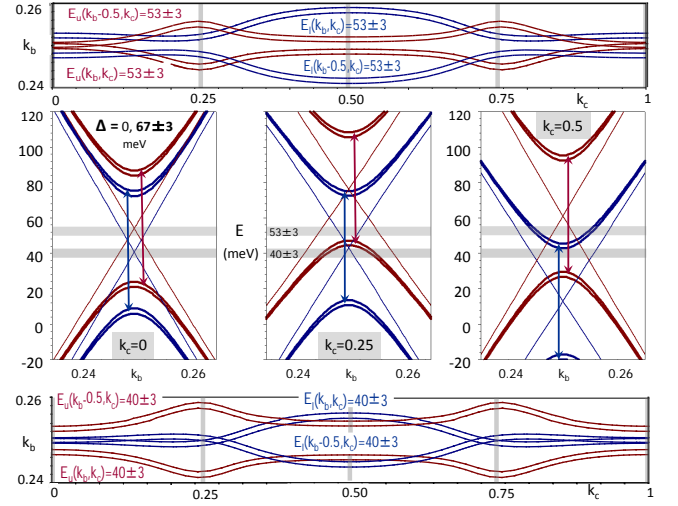


FIG. 15. FS nesting (top and bottom panels) and band gap opening (middle panels) for $\mathbf{q}=-0.5\mathbf{b}^*$ and $\Delta=0$ (thin) and 67 ± 3 meV (thick). The FS sheet of the upper (*u*) band is red and that of the lower (*l*) band is blue (see FIGs. 12 and 13). Unlike in FIG. 13, the FS is here not distorted. The Fermi levels, 53 and 40 meV, chosen in respectively the top and bottom panels correspond to the respective stoichiometries $\text{Li}_{1.00}$ and $\text{Li}_{0.99}$. An SDW with \mathbf{q} along \mathbf{b}^* does (hardly) couple those two bands. The two-band Hamiltonian (B2) with ARPES-refined parameters and selfconsistent E was used. Expressions (B11)-(B13) were used for the gapped bands. See text.

of FIG. 12, the crossing of the blue $E_l(\mathbf{k})$ and $E_l(\mathbf{k} + \mathbf{q})$ bands at $E=41, 43$, and 12 (bulge) meV, and of the red $E_u(\mathbf{k})$ and $E_u(\mathbf{k} + \mathbf{q})$ bands at $E=55, 77$ (peak), and 61 meV. The bands gapped by Δ are, for $k_b=0.25$, simply $E_u(0.25, k_c) \pm \Delta/2$ and $E_l(0.25, k_c) \pm \Delta/2$. This means, that in order to get an insulator (AFI; the case where no FS cut-off complicates the calculation of m/Δ) we must have each of the two bands half filled and the value of Δ such that the top (peak) of the upper majority-spin band is below the bottom (bulge) of the lower minority-spin band, i.e.: $\Delta \geq w \equiv 77 - 12 = 65$ meV, with w being the total width of the two unperturbed bands. This is achieved within the range of Δ -values, 67 ± 3 meV, used in FIG. 15 where we see the top of the red band straddle off the bottom of the blue band at the energy $E_F=45$ meV. The Δ -value 65 meV is presumably what gives the smallest value of Δ/m and, hence, of the I_{WO} -value required for an AFI solution. The sublattice magnetization for this AFI is the average of the BZ averages of the spin polarizations, $\partial E_{j,\text{maj}}(\mathbf{k})/\partial(\Delta/2)$, from the two ($j=l, u$) full majority bands. The sublattice magnetization is the average of (rather than the sum over) the magnetizations from the two bands because there are two sublattices (ribbons) per primitive cell. In the middle panel of FIG. 15, the spin polarization is proportional to the area between the bands for respectively $\Delta=70$ and 64 meV and the integral over k_b can therefore be calculated simply by assuming that the $\Delta=0$ band disperses

like $-(W/2)\cos 2\pi k_b$, with the effective bandwidth, W , being the one which yields the proper band slope, i.e. Fermi velocity projected onto the b^* direction (28). For $v_F=4.6\text{ eV}\text{\AA}$, $W=1.67\text{ eV}$, but it varies with the band and k_c , as seen in FIG. 14(b) and described after Eq. (28).

The sublattice magnetization, m , contributed by a majority-spin band is thus given by the elliptic integral,

$$\frac{m(\Delta)}{\Delta} = \frac{4}{W} \int_0^{k_F} \frac{dk_b}{\sqrt{(\Delta/W)^2 + (\cos 2\pi k_b)^2}}, \quad (32)$$

with k_F being that k_b -value on the reconstructed FS which lies between 0 and $\frac{1}{4}$. For a full majority-spin band ($k_F=\frac{1}{4}$), the sublattice magnetization tends to $1\mu_B$ for $\Delta/W \rightarrow \infty$. The magnetization contributed by a full majority-spin band and the minority-spin band filled to the same k_F , is also given by Eq. (32).

With $\Delta=w=65\text{ meV}$, this yields for the effective bandwidths and for the susceptibility contributions from three k_c -values and the upper and lower bands:

AFI, $\Delta=65\text{ meV}$ $k_c=0$ $=0.3$ $=0.5$				
$E_F \sim 45\text{ meV}$				
W_u [eV]	1.63	1.45	1.67	
m_u/Δ [μ_B/eV]	1.80	1.97	1.77	
W_l [eV]	1.74	1.38	1.60	
m_l/Δ [μ_B/eV]	1.71	2.05	1.83	

(33)

Here, the susceptibility variations are solely due to the variations of the effective bandwidths which, themselves, are proportional to the Fermi velocities shown in FIG. 14(b). So the resonances around $k_c=0.3$, where the velocities dips, contribute most to the susceptibility, and the regions around $k_c=0.5$ for the upper –and around $k_c=0$ for the lower– band contribute the least. Averaging over the three k_c -values yields: $m/\Delta=1.85\mu_B/\text{eV}$ and, hence, $m(65)=0.120\mu_B$ for both bands. The condition, $\Delta = mI_{\text{WO}}$, that the AFI is a stable solution is, however, far from being satisfied: With the *atomic* value: $I = 0.54\text{ eV}$, we must for m use the magnetization per atom, which is about 3 times smaller than the sublattice magnetizations because the $\tilde{x}\tilde{y}$ WO is spread over about 3 molybdenums (see FIG. 3 and Sect. IV A). Alternatively, we may for m use the sublattice magnetization and $I_{\text{WO}} \sim I/3=0.18\text{ eV}$ for the interaction parameter. In any case: $I_{\text{WO}} m/\Delta=0.18\times 1.85=0.33$, which is three times too small.

Of course, the small-signal susceptibility, $\chi = m(\Delta)/\Delta$, might be larger and suffice to induce a metallic, weak antiferromagnet (AFM). Let us therefore use the same procedure as above, but take the small value: $\Delta=12\text{ meV}$ of the splitting together with $E_F=41\text{ meV}$, which corresponds to the unperturbed FS shown in the bottom panel of FIG. 15. In this case, we get the following reconstructed Fermi vectors, k_F , and, from Eq. (32),

the corresponding susceptibility contributions:

AFM, $\Delta=12\text{ meV}$ $k_c=0$ $=0.3$ $=0.5$				
$E_F = 41\text{ meV}$				
$ k_{Fu} - \frac{1}{4} $ [10^4]	25	78	37	
m_u/Δ [μ_B/eV]	1.89	1.62	1.69	
$ k_{Fl} - \frac{1}{4} $ [10^4]	0	0	57	
m_l/Δ [μ_B/eV]	2.33	2.83	1.60	

(34)

The effective bandwidths, $W_j(k_c)$, are the same as those given in Table (33). The large susceptibility values seen in the AFM table for the lower, blue band at $k_c=0$ and 0.3 are caused by the gapping around E_F at both points, and that the largest value (2.83) is at 0.3 is due to the velocity dip there. That the smallest value (1.60) is at 0.5 is due to the negative magnetization from minority-spin band forming a bulge-electron pocket detached from the blue FS. The upper, red band is gapped well above E_F , except at $k_c=0$ where the top of the red majority-spin band is merely 8 meV above and the susceptibility therefore the largest. Except near $k_c=0$, the red FS is very much like the one shown in the bottom panel of FIG. 15. Averaging over the two bands and the three values of k_c yields: $m/\Delta=1.99\mu_B/\text{eV}$, i.e. merely 8% higher than for the AFI and the stable SDW solution is still missed by a factor ~ 3 . For that reason we have not performed numerically accurate BZ-integrations, but have merely tried to provide insights.

The k_b -integral in expression (32) diverges logarithmically for $\Delta \rightarrow 0$, but only when $k_F(k_c)=\frac{1}{4}$. So if we imagine searching for a stable solution by decreasing Δ beyond the 12 meV used in our three- k_c -point AFM estimate and iterate towards selfconsistency, we must increase the number of k_c points and, unless the FS is truly 1D, we will find that $k_F \neq \frac{1}{4}$ for all points, except those where the FS is gapped. In the $\Delta=0$ limit, this is where the \mathbf{k} and $\mathbf{k} + \mathbf{q}$ FSs cross or, most favorable for an instability, touch (nest). For our band structure, the largest AF susceptibility involves the lower band which over the entire region $|k_c| \leq 0.3$, i.e. over 60% of the BZ, varies from merely 41 to 43 meV (FIGs. 12 and 15). To get the maximal susceptibility we thus use $E_F=42\text{ meV}$ and $\Delta=2\text{ meV}$. This gives:

AFM, $\Delta=2\text{ meV}$ $k_c=0$ $=0.3$ $=0.5$				
$E_F = 42\text{ meV}$				
$ k_{Fl} - \frac{1}{4} $ [10^4]	0	0	57	
m_l/Δ [μ_B/eV]	2.98	3.66	1.60	

(35)

The susceptibility contributions from the upper band are the same as for $\Delta=12\text{ meV}$ (and the slightly changed E_F) given in Table (34), and so is the contribution from the bulge part, $0.3 < k_c \leq 0.5$, of the lower band. What has changed, is the contribution from the nested part of the lower band. Giving each k_c -point and band the same weight, which is appropriate in this case because it assumes that the nesting region is 67%, the band and k_c -averaged susceptibility comes out as: $m/\Delta =$

2.24 μ_B/eV , which is 13% larger than for $\Delta=12$ meV, but still less than half the value $1/I_{\text{WO}} = 5.6 \mu_B/\text{eV}$ needed for an SDW.

The standard computational procedure is to use the linear-response equations (30) and (31), but we doubt that this is a valid procedure for the present case: We first express the k_b -integral (32) as the one from $k_b=0$ to $\frac{1}{4}$, and then subtract the one from $k_F(k_c)$ to $\frac{1}{4}$. Both k_b -integrals diverge for $\Delta \rightarrow 0$, but that does not prevent us from averaging over k_c for fixed Δ , because only the last k_b -integral depends on $k_F(k_c)$. If we linearize $\cos 2\pi k_b$ around $k_b=\frac{1}{4}$, which is an excellent approximation in our case where $k_F(k_c)$ is close to $\frac{1}{4}$, this k_b -integral becomes:

$$\frac{2}{\pi W} \ln \left(x + \sqrt{1+x^2} \right) \approx \frac{4}{\Delta} \left| k_F(k_c) - \frac{1}{4} \right|, \quad (36)$$

with $x \equiv 2\pi \left| k_F - \frac{1}{4} \right| \frac{W}{\Delta}$. Here, the last approximation holds to order x^2 and expresses the reduction of the susceptibility (32) from its 1D value in terms of the deviation of the FS from its 1D value, $k_F(k_c)=\frac{1}{4}$. The latter can be read off from the top ($\text{Li}_{1.00}$) and bottom ($\text{Li}_{0.99}$) panels in FIG. 15 for the red inner and blue outer FS sheets, provided that Δ is so small that FS reconstruction can be neglected. However, the linear (actually quadratic) approximation (36) holds only for small x and this means that, for a given FS and maximum value of $|k_F - \frac{1}{4}|$, in our case 70×10^{-4} , we must choose Δ so large that the relative error, $\frac{1}{x} \ln(x + \sqrt{1+x^2}) - 1$, is acceptable. A maximal error of 10% requires $x \leq 0.9$, i.e.: $\Delta \geq 0.049W \approx 85$ meV. But for this large value, the FS is completely gapped. So the linear-response does not work. What we must do is to k_c -average the first expression (36) with $k_F(k_c)$ being the Δ -gapped FS. This is essentially what was done leading to Table (35), but only for the three characteristic values of k_c . We may of course split up the k_c -integral (although that is not done in standard computations). For the blue lower band, $k_c \leq 0.3$ and $E_F=41$ meV, we only need $\max |k_F - \frac{1}{4}| = 10 \times 10^{-4}$, i.e. 7 times smaller than for the entire k_c -range and, hence, $\Delta \geq 0.007W \approx 12$ meV, which within 10% does provide the correct susceptibility, as we have seen.

When Δ becomes very small, not only the k_a -dispersion, but also various scatterings must be included.

If k_F deviates substantially from $\frac{1}{4}$, the FS may be gapped by spin spiral (see App. B 2) with $\mathbf{q} = 2k_F\mathbf{b}^*$, which therefore seems to be the most stable type of spin order. Since the formalism is basically the same as the one used above, we expect our band structure to show the same robustness against spin-spiral formation as found for the AF, except maybe in overdoped samples because with increased doping the lower band becomes increasing flat –albeit over a decreasing range– around $k_c=0$ (see FIG.s 12 and 16, and App. B 1 g).

VII. CONCLUSION AND IMPLICATIONS

In conclusion, we have presented in great detail the electronic structure of $\text{LiMo}_6\text{O}_{17}$ that is experimentally obtainable using ARPES, emphasizing the degree of one-dimensional behavior of the bands in the vicinity of E_F and the excellent overall agreement with the LDA band structure. With the aim of fully describing and understanding the metallic bands found in the ARPES experiment, especially the details of FS splitting and warping, the LDA electronic structure was downfolded to a tight-binding description with three Mo1-centered t_{2g} Wannier orbitals (WOs) per formula unit using the newly developed full-potential version of the NMTO method. This description is based on analyzing the LiPB crystal structure (FIG. 1) as built from corner-sharing MoO_6 octahedra forming a staircase running along \mathbf{c} of bi-ribbons extending along \mathbf{b} .

The six t_{2g} WOs per primitive cell accurately describe not only the four bands seen by ARPES, but all six bands in the 1 eV neighborhood of E_F . This band structure (FIG. 2) is basically 2D and formed by the xy , xz , and yz WOs (FIG.s 3 and 6) giving rise to three 1D bands running along respectively \mathbf{b} , $\mathbf{c}+\mathbf{b}$, and $\mathbf{c}-\mathbf{b}$, i.e. at a 120° angle to the two other bands (FIG.s 5 and 9). The dimerization from $c/2$ to c of the ribbons into bi-ribbons gaps the xz and yz bands and leaves the xy band metallic in the gap, but resonantly coupled to its edges and, hence, to the $\mathbf{c}+\mathbf{b}$ and $\mathbf{c}-\mathbf{b}$ directions (FIG. 4). Inclusion of the xz and yz bands is indispensable to describe the strong indirect contributions to the k_c -dispersion and splitting of the metallic xy bands. These are most prominent (see FIG.s 5, and 9-15) at the crossing of the xy -band CECs running parallel to the $\text{P}_1\text{Q}_1\text{P}'_1$ -line in reciprocal space with those of the xz and yz V&C-band edges along respectively ZY' and ZY . All the ARPES-measured dispersions as well as the FS indeed confirm the resonant indirect couplings and thus the essential need for the six-band picture. The TB bands are very well described by a fully analytic 6×6 Hamiltonian with parameters optimized to match the ARPES data. Finally, the mix of direct and resonant indirect couplings along the \mathbf{c} -direction can be explicitly displayed by further analytical downfolding to the effective 2×2 Hamiltonian (B2). This and direct observation by ARPES is compelling evidence for the existence of pronounced resonance structures near E_F in LiPB.

Our results have several important implications for the issues posed in the Introduction. We begin with four straightforward points that flow directly from the central content of the paper, our new knowledge and understanding of the size of the splitting and perpendicular dispersions of the quasi-1D bands in the gap (FIG. 12), especially the indirect resonance contributions.

First, the reality of the resonance contributions casts serious doubts on theoretical descriptions based on TB bands which are smooth like the green ones in FIG. 12, i.e. casts doubt on all previous TB and TL models. Fur-

ther, in constructing an appropriate many-body Hamiltonian, it should be taken into serious consideration that with ARPES we have now been able to follow the resonance peak induced by the valence-band to energies nearly 150 meV below the Fermi level (FIG. 9) and, there, find the peak to have a magnitude of about 50 meV, as predicted by the LDA, cf. FIG. 11(c2).

Second, the general magnitude of the t_{\perp} -hoppings would suggest that 1D to 3D crossover should occur for T as high as at least 150 K, unless thwarted by the theoretically expected strong downward low- T renormalization due to LL fluctuations on the chains, as pointed out in the Introduction. However, the good agreement between LDA and ARPES data at $T=6$ K implies that this renormalization does not take place. This circumstance is not only puzzling, given the evidence for LL effects on the chains at high T , but eliminates one very attractive explanation for the exceptional stability of quasi-1D behavior in this material. We will return below to this stability issue.

Third, the coupling of the quasi-1D bands to the V&C bands cause the details of the FS splitting and warping (FIG. 13) to depend strongly on the position of E_F which in turn depends on the Li concentration. This implies that any property sensitive to the details of the FS will be very sensitive to the stoichiometry. One can then speculate that this FS sensitivity is connected to the sample dependence of the SC, especially if the SC is the product of the quasi-1D nature of the FS. We have already noted that the actual position of E_F in LiPB is such as to maximize the quasi-1D nature of the FS. This could be an important addition to the various previous theories of the SC [32–34, 36, 37].

Fourth, the spatial dependence of the t_{\perp} -hoppings argues strongly against coupled ladder models of the chains. At the simplest level the magnitude of the direct terms for hoppings within and between primitive cells (bi-ribbons) (Sect. IIIB and App. B1b) differ by less than a factor of two, respectively, $t_{\perp,1} \equiv -(t_1 + u_1) = 14$ meV and $t_{\perp,2} \equiv -(t_1 - u_1) = 8$ meV [28]. Just this would leave the ladders not very well defined as separable objects. But, much more importantly, the range of the indirect contributions (App. B1d) is at least an *order of magnitude* longer and even depends crucially on the position of the \tilde{xy} bands in the gap. We conclude that modeling the chains as separable weakly coupled ladders is very unrealistic.

Next we return to the question raised in the Introduction, whether to take a half filled or quarter filled view of the quasi-1D bands, and a closely related topic, the localization of the xy WOs. Similar to Ref. 39, our set of six WOs (Sect. IV A) describes the bonding orbitals appropriate to the half filled band below the zone-boundary dimerization gap in the k_b -direction. Each xy WO is spread onto the 4 corner-sharing MoO_6 octahedra of a ribbon, with more weight on the central Mo1 and Mo4 atoms forming the central zigzag chain, and less weight on the peripheral Mo2 and Mo5 atoms. To this spread in-

side the 70% WO contour shown in FIG.s 3 and 6 comes the 30% in a tail which extends many lattice constants along \mathbf{b} and causes the long-ranged hopping expressed by Eq.s (A2) and (A8). As seen from Eq.s (A3) and (A10), the 30% outside the contours for xz and yz WOs do not form such long-ranged tails. Further, as explained in App. B, the Löwdin-downfolded WOs (B1) appropriate for the final \tilde{xy} bands that describe ARPES so well, are exceedingly delocalized along $\mathbf{c} + \mathbf{b}$ and $\mathbf{c} - \mathbf{b}$, and depend strongly on the energy position of the bands in the gap. For numerical calculations, they are unsuitable. More localized xy WOs, as would be needed for the quarter filled view that includes also the band above the dimerization gap and interatomic Coulomb repulsions V , could be obtained by enlarging our set to 12 orbitals, placing t_{2g} (xy) NMTOs not only on Mo1, but also on Mo4 (Sect. IV B). This set could then be Löwdin downfolded analytically to the desired four-band Hamiltonian. In order to obtain atomically localized WOs, one would need to place t_{2g} NMTOs also on Mo2, and maybe even on Mo5, thus enlarging the set to 18 or even to 24 WOs per cell. Which might be more appropriate for many-body models of LiPB entails the extent to which dimerization due to covalency suppresses [30] the tendency of V -type Coulomb interactions to cause $4k_F$ charge fluctuations. For their set of 4 Wannier functions, Aichhorn and Nuss [39] found for the on-orbital Coulomb energy (U) an upper bound in the range of 0.7 eV to 1.5 eV. Although not large, this upper limit still permits V -values that are larger than the 0.8 eV dimerization gap, as indeed are contemplated in the quarter-filling models.

Without serious calculations of the Coulomb interactions and their range, calculations that have not yet been made but should be, we cannot absolutely disprove the merit of the quarter filling scenarios. But we can say that there is no evidence from our detailed comparison of ARPES and theory for the 1D xy bands near and at E_F that the Coulomb interactions are able to disrupt the strong covalent bonding that leads to the FS features that we have elucidated. Indeed it took only small refinements of the parameter values to bring our TB Hamiltonian into complete agreement with the ARPES bands up to 150 meV below the Fermi level, so we know that the Coulomb correlation effects on the energy bands are quantitatively small. As pointed out already, our final \tilde{xy} bands are exceedingly delocalized. The corresponding values of Coulomb interaction will be very much reduced and much longer range, relative to those of the bonding WOs of our 6-WO set, and even more so relative to those of the 12-WO site-based set described in the preceding paragraph. Roughly we expect that a set reduced in size by a factor of n will be n times less localized, with U about n times smaller, implying for our final 2-orbital set relative to the 4-orbital set of Nuss and Aichhorn [39] (to our 6-orbital set), a reduction of $2/4=1/2$ ($2/6=1/3$), implying upper limit interaction values for U and therefore also V that are well less than the xy dimerization gap in the k_b direction [93]. We thus argue generally

that the quasi-1D bands are better thought of in a weak coupling limit, with weak, long-range Coulomb interactions, rather than in a strong-coupling Hubbard ladder model with large short-range interactions U and V . I.e., low dimensionality itself is the driving force for many-body effects. Such a view deserves serious consideration for the modeling of LiPB.

In spite of the considerable differences from the viewpoint of previous strong-coupling Hubbard ladder models, our proposed new view can nonetheless match one of the important achievements [25, 26] of these models, rationalizing the large experimental values of the anomalous exponent $\alpha \approx 0.5 - 0.9$ [94]. It is theoretically well-known [95] that a long range (but screened) Coulomb interaction between the chains of a lattice of chains easily produces such enhanced α values. From our previous low-temperature ARPES measurements we can deduce a low-temperature Fermi velocity v_F in the range 3.5 to 5 eV Å and thus evaluate the interaction parameter $e^2/(\pi\hbar v_F)$ of Ref. [95] in the range 1.32 to 0.92. The values (A15)-(A16) obtained from our six-band Hamiltonian with ARPES-refined parameters are, respectively, 4.6 eV Å and 0.99. From FIG.1 of Ref. [95] we see that a value of α as large as the low temperature value 0.6 is very plausible. We note that the calculations leading to this figure assume a rod-like charge density along the chains rather than having the lines of pancake-like charge seen in FIG. 6 for LiPB. A very interesting project for the future would be to perform the calculation of Ref. [95] for the actual charge density of LiPB.

Within the weak coupling picture advocated here we have also found a rationale for the robust 1D nature of LiPB for T down to its SC transition. The most likely routes to 3D crossover are FS density wave instabilities. Therefore Sect. VI E presented a detailed analysis of the FS nesting and gapping that would be involved in such an instability. Because the experimental evidence against an SDW is less strong than that against a CDW, particular attention was paid there to showing that the criterion for an SDW can hardly be met. Nonetheless, because the FS instability that is most expected to lead to 3D crossover is the $2k_F$ CDW, especially for a half filled band, we now give a more detailed discussion of why this possibility does not occur.

Our essential point is that for weak coupling it has been shown [96, 97], with strong supporting experimental evidence [98], that the CDW ground state is unstable against the concomitant increase of Coulomb energy, unless this increase is offset by a reduction arising from a strong electron-phonon interaction, producing a periodic lattice distortion, i.e. a doubling from b to $2b$. However, with an average, nominal $d^{0.5}$ configuration, the Fermi level is so close to the bottom of the Mod band that the states at the FS are essentially non-bonding with Op . This is seen in more detail for the xy WO in FIG.s 3 and 6 and was described in Sect. IV A. Therefore, the electron-phonon coupling constant for the quasi-1D bands should be weak and we hope that fu-

ture DFT calculations will check this. Moreover, the additional warping and splitting of the FS caused by the coupling to the xz and yz valence and conduction bands (FIG. 13) greatly weakens the $2k_F$ susceptibility as shown in Sect. VI E. In order to be able to compare the nesting properties of our FS with those calculated for the quasi-1D compounds MMo_3Se_2 , we must use the same crude measure, $\lambda_c = 1/\{2[1 + \ln(W/w)]\}$, of the critical coupling constant needed to produce a $2k_F$ instability. For the above-mentioned metals, it was found that $\lambda_c=0.11$ for the metals $M=Ti$ and In , and $\lambda_c=0.07$ for the insulator $M=Rb$ [99]. For LiPB and $q=2k_F=\frac{1}{2}$, FIG. 12 with $k_b=0.25$ yields: $W/w=1670/34$ and, hence: $\lambda_c=0.102$ for the directly-coupled green bands, and for the black bands: $W/w=1670/64$ and, hence: $\lambda_c=0.117$. This is consistent with our conclusion that LiPB is robust against CDW formation, and that the indirect couplings make it more so [100].

We conclude that the origin of the unusual robustness of quasi-1D behavior in LiPB is in a sense not profound, but can be found in our new understanding of the basic electronic structure. This robust behavior then provides a nearly unique opportunity to study how perpendicular single particle hopping modifies single chain LL behavior if simple 3D crossover does not occur. The efforts to understand the resulting behavior are still ongoing and we hope that our new knowledge and highly portable description of the electronic structure will contribute to this effort.

ACKNOWLEDGMENTS

We are indebted to Tanusri Saha-Dasgupta, Sashi Satpathy, and Zoran Popovic for their active participation at the initial stage of this project.

We are pleased to acknowledge the early contributions to this research made by G.-H. Gweon, whose 1999 University of Michigan doctoral thesis [94] first presented the weak-coupling explanation of the large α value using the ideas of Ref. 95, that we have included in the present paper. JWA acknowledges past support of this work by the U.S. National Science Foundation (grant DMR-07-04480), and very valuable discussions with J.-P. Pouget, J. Merino, and J. V. Alvarez concerning the motivation for modeling the 1D xy bands as quarter filled.

This research used resources of the Advanced Light Source, which is a DOE Office of Science User Facility under contract no. DE-AC02-05CH11231. MG acknowledges support by NSF-DMR-1507252 grant.

Appendix A: Six-band TB Hamiltonian

1. Sublattice representation

With the definitions and notations given in Sect.s III and IV, the TB Hamiltonian in the representation of the

six Bloch sums (4) of the three t_{2g} WOs on the lower string, $xy(\mathbf{k}, \mathbf{r})$, $xz(\mathbf{k}, \mathbf{r})$, $yz(\mathbf{k}, \mathbf{r})$, and the three on the upper string, $e^{\pi i(k_c+k_b)}XY(\mathbf{k}, \mathbf{r})$, $e^{\pi i(k_c+k_b)}XZ(\mathbf{k}, \mathbf{r})$, $e^{\pi i(k_c+k_b)}YZ(\mathbf{k}, \mathbf{r})$, is:

H	xy	XY	xz	XZ	yz	YZ
xy	τ	$t - iu$	$\alpha + i\gamma$	$a - ig$	$\bar{\alpha} + i\bar{\gamma}$	$\bar{a} - i\bar{g}$
XY	$t + iu$	τ	$a + ig$	$\alpha - i\gamma$	$\bar{a} + i\bar{g}$	$\bar{\alpha} - i\bar{\gamma}$
xz	$\alpha - i\gamma$	$a - ig$	0	$A - iG$	$\lambda - i\mu$	$l - im$
XZ	$a + ig$	$\alpha + i\gamma$	$A + iG$	0	$l + im$	$\lambda + i\mu$
yz	$\bar{\alpha} - i\bar{\gamma}$	$\bar{a} - i\bar{g}$	$\lambda + i\mu$	$l - im$	0	$\bar{A} - i\bar{G}$
YZ	$\bar{a} + i\bar{g}$	$\bar{\alpha} + i\bar{\gamma}$	$l + im$	$\lambda - i\mu$	$\bar{A} + i\bar{G}$	0

(A1)

using simplified labelling of the rows and columns. The six WOs are real-valued and shown in FIG. 6; they are formally located on Mo1 and MO1. The common \mathbf{k} -dependent phase factor, $e^{\pi i(k_c+k_b)}$, multiplying the Bloch sums (4) of the upper-string WOs has been included in order that matrix-elements between the two different sublattices take the simple form (A1) where the asymmetry between integrals for hopping in- and outside a bi-ribbon (electronic dimerization) is given by the imaginary part.

The quantities named by Greek and Latin letters are real-valued functions of the Bloch vector, $\mathbf{k} = k_b\mathbf{b}^* + k_c\mathbf{c}^*$. Specifically:

$$\begin{aligned} \tau(k_b) &= \tau_0 + 2 \sum_{n=1} \tau_n \cos 2\pi n k_b, \\ t(\mathbf{k}) &= (2t_1 \cos \pi k_b + 2t_2 \cos 3\pi k_b) 2 \cos \pi k_c, \\ u(\mathbf{k}) &= (2u_1 \cos \pi k_b + 2u_2 \cos 3\pi k_b) 2 \sin \pi k_c, \end{aligned} \quad (\text{A2})$$

which describe the pure xy/XY bands, and:

$$A(k) = 2A_1 \cos \pi k \quad \text{and} \quad G(k) = 2G_1 \sin \pi k, \quad (\text{A3})$$

which describe the pure xz/XZ bands when $k \equiv k_c - k_b$, and the pure yz/YZ bands when $k \equiv k_c + k_b$. An *overbar*, used when switching from an xz to a yz orbital, indicates the mirror operation $k_b \leftrightarrow -k_b$, e.g. $\bar{a}(k_b, k_c) \equiv a(-k_b, k_c)$. The hybridizations between the xy/XY and the xz/XZ bands are given by the Bloch sums:

$$\begin{aligned} \alpha(\mathbf{k}) &= \alpha_0 + 2\alpha_1 \cos 2\pi k_b + 2\alpha_2 \cos 2\pi k_c \\ &\quad + 2\alpha_3 \cos 2\pi(k_c + k_b) + 2\alpha'_3 \cos 2\pi(k_c - k_b), \\ a(\mathbf{k}) &= 2a_1 \cos \pi(k_c - k_b) + 2a'_1 \cos \pi(k_c + k_b) \\ &\quad + 2a_2 \cos \pi(k_c - 3k_b) + 2a'_2 \cos \pi(k_c + 3k_b), \\ \gamma(\mathbf{k}) &= 2\gamma_1 \sin 2\pi k_b + 2\gamma_2 \sin 2\pi k_c \\ &\quad + 2\gamma_3 \sin 2\pi(k_c + k_b) + 2\gamma'_3 \sin 2\pi(k_c - k_b), \\ g(\mathbf{k}) &= 2g_1 \sin \pi(k_c - k_b) + 2g'_1 \sin \pi(k_c + k_b) \\ &\quad + 2g_2 \sin \pi(k_c - 3k_b) + 2g'_2 \sin \pi(k_c + 3k_b), \end{aligned} \quad (\text{A4})$$

and the hybridizations between the xz/XZ and yz/YZ

bands by:

$$\begin{aligned} \lambda(\mathbf{k}) &= \lambda_0 + 2\lambda_1 \cos 2\pi k_b + 2\lambda_2 \cos 2\pi k_c + 2\lambda_3 \cos 2\pi k_b, \\ l(\mathbf{k}) &= (2l_1 \cos \pi k_b) 2 \cos \pi k_c, \\ \mu(\mathbf{k}) &= 2\mu_1 \sin 2\pi k_b + 2\mu_3 \sin 2\pi k_b, \\ m(\mathbf{k}) &= (2m_1 \cos \pi k_b) 2 \sin \pi k_c. \end{aligned} \quad (\text{A5})$$

The dispersion along \mathbf{a}^* is neglected, and the Bloch sums are truncated for distances exceeding the lattice constant a , which means after the 3rd-nearest neighbors. The long-ranged $\tau(k_b)$ is an exception and will be discussed in connection with Eq. (A13). The A and G sums (A3) are converged already after 1st-nearest neighbors.

The Greek-lettered Bloch sums are over hops on the *same* sublattice, whereby their \mathbf{k} dependence is periodic in the reciprocal lattice spanned by \mathbf{b}^* and \mathbf{c}^* , e.g.

$$\alpha(k_b, k_c) = \alpha(k_b + M, k_c + N) \quad (\text{A6})$$

with M and N any integer. The Latin-lettered Bloch sums are over hops *between* the Mo1- and MO1-centered sublattices and averaged such that these Bloch sums are periodic in the double zone, but change sign upon odd reciprocal-lattice translations, e.g.

$$a(k_b, k_c) = (-)^{M+N} a(k_b + M, k_c + N). \quad (\text{A7})$$

Note the difference between α and a .

Below, we give the values in meV of the hopping integrals obtained from the first-principles LDA full-potential NMTO calculation (5), together with the (shifted) and the [ARPES-refined] values in those cases where they differ from the first-principles values:

$\tau_0 = 47$ [147]	τ_{203}	
$\tau_1 = -422$ [-477]	$\tau_5 = -11$	$\tau_9 = -2$
$\tau_2 = 47$ [87]	$\tau_6 = 8$	$\tau_{10} = 1$
$\tau_3 = -31$	$\tau_7 = -4$	$\tau_{11} = -1$
$\tau_4 = 17$	$\tau_8 = 3$	$\tau_{12} = 1$

(A8)

$t_1 = -11$	$u_1 = -3$
$t_2 = -5$	$u_2 = 1$

(A9)

$A_1 = -319$	$G_1 = -98$ [-109]
--------------	--------------------

(A10)

$\alpha_0 = 31$			
$\alpha_1 = 20$	$a_1 = -49$	$\gamma_1 = 8$	$g_1 = 1$
$\alpha_2 = -5$	$a'_1 = -8$	$\gamma_2 = -6$	$g'_1 = 5$
$\alpha_3 = 10$	$a_2 = -6$	$\gamma_3 = 2$	$g_2 = -3$
$\alpha'_3 = -4$	$a'_2 = -11$	$\gamma'_3 = -4$	$g'_2 = -11$

(A11)

$\lambda_0 = -61$	$\mu_1 = 7$
$\lambda_1 = 7$	$\mu_3 = -11$
$\lambda_2 = 22$ [15]	$l_1 = 20$
$\lambda_3 = -11$ [-5]	$m_1 = 12$ [6]

(A12)

Subscript 0 indicates an on-site energy, which is that of the WO in case the two WOs are identical, and an anisotropy energy in case they are different. Further subscripts indicate 1st, 2nd, and 3rd-nearest neighbor hops [28].

The zero of energy is chosen as the common energy of the xz , XZ , yz , and YZ WOs, i.e. the center of the gap in the approximation that the hybridizations (A5) between the xz/XZ and yz/YZ bands are neglected. In Sect. IIIB and in footnote [69] this energy was named $E_0 \sim B + 2|A_1|$. The common energy of the xy and XY WOs, i.e. the center of the unhybridized xy bands, is τ_0 with respect to that of the xz , XZ , yz , and YZ WOs.

The Fourier series (A2) for the dominating k_b dependence of the \widetilde{xy} bands in the gap, $\tau(k_b)$, converges slowly because, in contrast to the usual description (10) in terms of atomic orbitals, our Mo1-centered WO (FIG. 3) has the orbitals on Mo4 downfolded, whereby only the part below the 0.8 eV-gap of the 3.8 eV-broad xy band is reproduced. For many purposes, it suffices to linearize $\tau(k_b)$ around $k_b = \frac{1}{4} \approx k_F$ or $-\frac{1}{4}$:

$$\tau(k_b) \approx \tau_0 + 2 \sum_{n=1} (-1)^n \tau_{2n} - \left(|k_b| - \frac{1}{4} \right) 4\pi \sum_{n=0} (-1)^n (2n+1) \tau_{2n+1}. \quad (\text{A13})$$

With the values given above, the upper line of Eq. (A13) says that –neglecting FS warping and splitting– the Fermi level at *half* filling is

$$E_F \approx \tau(0.25) = -23 \text{ (77) [53] meV} \quad (\text{A14})$$

above the center of the gap. Note that this differs from the on-site xy energy $\tau_0 = 47 \text{ (147) [203]}$ by the alternating sum over the even-numbered hops in (A13). Hence, the reason why the ARPES-refined value of the Fermi level for half-filling is 150 meV below τ_0 , and thereby closer to the center of the gap than the LDA value shifted by 100 meV, is caused by the refinement of the τ_2 value. In App. C2 the k_{FB} -value measured by ARPES is 0.254 for both samples G and H. The Fermi level is thus approximately $\tau(0.254) = 75$ meV rather than 53 meV above the center of the gap. The value of the coefficient to $|k_b| - \frac{1}{4}$ in the lower line of Eq. (A13), times b , yields the Fermi velocity at half filling:

$$v_F = 4.0 \text{ (4.0) [4.6] eV \AA}. \quad (\text{A15})$$

This LDA value is a bit larger than those of Satpathy and Popovic (3.72 eV \AA) and of Nuss and Aichhorn (0.93 10^5 m/s = 3.8 eV \AA). Our ARPES-refined value, which is consistent with FIG. 14 (b) exceeds the LDA value by 15%. The dimensionless coupling constant used in Ref. [95] has the value

$$e^2 / (\pi \hbar v_F) = 1.14 \text{ [0.99]}. \quad (\text{A16})$$

The splitting-and-warping effects neglected in the above are considered in detail in Sect. VID and in App. B.

Of the matrix elements $\langle xy_0 | H | xz_n \rangle = \alpha_n \pm \gamma_n$, determining the xz and yz hybridization of the xy bands, α_0 is the on-site anisotropy energy and $\alpha_n \pm \gamma_n$ and $\bar{\alpha}_n \pm \bar{\gamma}_n$ are integrals for hopping between n th-nearest neighbors with the upper sign for forwards- and the lower for backwards hopping. Although these Greek-lettered hops are between WOs on the *same* sublattice, forwards hopping differs from backwards hopping because there is no inversion symmetry around Mo1. Except α_1 , these hopping integrals are all small, but significant for the detailed k_c -dispersion of the xy band near the Fermi level, especially the resonance behavior. The same holds for the Latin-lettered hopping integrals, $\langle xy_0 | H | XZ_n \rangle = a_n \pm g_n$, between WOs on different sublattices.

The matrix elements $\langle xz_0 | H | yz_n \rangle = \lambda_n \pm \mu_n$ and $\langle xz_0 | H | YZ_n \rangle = l_n \pm m_n$ are larger, but of minor importance for the xy band. They are decisive for the levels near Z where the V&C bands come closest. Since the Bloch sums (A5) are badly converged, we found it necessary to truncate the sum and then refine the hopping values as shown in the table above. This refinement was enabled by the fact that the Hamiltonian (A18) simplifies at the points of high symmetry such as Z .

2. $\{|\mathbf{k}\rangle, |\mathbf{k} + \mathbf{c}^*\rangle\}$ representation

While the sublattice representation is conceptually simple, the reciprocal-lattice $\{|\mathbf{k}\rangle, |\mathbf{k} + \mathbf{c}^*\rangle\}$ -representation in terms of the pseudo-Bloch sums (16) of the three t_{2g} WOs in the double zone is the more physical. With the common phase factor $e^{\pi i(k_c + k_b)}$ included in the definition of the Bloch sums of the capital-lettered real-valued WOs, the transformation (18) is simply the bonding-antibonding transformation,

$$\frac{1}{\sqrt{2}} \begin{pmatrix} 1 & 1 \\ 1 & -1 \end{pmatrix}, \quad (\text{A17})$$

for each of the three t_{2g} Bloch orbitals. Subjecting the Hamiltonian (A1) to the unitary transformation which has the three 2×2 blocks along the diagonal given by (A17) and all other matrix elements zero, yields a six-band Hamiltonian with the following form:

$$\begin{array}{c|cc} H & |\mathbf{k}\rangle & |\mathbf{k} + \mathbf{c}^*\rangle \\ \hline \langle \mathbf{k} | & h(\mathbf{k}) & \Delta(\mathbf{k}) \\ \langle \mathbf{k} + \mathbf{c}^* | & h.c. & h(\mathbf{k} + \mathbf{c}^*) \end{array}. \quad (\text{A18})$$

Here, the 3×3 t_{2g} Hamiltonian, $h(\mathbf{k})$, is:

$$\begin{array}{c|ccc} h(\mathbf{k}) & |xy; \mathbf{k}\rangle & |xz; \mathbf{k}\rangle & |yz; \mathbf{k}\rangle \\ \hline \langle xy; \mathbf{k} | & \tau(k_b) + t(\mathbf{k}) & \alpha(\mathbf{k}) + a(\mathbf{k}) & \bar{\alpha}(\mathbf{k}) + \bar{a}(\mathbf{k}) \\ \langle xz; \mathbf{k} | & \alpha(\mathbf{k}) + a(\mathbf{k}) & A(k_c - k_b) & \lambda(\mathbf{k}) + l(\mathbf{k}) \\ \langle yz; \mathbf{k} | & \bar{\alpha}(\mathbf{k}) + \bar{a}(\mathbf{k}) & \lambda(\mathbf{k}) + l(\mathbf{k}) & A(k_c + k_b) \end{array} \quad (\text{A19})$$

while the off-diagonal, upper-right block, $\Delta(\mathbf{k})$, in (A18) is given by:

$$\Delta(\mathbf{k})/i \begin{array}{c|ccc} & |xy; \mathbf{k} + \mathbf{c}^*\rangle & |xz; \mathbf{k} + \mathbf{c}^*\rangle & |yz; \mathbf{k} + \mathbf{c}^*\rangle \\ \hline \langle xy; \mathbf{k}| & u(\mathbf{k}) & \gamma(\mathbf{k}) + g(\mathbf{k}) & \bar{\gamma}(\mathbf{k}) + \bar{g}(\mathbf{k}) \\ \langle xz; \mathbf{k}| & g(\mathbf{k}) - \gamma(\mathbf{k}) & G(k_c - k_b) & m(\mathbf{k}) - \mu(\mathbf{k}) \\ \langle yz; \mathbf{k}| & \bar{g}(\mathbf{k}) - \bar{\gamma}(\mathbf{k}) & \mu(\mathbf{k}) + m(\mathbf{k}) & G(k_c + k_b) \end{array} \quad (\text{A20})$$

Note that the lower-left block of the Hermitian matrix H in (A18) is *not* $\Delta(\mathbf{k})^\dagger$; see Eq. (A21) below.

The diagonal blocks $h(\mathbf{k})$ and $h(\mathbf{k} + \mathbf{c}^*)$ are periodic in the double zone with $M + N$ respectively even and

odd. This means that $h(\mathbf{k} + \mathbf{c}^*)$ is given by expression (A19) with the sign in front of the Latin-lettered Bloch sums flipped as seen from Eq. (A7).

The diagonal blocks, $h(\mathbf{k})$ and $h(\mathbf{k} + \mathbf{c}^*)$ are real-valued and the off-diagonal blocks, given by $\Delta(\mathbf{k})$ are imaginary. The latter contain the electronic dimerizations. Since their largest elements are $G(k_c - k_b)$ and $G(k_c + k_b)$, which split the xz bands as in Eq. (15), and the yz bands in the same way, but with k_b substituted by $-k_b$, we shall in the following section derive the representation in which the xz and yz blocks are diagonal. This mixed representation is the natural one to use for downfolding the xz and yz blocks of the six-band Hamiltonian to a Hamiltonian which describes merely the two xy -like bands in the gap.

But before doing so, it is useful to write the Hamiltonian (A18)-(A20) with the rows and columns in the order: $|xy; \mathbf{k}\rangle, |xy; \mathbf{k} + \mathbf{c}^*\rangle, |xz; \mathbf{k}\rangle, |xz; \mathbf{k} + \mathbf{c}^*\rangle, |yz; \mathbf{k}\rangle, |yz; \mathbf{k} + \mathbf{c}^*\rangle$:

$$\begin{array}{cccccc} \tau + t & iu & \alpha + a & i(\gamma + g) & \bar{\alpha} + \bar{a} & i(\bar{\gamma} + \bar{g}) \\ -iu & \tau - t & i(\gamma - g) & \alpha - a & i(\bar{\gamma} - \bar{g}) & \bar{\alpha} - \bar{a} \\ \alpha + a & -i(\gamma - g) & A & iG & \lambda + l & -i(\mu - m) \\ -i(\gamma + g) & \alpha - a & -iG & -A & -i(\mu + m) & \lambda - l \\ \bar{\alpha} + \bar{a} & -i(\bar{\gamma} - \bar{g}) & \lambda + l & i(\mu + m) & \bar{A} & i\bar{G} \\ -i(\bar{\gamma} + \bar{g}) & \bar{\alpha} - \bar{a} & i(\mu - m) & \lambda - l & -i\bar{G} & -\bar{A} \end{array} \quad (\text{A21})$$

Like in Eq (A1) the argument, \mathbf{k} , of the Bloch sums of hopping integrals is omitted for brevity.

3. Mixed representation

The eigenvalues, $\pm\sqrt{A^2 + G^2} \equiv \varepsilon_C$, of the xz - xz (or yz - yz) diagonal block of the six-band Hamiltonian (A21) in the reciprocal-lattice representation –and neglecting hybridization with the xy and yz (or xz) orbitals– are the conduction (C)- and valence (V)-band energies (15). The normalized eigenvectors of this block, form the C and V columns of the unitary matrix which gives the xz C&V-band orbitals as:

$$\{ |xz_C(\mathbf{k})\rangle, |xz_V(\mathbf{k})\rangle \} = \{ |xz; \mathbf{k}\rangle, |xz; \mathbf{k} + \mathbf{c}^*\rangle \} \times \begin{pmatrix} U_C(k) & U_V(k) \\ -is(k)U_V(k) & is(k)U_C(k) \end{pmatrix}, \quad (\text{A22})$$

where $k \equiv k_c - k_b$,

$$U_V(k) \equiv \frac{1}{\sqrt{2}} \sqrt{1 \pm \frac{A(k)}{\sqrt{A(k)^2 + G(k)^2}}}, \text{ and } s(k) \equiv \text{sign}\{G(k)\}. \quad (\text{A23})$$

Since $G_1 \leq 0$, it follows from (A3) that $s(k) = -\text{sgn}\{\sin\pi(k_c - k_b)\}$.

Translation of k by 1 (i.e. \mathbf{k} by \mathbf{c}^*) has the following effects: $U_C \leftrightarrow U_V$ and $s \leftrightarrow -s$, whereby the columns of U (not to be confused with the on-site Coulomb repulsion) are exchanged as expected because they are the eigenvectors for the C&V bands. Exchanging the rows of U of course also corresponds to translating k by 1, but does bring in a phase factor which gets passed onto the C&V-band functions:

$$|xz_C(\mathbf{k} + \mathbf{c}^*)\rangle = |xz_C(\mathbf{k})\rangle is(k) \text{ and } |xz_V(\mathbf{k} + \mathbf{c}^*)\rangle = |xz_V(\mathbf{k})\rangle / is(k) \quad (\text{A24})$$

Similarly for the orbitals diagonalizing the yz -block of (A21), provided that $-k_b$ is substituted by k_b .

In the following, we shall neglect the hybridization (A5) between the xz and yz bands because this simplifies the two-band Hamiltonian considerably and is a good approximation for \mathbf{k} far away from $Z(0, \frac{1}{2})$, specifically for $|k_b| \sim k_F \sim \frac{1}{4}$. With this approximation, the unitary 6×6 matrix transforming the Hamiltonian from the reciprocal-lattice representation (A21) to the mixed representation merely has three non-zero 2×2 blocks along the diagonal: the xy block is the unit matrix, the xz block is $U(k_c - k_b)$, and the yz block $U(k_c + k_b)$.

Hence, the first four rows and columns of the Hamiltonian in the mixed representation become:

H	$ xy; \mathbf{k}\rangle$	$ xy; \mathbf{k} + \mathbf{c}^*\rangle$	$ xz_C(\mathbf{k})\rangle$	$ xz_V(\mathbf{k})\rangle$
$\langle xy; \mathbf{k} $	$\tau + t$	iu	cc	cc
$\langle xy; \mathbf{k} + \mathbf{c}^* $	$-iu$	$\tau - t$	cc	cc
$\langle xz_C(\mathbf{k}) $	$(\alpha + a)U_C + (\gamma + g)sU_V$	$is[(\alpha - a)U_V - (\gamma - g)sU_C]$	$\sqrt{A^2 + G^2}$	0
$\langle xz_V(\mathbf{k}) $	$(\alpha + a)U_V - (\gamma + g)sU_C$	$-is[(\alpha - a)U_C + (\gamma - g)sU_V]$	0	$-\sqrt{A^2 + G^2}$

(A25)

The last two (xz_C and xz_V) rows and columns, equal those given above for xz_C and xz_V , but with k_b substituted by $-k_b$. For simplicity of notation, we have dropped the argument \mathbf{k} of the matrix elements.

Appendix B: Löwdin-downfolded two-band Hamiltonian

The WOs for the two isolated xy -like bands in the gap have much longer range than the xy -WOs shown in FIG.s 3 and 6, and similarly for the elements of the effective two-band Hamiltonian as compared with the range exhibited by the Bloch sums of the six-band Hamiltonian. For this reason, we do not perform the downfolding of the xz , XZ , yz , and YZ WOs into the "tails" of the effective xy and XY orbitals, \widetilde{xy} and \widetilde{XY} , in real- but in reciprocal space. Real-space pictures of the downfolded orbitals would be unwieldy and would crucially depend on the position of the energies, E , of the bands in the gap. For the same reason, tables of hopping integrals would be unwieldy and energy dependent. For downfolding from six to two bands, we therefore use analytical Löwdin- rather than numerical (NMTO) downfolding.

With the hybridization between the xz and yz orbitals neglected, the xz and yz downfoldings are additive:

$$\{ |\widetilde{xy}; E, \mathbf{k}\rangle, |\widetilde{xy}; E, \mathbf{k} + \mathbf{c}^*\rangle \} = \{ |xy; \mathbf{k}\rangle, |xy; \mathbf{k} + \mathbf{c}^*\rangle \} + \delta_{xz} \{ |xy; \mathbf{k}\rangle, |xy; \mathbf{k} + \mathbf{c}^*\rangle \} + \delta_{yz} \{ |xy; \mathbf{k}\rangle, |xy; \mathbf{k} + \mathbf{c}^*\rangle \}.$$

Here, the perturbations involve the Green function for the xz - xz or yz - yz block of the six-band Hamiltonian times the corresponding xz - xy or yz - xy hybridization matrix. The representation chosen for the xz and yz states to be downfolded (integrated out) matters for the formalism –and, hence, for our interpretations– but not for the resulting two-band Hamiltonian. Choosing the mixed representation (A25) we get:

$$\delta_{xz} \{ |xy; E, \mathbf{k}\rangle, |xy; E, \mathbf{k} + \mathbf{c}^*\rangle \} = \frac{|xz_C\rangle}{E - \sqrt{A^2 + G^2}} (\langle xz_C | H | xy; \mathbf{k}\rangle, \langle xz_C | H | xy; \mathbf{k} + \mathbf{c}^*\rangle) + \frac{|xz_V\rangle}{E + \sqrt{A^2 + G^2}} (\langle xz_V | H | xy; \mathbf{k}\rangle, \langle xz_V | H | xy; \mathbf{k} + \mathbf{c}^*\rangle), \quad (B1)$$

and similarly for δ_{yz} . Note that the downfolded orbitals depend on the energy, E , but only through the denominators in (B1) because we have chosen the *diagonal* V&C-band representation for the xz (and yz) states.

In the representation of these downfolded \widetilde{xy} orbitals, the two-band Hamiltonian is seen to be:

$$\begin{pmatrix} \langle \widetilde{xy}; E, \mathbf{k} | H | \widetilde{xy}; E, \mathbf{k} \rangle & \langle \widetilde{xy}; E, \mathbf{k} | H | \widetilde{xy}; E, \mathbf{k} + \mathbf{c}^* \rangle \\ \text{c.c.} & \langle \widetilde{xy}; E, \mathbf{k} + \mathbf{c}^* | H | \widetilde{xy}; E, \mathbf{k} + \mathbf{c}^* \rangle \end{pmatrix} = \tau(k_b) \begin{pmatrix} 1 & 0 \\ 0 & 1 \end{pmatrix} + \begin{pmatrix} t(\mathbf{k}) & iu(\mathbf{k}) \\ -iu(\mathbf{k}) & -t(\mathbf{k}) \end{pmatrix} \quad (B2)$$

$$+ \frac{\Gamma_C(\mathbf{k})}{E - \sqrt{A^2(\mathbf{k}) + G^2(\mathbf{k})}} + \frac{\Gamma_V(\mathbf{k})}{E + \sqrt{A^2(\mathbf{k}) + G^2(\mathbf{k})}} + \frac{\bar{\Gamma}_C(\mathbf{k})}{E - \sqrt{A^2(\mathbf{k}) + G^2(\mathbf{k})}} + \frac{\bar{\Gamma}_V(\mathbf{k})}{E + \sqrt{A^2(\mathbf{k}) + G^2(\mathbf{k})}},$$

where the poles at the xz and yz C&V bands are numbers while the residues are 2×2 matrices. The residue for the perturbation by the xz conduction band is:

$$\Gamma_C(\mathbf{k}) = \begin{pmatrix} |\langle xz_C(\mathbf{k}) | H | xy; \mathbf{k} \rangle|^2 & \langle xy; \mathbf{k} | H | xz_C(\mathbf{k}) \rangle \langle xz_C(\mathbf{k}) | H | xy; \mathbf{k} + \mathbf{c}^* \rangle \\ \text{cc} & |\langle xz_C(\mathbf{k}) | H | xy; \mathbf{k} + \mathbf{c}^* \rangle|^2 \end{pmatrix}, \quad (B3)$$

and similarly for the xz valence band. These matrix elements are shown in the 4th row in FIG. 16 and their factors, the matrix elements of the xz - xy hybridization (A25), are shown in the 5th row of the figure. Remember: an overbar indicates the mirror operation $k_b \leftrightarrow -k_b$ and is used to switch from an xz to a yz orbital.

E is the energy of the xy state that we are seeking, i.e. an eigenvalue of the Hamiltonian (B2), and should therefore be found self-consistently. For states deep inside the gap, we may substitute E by $\tau(k_b)$ from Eq. (A2). Note (a)

that E is with respect to the center of the gap and (b) that it enters the two-band Hamiltonian (B2) only through the denominators of the four resonance terms. Keeping E as a free parameter therefore provides insight to study the \widetilde{xy} -bands depending on their placement in the gap and on the \mathbf{k} -dependence of the residues [101].

1. Origin of the perpendicular dispersion and splitting of the quasi-1D bands in the gap

Having verified the realism of our LDA-based TB model in Sect. VI, we now take up the thread and trace the non-trivial features of the bands and CECs shown in respectively FIG.s 12 and 13 back to the Bloch-sums (A2), $\tau(k_b)$, $t(\mathbf{k})$, and $u(\mathbf{k})$, of the xy - xy hopping integrals, to the Bloch sums (A3), $A(k_c \pm k_b)$ and $G(k_c \pm k_b)$, of the xz - xz or yz - yz hopping integrals, and to the Bloch sums (A4), $\alpha(\mathbf{k}) + a(\mathbf{k})$ and $\gamma(\mathbf{k}) + g(\mathbf{k})$, of the xy - xz hopping integrals. This is a long route, but the essence of what was learned is contained in App. B 1 g.

We start by extending FIG. 12 from the irreducible ($0 \leq k_c \leq 0.5$) to the double ($-1 < k_c \leq 1$) zone, shown in 5, in which all Bloch sums are periodic. This is done in FIG. 16 in the 1st row to the right in each of three panels for $k_b=0.225, 0.250$, and 0.275 . In the following rows, we identify and analyze the individual contributions from the direct xy - xy hops (green) and the indirect hops via the xz (blue) and yz (red) V&C bands to the diagonal and off-diagonal elements, $\langle \widetilde{xy}; \mathbf{k} | H | \widetilde{xy}; \mathbf{k} \rangle$ and $\langle \widetilde{xy}; \mathbf{k} | H | \widetilde{xy}; \mathbf{k} + \mathbf{c}^* \rangle$, of the two-band Hamiltonian (B2). We end in the 6th rows showing $\alpha(\mathbf{k}) + a(\mathbf{k})$ in purple and $\gamma(\mathbf{k}) + g(\mathbf{k})$ in turquoise.

The bands –but not their eigenvector decoration (fatness)– shown on the 1st row to the right in FIG. 16 have the proper single-zone period 1 in k_c . Where one band is fat and the other not, those bands have respectively pure $|\mathbf{k}\rangle$ and pure $|\mathbf{k} + \mathbf{c}^*\rangle$ character. This is the case for integer values of k_c , whereas for half-integer values, the two bands are of 50% mixed character. To left, we show in respectively fat and thin lines the pure $\widetilde{xy}(\mathbf{k})$ and $\widetilde{xy}(\mathbf{k} + \mathbf{c}^*)$ bands. These are the diagonal elements, $\langle \widetilde{xy}; \mathbf{k} | H | \widetilde{xy}; \mathbf{k} \rangle$ and $\langle \widetilde{xy}; \mathbf{k} + \mathbf{c}^* | H | \widetilde{xy}; \mathbf{k} + \mathbf{c}^* \rangle$ of the two-band Hamiltonian (B2) and have the double-zone period 2 in k_c .

In FIG. 16 we have for simplicity substituted E in the denominators of the resonance terms (B2) by $\tau(k_b)$. Comparison of the bands in the 1st row to the right with those in FIG. 12 demonstrate how this approximation enhances the resonance features: the peak in upper band for $k_c=0.225$ and the dip in the lower band for $k_c=0.275$.

a. Peak-, bulge-, and near band-crossing features

The *primary feature* of the \widetilde{xy} bands in the gap, the *resonance peaks*, originate from either an xz -band edge running along a blue dot-dashed line in Fig. 5, or from a yz -band edge running along a red dot-dashed line in the same figure, and are therefore located at the crossings between such a line and the \widetilde{xy} -band CEC, one of the

brown-to-olive dot-dashed lines when $k_b=0.225$ - 0.275 . In FIG. 16, these features are therefore well separated in k_c . The resonance peaks in the 1st row to the right are seen to have almost pure $|\widetilde{xy}; \mathbf{k}\rangle$ or $|\widetilde{xy}; \mathbf{k} + \mathbf{c}^*\rangle$ character, although the V&C-band edges have mixed $|\mathbf{k}\rangle$ and $|\mathbf{k} + \mathbf{c}^*\rangle$ characters, as we saw along ΛW ($k_c=\frac{1}{4}$) and $\Lambda'W'$ ($k_c=\frac{3}{4}$) in Fig. 10 (d) and (e). The strong $|\mathbf{k}\rangle$ character is what enabled us to detect with ARPES the large peak in the upper \widetilde{xy} band from the resonance with the yz valence band at $\mathbf{k}=(0.225, -0.775)$, k_c -translated to $(0.225, 0.225)$. The small peak in the lower band at $(0.225, 0.275)$, also from the resonance with the yz valence band, merely caused a shoulder-like structure [see FIG. 11 (c2)].

Quite differently for the *secondary feature* seen around the BZ boundaries, $k_c=\pm\frac{1}{2}$, to the right in the 1st row in FIG. 16. This feature consists of a *bulge* in the lower band and the concomitant filling-in of the valleys between the neighboring resonance peaks repelled from xz and yz V or C bands, whichever is closer in energy. These neighboring resonance peaks are therefore in the upper \widetilde{xy} band when $k_b=0.225$ and 0.250 , and (over-enhanced) in the lower \widetilde{xy} band when $k_b=0.275$. The bulge is caused by the hybridization between the $\widetilde{xy}(\mathbf{k})$ and $\widetilde{xy}(\mathbf{k} + \mathbf{c}^*)$ bands (displayed to the left) which cross at the BZ boundaries, $k_c=\pm\frac{1}{2}$, and split by $\pm |\langle \widetilde{xy}; \mathbf{k} | H | \widetilde{xy}; \mathbf{k} + \mathbf{c}^* \rangle|$. The latter, off-diagonal matrix element of the two-band Hamiltonian (B2) is shown in black in the 2nd row to the right. This element is seen to attain its largest absolute value near $k_c=\pm\frac{1}{2}$ and, here, to have equal contributions from the indirect hops via the xz (blue) and yz (red) bands, and to be amplified by the direct xy - xy (green) contribution. To the left, and in the same colors, are shown the diagonal element, $\langle \widetilde{xy}; \mathbf{k} | H | \widetilde{xy}; \mathbf{k} \rangle$, and its three contributions.

Also the *third characteristic feature* of the \widetilde{xy} bands, the *conspicuous crossing* of the bands and FS sheets on the ΓY and $\Gamma'Y'$ lines, $k_c=-1, 0, 1$, is connected with the hybridization between the $\widetilde{xy}(\mathbf{k})$ and $\widetilde{xy}(\mathbf{k} + \mathbf{c}^*)$ bands, but with its zero rather than its maximum. In ARPES [FIG. 11(c2)], as well as in previous calculations, an apparent crossing on the ΓY line was noted [23] and a TB description attempted [26]. With our much higher resolution, this peculiarity is now seen in FIG.s 13 (d), 12, and 16 as an anomalously small splitting, in particular for $k_b=0.275$ where the contrast to the huge hybridization-caused splitting around $k_c=\pm\frac{1}{2}$ is the largest. The splitting at integer k_c is even *smaller* than that of the directly-coupled, green bands. This is simple to understand: First of all, the splitting, $2t(\mathbf{k}) = 8(t_1 \cos \pi k_b + t_2 \cos 3\pi k_b)$, of the green bands decreases from 46 meV for $k_b=0.225$ to 24 meV for $k_b=0.275$. Secondly, along ΓY ($k_c=0$) the $xy(\mathbf{k})$, $xz(\mathbf{k})$, and $yz(\mathbf{k})$ bands –approximately given

by respectively Eq.s (11), (13), and (12)– are all bonding between ribbons while the $xy(\mathbf{k} + \mathbf{c}^*)$, $xz(\mathbf{k} + \mathbf{c}^*)$, and $yz(\mathbf{k} + \mathbf{c}^*)$ bands are all antibonding. Since both xy bands in the gap lie above the $xz(\mathbf{k})$ and $yz(\mathbf{k})$ bands, but below the $xz(\mathbf{k} + \mathbf{c}^*)$ and $yz(\mathbf{k} + \mathbf{c}^*)$ bands, the valence bands will push the bonding $xy(\mathbf{k})$ band up, and the conduction bands will push the antibonding $xy(\mathbf{k} + \mathbf{c}^*)$ band down in energy. Hence, the hybridization with the xz and yz V&C bands will *diminish* the separation between the xy bands [102]. This is clearly seen in the 1st and 2nd rows of FIG. 16. The repulsion from the V band, seen in the figures as the distance of the lower black band above that of the lower green band, decreases with increasing k_b because the distance of the \widetilde{xy} -band energy, $\tau(k_b)$, above the energy of the V band increases (see 3rd row to the left in FIG. 16), and this enters the V-band denominators in the two-band Hamiltonian (B2). By the same reasoning, the repulsion from the C band, seen as the distance of the upper black band below that of the upper green band, should *increase* with k_b and become large when at $k_b=0.275$ the \widetilde{xy} -band is close to the V band at integer k_c . This is also what the figures show, albeit not to the expected extent, so we shall return to this in App. B 1 g.

We now proceed to identify the different terms of the two-band Hamiltonian (B2):

b. Directly coupled terms

Its 1st term, the energy $\tau(k_b)$ of the two degenerate 1D intra-ribbon xy bands, is included only in the 1st row of FIG. 16, where it is the average of the two green, directly-coupled xy bands, unhybridized (left) or hybridized (right). This average is independent of k_c . In the 2nd row to the left, $\tau(k_b)$ is neither included in the green, directly-coupled $xy(\mathbf{k})$ band, nor in the black, directly plus indirectly-coupled $\widetilde{xy}(\mathbf{k})$ band.

The 2nd term in Eq. (B2) is the xy -block of the six-band Hamiltonian (A21) and it gives the perpendicular dispersions and splitting of the green xy bands shown in the 1st row in FIG. 16. The corresponding diagonal, \mathbf{k} -conserving, and off-diagonal, $(\mathbf{k}, \mathbf{k} + \mathbf{c}^*)$ -coupling, matrix elements, $t(\mathbf{k})$ and $iu(\mathbf{k})$, are the Bloch sums of respectively the average xy -XY hoppings and their dimerizations [28]. They are given in Eq. (A2) and are shown in green in the 2nd row to respectively the left and the right. These Bloch sums of direct hoppings are seen to depend little on k_b in the $\pm 10\%$ interval around k_F .

Also the TB model [26] upon which current TLL theories [31][35] are based, includes 1st- and 2nd-nearest-neighbor terms. But in the attempt to fit the peak, bulk, and band-crossing features of the LDA FS [23] without recognizing their resonant nature, the resulting TB model had an unphysical form (containing e.g. $\sin \pi k_c$ and $\sin 2\pi k_c$ terms) and, as a consequence, its parameter values are incompatible with ours. That the magnitude of its FS warping is several times ours is partly because the

stoichiometry was taken to be $\text{Li}_{0.90}$ rather than $\text{Li}_{1.02}$.

c. Symmetries

The green, directly-coupled and the black, directly plus indirectly-coupled $|\mathbf{k}\rangle$ bands shown to the left in the 2nd row are even around $k_c=-1,0$, and 1. The green and black matrix elements shown to the right couple each of these bands to itself after k_c -translation by 1. These off-diagonal elements, divided by i , are odd around $k_c=-1,0,1$ and even around $k_c=\pm 0.5$. The indirect couplings alone, i.e. the perturbations of the \widetilde{xy} -band Hamiltonian by the xz or yz V&C bands, are shown respectively in blue and red. They are related to each other by a sign change of k_b [77], and those blue and red curves to the left/right are related to each other by a mirror/anti-mirror operation around $k_c=-1,0,1$. Moreover, each of the blue and the red curves to the right change sign upon k_c -translation by 1, i.e. they are anti-periodic [see Eq. (B6)].

d. Indirectly coupled terms; role of the denominators

The indirect couplings via the xz and yz bands are additive and given by respectively the 3rd&4th and the 5th&6th terms in expression (B2), provided that the hybridization between the xz and yz bands, i.e. the (A5) hoppings, can be neglected, as is the case when $|k_b|$ is in the $\pm 10\%$ interval around $k_F \sim \frac{1}{4}$. The perturbations via the xz and yz bands have been subdivided into V and C bands whereby each of them takes the form of a single resonance (pole) with the nominator (residue) being a 2×2 matrix with period 2 in k_c , see Eq. s (B3) and (A25), and the denominator, a period-1 scalar function which is the energy distance between the \widetilde{xy} band and one of the four xz or yz V or C bands. The energy of the former is $E[\sim \tau(k_b)]$ and that of one of the latter is given by Eq. (15) for ε_{xz} and by the same equation, but with k_b substituted by $-k_b$, for ε_{yz} .

From now on, we shall take advantage of the mirror/anti-mirror symmetries between the blue xz - and the red yz perturbations of the two-band Hamiltonian mentioned in App. B 1 c to consider merely the blue xz perturbation, which we shall trace back from the 2nd row to the Bloch sums (A3) of xz - xz hopping integrals in the 3rd row, and to the Bloch sums (A4) of xy - xz hopping integrals in the 6th row.

The most important factor influencing the shapes of the diagonal and off-diagonal matrix elements shown in blue on the 2nd row to the left and the right, and given by the 3rd&4th terms in Eq. (B2), is their common denominator. This is the distance between the \widetilde{xy} bands and the xz valence- or conduction band shown to the left in the 3rd row, with the \widetilde{xy} bands in black and the xz V and C bands in respectively dark and light blue. Also shown are the yz V and C bands in dark and light red,

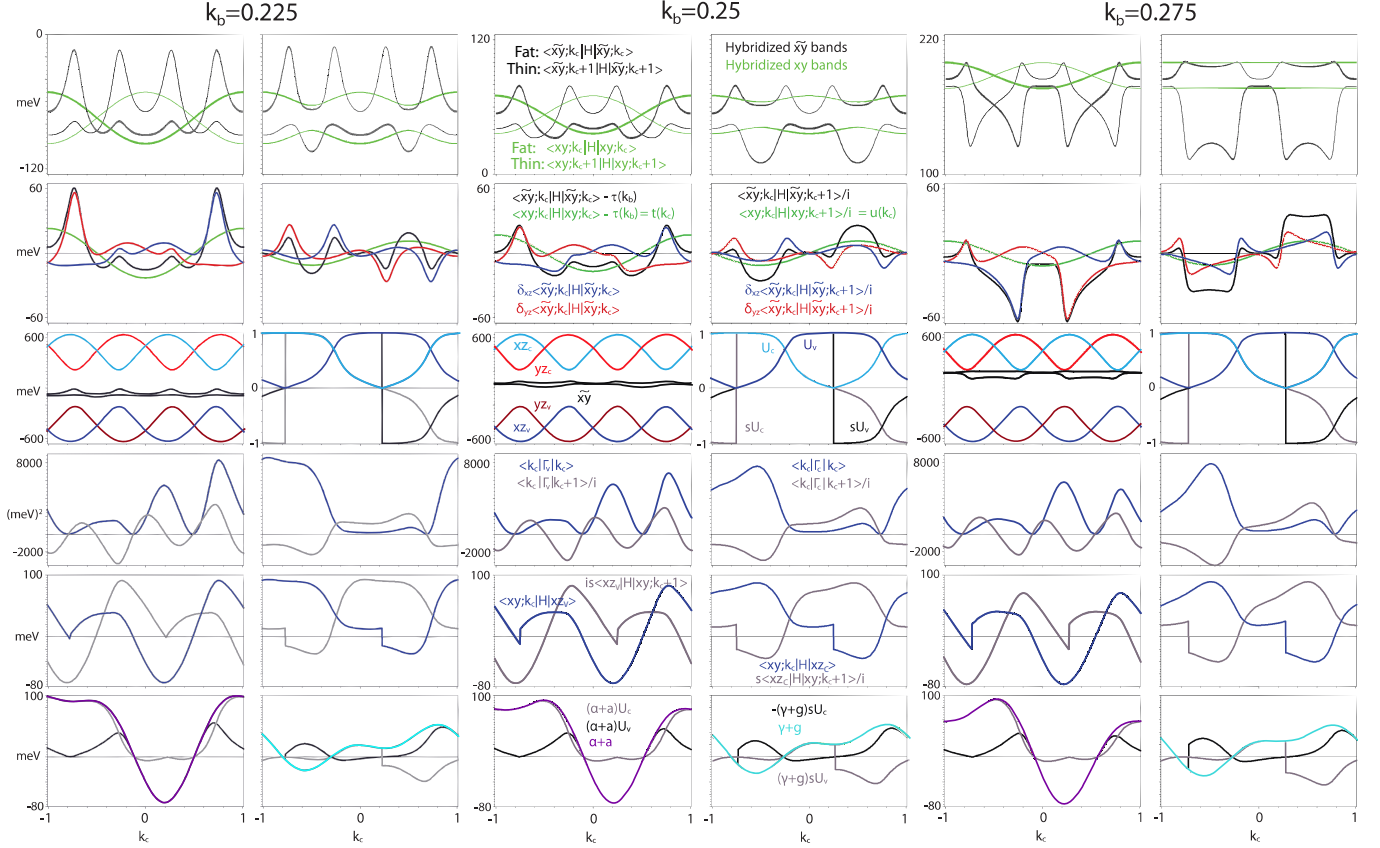


FIG. 16. The following caption is for each of the three k_b -panels: **1st row:** Unhybridized (left) and hybridized (right) \widetilde{xy} bands as fct.s of k_c . The latter are as in FIG. 12, but extended to the double zone. **2nd row:** Diagonal, $\langle \widetilde{xy}; \mathbf{k} | H | \widetilde{xy}; \mathbf{k} \rangle - \tau(k_b)$ (left), and off-diagonal, $\langle \widetilde{xy}; \mathbf{k} | H | \widetilde{xy}; \mathbf{k} + \mathbf{c}^* \rangle / i$ (right), elements of the two-band Hamiltonian (B2). In black, the sum of the contributions from the direct, inter-ribbon xy - XY hops (green) and from the indirect hops via the xz (blue) and yz (red) V&C bands. **3rd row left:** The black \widetilde{xy} bands in the gap between the blue xz and red yz V (dark) & C (light) bands. **3rd row right:** Matrix elements of the unitary transformation (A22) between the xz orbitals in the reciprocal-lattice and V&C representations, U_V (dark blue), U_C (light blue), sU_V (black), and sU_C (grey). The probability that at \mathbf{k} , the $|xz; \mathbf{k}\rangle$ character is in the V band is U_V^2 , and similarly for U_C^2 . **4th row:** Diagonal, $\langle \mathbf{k} | \Gamma | \mathbf{k} \rangle$ (blue), and off-diagonal, $\langle \mathbf{k} | \Gamma | \mathbf{k} + \mathbf{c}^* \rangle / i$ (grey), matrix elements in meV^2 of the residue for the perturbation of the two-band Hamiltonian via the xz V band (left) or C band (right). **5th row:** The factors $\langle xy; \mathbf{k} | H | xz_V \rangle$ (blue) and $\langle xz_V | H | xy; \mathbf{k} + \mathbf{c}^* \rangle / (-is)$ (grey) of Γ_V (left) and the factors $\langle xy; \mathbf{k} | H | xz_C \rangle$ (blue) and $\langle xz_C | H | xy; \mathbf{k} + \mathbf{c}^* \rangle / (is)$ (grey) of Γ_C (right). Blue and grey curves are related by a \mathbf{c}^* translation. **6th row left:** $\alpha + a$ (purple) and the products, $(\alpha + a)U_V$ (black) and $(\alpha + a)U_C$ (grey), which are the first terms in respectively Eq.s (B8) and (B7). **6th row right:** $\gamma + g$ (turquoise) and the products, $-(\gamma + g)sU_C$ (black) and $(\gamma + g)sU_V$ (grey), which are the second terms in the above mentioned Eq.s. Energies are in meV, the ARPES-refined parameter values have been used, and we have approximated E in the resonance terms by $\tau(k_b)$.

respectively. The edges, $\mp 2|G_1|$, of the xz bands (stippled blue in Fig. 5) are along $k_c = k_b \mp \frac{1}{2} + 2n$, which for the three chosen values of k_b , and for k_c in the $(-1|1)$ double-zone are at $k_c \sim -0.25$ and 0.75 . This is where the xz -band edges may cause resonance peaks in the \widetilde{xy} bands.

When $k_b=0.225$, there is a large peak in the unhybridized $\widetilde{xy}(\mathbf{k})$ band near 0.75 and a small one near -0.25 . Both point upwards, i.e. are caused by repulsion from the xz valence band. Their sizes decrease strongly as with increasing k_b the \widetilde{xy} bands move upwards, away from the valence band. For $k_b=0.250$, the peaks can still be seen in the unhybridized $\widetilde{xy}(\mathbf{k})$ bands to the left in the

1st and 2nd rows (black and blue), as well as in the fully hybridized \widetilde{xy} band in the 1st row to the right. But for $k_b=0.275$, when the upper \widetilde{xy} band is touching the bottom of the conduction-band edge, only the peak from the xz valence-band resonance near 0.75 has survived. The small peak near -0.25 has been overpowered by a (too) large, downwards pointing conduction-band resonance, shaped like a canine tooth. Going back to $k_b=0.250$, this tooth is reduced to a "hole" on the low- k_c side of the small blue valence-band peak near $k_c=-0.25$.

The contribution from the xz V&C bands to the hybridization between the $\widetilde{xy}(\mathbf{k})$ and $\widetilde{xy}(\mathbf{k} + \mathbf{c}^*)$ bands is shown in blue (and divided by i) on the 2nd line to the

right. Whereas the diagonal element of the residue matrix (B3) is positive definite, its off-diagonal elements are purely imaginary and anti-periodic, i.e. they change sign upon translation of k_c by 1. For $k_b=0.225$ the peak near 0.75 is similar to that of the diagonal element, but its magnitude is reduced by roughly a factor 2. For k_b increasing, this peak decreases and gets superposed by the growing, anti-periodic canine-tooth structure. The $\widetilde{xy}(\mathbf{k})$ and $\widetilde{xy}(\mathbf{k} + \mathbf{c}^*)$ bands are degenerate at the BZ boundary, $k_c=\pm 0.5$, but get split by \pm the numerical value of the off-diagonal element of the two-band Hamiltonian (B2), which is seen to increase strongly with k_b . The reason is, as we shall see below, that the contribution from the valence band vanishes at the zone boundary. The uncompensated repulsion from the conduction band is then what causes the development of the bulge in the lower \widetilde{xy} band.

The valence band thus causes peaks in the upper, quasi-1D band, and the conduction band causes canine teeth plus zone-boundary-centered bulges, which merge the teeth, in the lower band. The peaks and the teeth are resonance features occurring where the xy -like FS, $|k_b|=\frac{1}{4}$, crosses above the edges, $|k_c \pm k_b|=\frac{1}{2}$, of xz and yz -like bands.

e. Indirectly coupled terms; role of the residues

The residues of the 4 resonance terms in expression (B2) are 2×2 matrices whose elements are products of xz - xy and yz - xy hybridization matrix elements (A25). For $\Gamma_C(\mathbf{k})$, this is expressed in Eq. (B3).

The form (B3) with $\langle xy; \mathbf{k} | H | xz; \mathbf{k} \rangle$ real and $\langle xz; \mathbf{k} | H | xy; \mathbf{k} + \mathbf{c}^* \rangle$ imaginary, causes the two *eigenvalues* of the $\Gamma_C(\mathbf{k})$ -matrix, $\langle \mathbf{k} | \Gamma_C | \mathbf{k}' \rangle$, to be:

$$\Gamma_0(\mathbf{k}) = \begin{pmatrix} 0 & 0 \\ \langle \mathbf{k} | \Gamma | \mathbf{k} \rangle + \langle \mathbf{k} + \mathbf{c}^* | \Gamma | \mathbf{k} + \mathbf{c}^* \rangle & 0 \end{pmatrix}. \quad (\text{B4})$$

Since this holds for any of the 4 residues, subscripts and overbars have been dropped. Obviously, the eigenvalues are periodic in the single zone. With the residue possessing no negative eigenvalue, the sign of the resonance term is that of the denominator, i.e. it is repulsive. As a consequence, if the Hamiltonian minus $\tau(k_b)$ is dominated by *one* of the resonance terms, e.g. due to a small denominator, that term will repel *one* of the two xy bands, and leave the other unperturbed.

An example is the resonance peak in the upper \widetilde{xy} band together with the flat lower \widetilde{xy} band seen in FIG. 11 (c2) for $k_b=0.225$, and in FIG. 12, also for $k_b=0.250$. From the latter figure we confirm that the energy of the lower band is approximately at the average of the two green xy bands. Further confirmation follows from FIG. 16: Here, we take the resonance peak as the one caused by the xz valence band near $k_c=0.75$, whereby the two bands are those seen to the right in the top row. The relevant parts of $\frac{\langle \mathbf{k} | \Gamma_V | \mathbf{k} \rangle}{\tau(k_b) + \sqrt{A^2(\mathbf{k}) + G^2(\mathbf{k})}}$ and $\frac{\langle \mathbf{k} + \mathbf{c}^* | \Gamma_V | \mathbf{k} + \mathbf{c}^* \rangle}{\tau(k_b) + \sqrt{A^2(\mathbf{k}) + G^2(\mathbf{k})}}$, are

those near $k_c=-0.25$ and 0.75 of the blue hybridized δ_{xz} band in the 2nd row to the left. The closeness of the black and blue curves confirms that the Hamiltonian is, in fact, dominated by this *one* resonance term.

Next, we go to $k_b=0.275$ where the \widetilde{xy} bands are located just below the bottom of the C bands. The peak in the upper band caused by the repulsion from the V-band edge can still be seen near $k_c=0.75$ to the right in the top row, but the nearby C-band edge repels the lower band much further. In fact, it is now the upper band which is the flatter and has an energy near the average of the two green bands. The closeness of the black and blue curves in the 2nd row to the left confirms that the Hamiltonian is dominated by the xz -band resonances, with a minor, peak-shaped contribution from the V band near $k_c=0.75$ and a major, contribution with the shape of a canine tooth from the C band near $k_c=-0.25$.

This behavior is also clearly seen in the band structures (FIG.s 7 and 11) along the ZY and WA lines as was described in Sect. V E. This may also lie behind the "non-linearity" seen in FIG. 17 2(b).

We now return to study the \mathbf{k} -dependence of the residues in their common $\{|\mathbf{k}\rangle, |\mathbf{k} + \mathbf{c}^*\rangle\}$ representation. Since translation of \mathbf{k} by \mathbf{c}^* yields:

$$\widehat{\mathbf{c}^*} \langle \mathbf{k} | \Gamma | \mathbf{k} \rangle = \langle \mathbf{k} + \mathbf{c}^* | \Gamma | \mathbf{k} + \mathbf{c}^* \rangle, \quad (\text{B5})$$

the two diagonal elements with \mathbf{k} in the single zone reduce to *one* real-valued function with \mathbf{k} running over the double zone. For the purely imaginary off-diagonal element:

$$\begin{aligned} \widehat{\mathbf{c}^*} \langle \mathbf{k} | \Gamma | \mathbf{k} + \mathbf{c}^* \rangle &= \langle \mathbf{k} + \mathbf{c}^* | \Gamma | \mathbf{k} \rangle = \\ \langle \mathbf{k} | \Gamma | \mathbf{k} + \mathbf{c}^* \rangle^* &= - \langle \mathbf{k} | \Gamma | \mathbf{k} + \mathbf{c}^* \rangle, \end{aligned} \quad (\text{B6})$$

i.e. it is an anti-periodic function of \mathbf{k} .

In FIG. 16 in the 4th row to the right we show the residue matrix, $\Gamma_C(\mathbf{k})$, with the diagonal element in blue and the off-diagonal element in grey. The former, \mathbf{k} -conserving perturbation of the $xy(\mathbf{k})$ band via the xz C band proceeds mainly through its $|\mathbf{k}\rangle$ character and is therefore expected to be strong where this character dominates and weak where the complementary character, $|\mathbf{k} + \mathbf{c}^*\rangle$, dominates. The shape of the blue curve should therefore correlate with the extent of the light-blue xz C band shown to the left on the 3rd line. Remembering from Eq.s (13), (14), and (A3) [103] that the pure $xz(\mathbf{k})$ and $xz(\mathbf{k} + \mathbf{c}^*)$ bands have their maxima for respectively odd and even values of $k_c - k_b$, i.e. at respectively $k_c = -0.775, -0.750, -0.725 \sim -0.75$ and $k_c = 0.225, 0.250, 0.275 \sim 0.25$, the $|\mathbf{k}\rangle$ character of the xz C band dominates around -0.75 , and the $|\mathbf{k} + \mathbf{c}^*\rangle$ character dominates around 0.25, both in windows of width 1. This is as expected. However, using the same argument for the shape of the grey, anti-periodic curve showing the matrix element mixing the $xy(\mathbf{k})$ and $xy(\mathbf{k} + \mathbf{c}^*)$ bands via the xz C band, would make us expect zeroes near -0.75 and 0.25, which do, however, not occur. Even worse for $\Gamma_V(\mathbf{k})$ whose diagonal and

off-diagonal elements are shown on the left-hand side of the 4th line. Since the k_c -positions of the minima and maxima of the pure $xz(\mathbf{k})$ and $xz(\mathbf{k} + \mathbf{c}^*)$ bands are shifted by 1, we would expect the blue $\Gamma_V(\mathbf{k})$ and $\Gamma_C(\mathbf{k})$ curves to have the same shapes. But, clearly, $\Gamma_V(\mathbf{k})$ is more complicated than that; it in particular vanishes near $k_c=0.5$. The pitfall in our reasoning is that the $\langle xy; \mathbf{k} | H | xz_C(\mathbf{k}) \rangle$ and $\langle xz_C(\mathbf{k}) | H | xy; \mathbf{k} + \mathbf{c}^* \rangle$ hybridizations in Eq. (B3) have been substituted by overlaps, which means that the $\{|\mathbf{k}\rangle, |\mathbf{k} + \mathbf{c}^*\rangle\}$ -mixing effect of the Δ -block (A20) has been neglected.

We must therefore more carefully disentangle the effects of the two xz -to- XZ and XZ -to- xz hopping integrals –whose Bloch-summed average $A(k_c - k_b)$ and difference $G(k_c - k_b)$ are given by Eq. (A3)– from those of the many xy - xz and xy - XZ hopping integrals whose Bloch-summed averages, $\alpha(\mathbf{k}) + a(\mathbf{k})$, and differences, $\gamma(\mathbf{k}) + g(\mathbf{k})$, are given by Eqs (A4). Remember that the averages conserve \mathbf{k} and $\mathbf{k} + \mathbf{c}^*$, while the differences mix them.

We start with the roles of A and G in determining the conduction- and valence-band eigenfunctions, $|xz_C\rangle$ and $|xz_V\rangle$. As explained in App. A3, $|xz_C\rangle$ and $|xz_V\rangle$ are linear combinations of $|xz; \mathbf{k}\rangle$ and $|xz; \mathbf{k} + \mathbf{c}^*\rangle$ specified by a unitary matrix, U , whose elements are given by Eqs (A22)-(A23) in terms of A and G . The four elements of U are shown to the right in the 3rd row of FIG. 16 with U_C and U_V in respectively light and dark blue, and with sU_C and sU_V in respectively light and dark grey. The squares of the blue curves give the probabilities that at \mathbf{k} , the $|xz; \mathbf{k}\rangle$ character is in respectively the light-blue C- or the dark-blue V band, or equivalently, that the C-band character is in respectively the $xz(\mathbf{k})$ or $xz(\mathbf{k} + \mathbf{c}^*)$ band, or equivalently, that the V-band character is in respectively the $xz(\mathbf{k} + \mathbf{c}^*)$ or the $xz(\mathbf{k})$ band. As expected, the light-blue U_C dominates around $k_c=-0.75$ and the dark-blue U_V around $k_c=0.25$, both in windows of width 1. The grey lines are the numerical values, sU_C and sU_V , of the two other elements. Note that where the mixing between $|xz; \mathbf{k}\rangle$ and $|xz; \mathbf{k} + \mathbf{c}^*\rangle$ vanishes, s switches between $+$ and -1 , and where sU_C jumps, U_V vanishes with a kink, and vice versa. As a consequence, $sU_C U_V$ is everywhere smooth [101].

The transformation of the six-band Hamiltonian from the $\{|\mathbf{k}\rangle, |\mathbf{k} + \mathbf{c}^*\rangle\}$ - to the mixed representation results in the Hamiltonian (A25) whose first two columns contain the expressions needed in Eq. (B3) for the hybridization matrix elements in terms of the Bloch sums (A4) of the average hopping integrals, $\alpha + a$, and their dimerizations, $\gamma + g$. These expressions are the only ones from where the xy - xz hoppings enter the two-band Hamiltonian. Our naive expectations for the shapes of the $\Gamma_C(\mathbf{k})$ and $\Gamma_V(\mathbf{k})$ curves in the 4th row were equivalent to the assumption that $\alpha(\mathbf{k}) + a(\mathbf{k})$ is fairly constant and $\gamma(\mathbf{k}) + g(\mathbf{k})$ negligible. In the 5th row of FIG. 16, and

in blue, we now show the correct hybridization elements:

$$\langle xy; \mathbf{k} | H | xz_C \rangle = (\alpha + a) U_C + (\gamma + g) s U_V \quad (\text{B7})$$

$$\langle xy; \mathbf{k} | H | xz_V \rangle = (\alpha + a) U_V - (\gamma + g) s U_C, \quad (\text{B8})$$

with the former to the right and the latter to the left. Squaring these curves yields the blue ones directly above in the 4th row. Those latter are the diagonal elements of the residues. Note that since $sU_C U_V$ is smooth, so are the curves on the 4th line.

The diagonal element, $\langle \mathbf{k} | \Gamma_C | \mathbf{k} \rangle = |\langle xy; \mathbf{k} | H | xz_C \rangle|^2$, of the conduction-band residue is reasonably constant in the k_c -interval where U_C dominates, $(-1.25| -0.25)=(0.75|1.75)$, and is small outside. A small exception is that $\langle \mathbf{k} | \Gamma_C | \mathbf{k} \rangle$ dips to zero near the 0.75-edge due to a zero of $\langle xy; \mathbf{k} | H | xz_C \rangle$ which, itself, is caused by a zero of $\alpha + a - \gamma - g$ [see Eq. (B9) and the purple and turquoise lines in row 6]. This vanishing of the conduction-band repulsion is what allows the valence-band peak to be seen in the 1st row, even for $k_b=0.275$ when the $\tilde{x}\tilde{y}$ bands are far away from valence band. For k_c increasing inside the U_C window, $\langle xy; \mathbf{k} | H | xz_C \rangle$ rises to a large, 90-meV tall peak, which is near $-0.5=1.5$ when $k_b=0.275$, and develops into a window-filling plateau when $k_b=0.225$ and the $\tilde{x}\tilde{y}$ bands are far away from the conduction band. We also see the k_c -position of the window shifting with k_b .

In contrast to this simple behavior, the *valence*-band residue, $\langle \mathbf{k} | \Gamma_V | \mathbf{k} \rangle = |\langle xy; \mathbf{k} | H | xz_V \rangle|^2$, drops to zero near -0.1 and 0.5 inside the interval $(-0.25|0.75)$ where U_V dominates. This was noted before, and the reason is now seen to be zeroes of $\langle xy; \mathbf{k} | H | xz_V \rangle$ which are, themselves, caused by zeroes of $\alpha + a$. This is confirmed by the shapes of the $\alpha + a$ and $(\alpha + a) U_V$ curves shown to the left in the 6th row in respectively purple and black. The third zero of $\langle xy; \mathbf{k} | H | xz_V \rangle$ is outside the U_V -window and near $-0.85 (=1.15)$. It is caused by a zero of $\gamma + g$ as shown in turquoise in the 6th row to the right. The linear rise of $\langle xy; \mathbf{k} | H | xz_V \rangle$ for k_c decreasing below -0.85 , culminates in the sharp, 90 meV tall peak at the band edge near $-1.25=0.75$. It is initially caused by the term $-(\gamma + g) s U_C$ in (B8), but is subsequently taken over by $(\alpha + a) U_V$, both shown in black in line 6.

The peaks due to resonances with the xz bands occur near the band edges. $U_C=U_V$ exactly at the edges, where the \mathbf{k} -conserving part of the residues then takes the values:

$$\langle \mathbf{k} | \Gamma_C | \mathbf{k} \rangle = \frac{1}{2} [(\alpha + a) \pm s(\gamma + g)]^2. \quad (\text{B9})$$

The magnitudes and signs of $\alpha + a$ and $\gamma + g$ shown in respectively purple and turquoise in the 6th row, cause the Γ_V coupling at the $k_c=0.75$ edge, where $s=-1$, and the Γ_C coupling at the $k_c=-0.25$ edge, where $s=1$, to be much stronger than the two others, i.e. than the Γ_V coupling at -0.25 and the Γ_C coupling at 0.75 , which even has a "hole" here. This is exactly the behavior of the blue peaks seen in the 2nd row to the left.

We now come to the grey, off-diagonal elements, $\langle \mathbf{k} | \Gamma | \mathbf{k} + \mathbf{c}^* \rangle$, in the 4th row. They are, roughly speaking, anti-periodic (B6) versions of the double-periodic blue, diagonal elements. In the 5th row, the grey curves shown expression (B7) to the right and (B8) to the left, both with k_c translated by 1. Keeping in mind, that under this translation, Greek lettered functions are invariant (A6), Latin-lettered functions change sign (A7), and U_C and U_V are exchanged (A23), the grey curves to the right and to the left equal respectively $-is \langle xz_C | H | xy; \mathbf{k} + \mathbf{c}^* \rangle$ and $is \langle xz_V | H | xy; \mathbf{k} + \mathbf{c}^* \rangle$. The off-diagonal elements of the residues shown grey in the 4th row are therefore simply the products of the blue and grey curves shown vertically below in the 5th row, times $\pm is$. The reason why the grey $\langle \mathbf{k} | \Gamma_V | \mathbf{k} + \mathbf{c}^* \rangle$ to the left is far more wiggly than the grey $\langle \mathbf{k} | \Gamma_C | \mathbf{k} + \mathbf{c}^* \rangle$ to the right is, that not only does the former possess the two "extra" zeroes from $\alpha + a$ near -0.1 and 0.5 , as well as the one from $\gamma + g$ at -0.85 , but also those translated by 1, i.e. those near -0.5 , 0.9 , and 0.15 .

These very different k_c -dependencies seen in the 4th row of the blue $\langle \mathbf{k} | \Gamma_C | \mathbf{k} \rangle$ and $\langle \mathbf{k} | \Gamma_V | \mathbf{k} \rangle$ curves, and of the grey $\langle \mathbf{k} | \Gamma_C | \mathbf{k} + \mathbf{c}^* \rangle$ and $\langle \mathbf{k} | \Gamma_V | \mathbf{k} + \mathbf{c}^* \rangle$ curves, i.e. of the conduction- and valence-band residues, are the cause of the strong asymmetry of the perpendicular dispersion and splitting of the quasi-1D bands around the centre of the gap.

f. xy - xz and xy - yz hopping integrals

The purple $\alpha + a$ and turquoise $\gamma + g$ Bloch sums (A4) shown in the 6th row are determined by the hopping integrals, a_n , g_n , α_n , and γ_n , computed as matrix elements (5) of the LDA Hamiltonian between n th-nearest-neighbor xy and xz or XZ WOs (see FIG. 6) with the results given in Table (A11). Specifically, the integrals for hopping between xy and XZ WOs on *different* sublattices are $a_n \pm g_n$. Here, a_1 is the average of- and g_1 half the difference between the integrals for hopping from xy at the origin to XZ on the neighboring ribbon, inside or outside the same bi-ribbon, i.e. to XZ at respectively $-0.012\mathbf{a} - 0.5\mathbf{b} + 0.467\mathbf{c}$ and $-(0.012\mathbf{a} - 0.5\mathbf{b} + 0.533\mathbf{c})$. Similarly for a'_1 and g'_1 , except that the XZ orbital is translated by \mathbf{b} [see Eq. (9)]. For a_2 and g_2 , the XZ WO is translated by $-2\mathbf{b}$, and for a'_2 and g'_2 , by $2\mathbf{b}$. For the Greek-lettered hopping integrals, the two orbitals are on the *same* sublattice. Specifically, the integrals for hopping from xy at the origin to xz at $\pm\mathbf{b}$ are $\alpha_1 \pm \gamma_1$, to xz at $\pm\mathbf{c}$ are $\alpha_2 \pm \gamma_2$, to xz at $\pm(\mathbf{c} + \mathbf{b})$ are $\alpha_3 \pm \gamma_3$, and to xz at $\pm(\mathbf{c} - \mathbf{b})$ are $\alpha'_3 \pm \gamma'_3$. Calling γ an electronic dimerization is really a misnomer, because the reason for its existence is simply the difference of relative orientation of the two orbitals. Finally, α_0 is the xy - xz on-site (crystal-field) term.

The parameters dominating the behavior of the $\alpha + a$ Bloch sum are: the integral for hopping between the xy and XZ nearest-neighbor WOs, $a_1 = -49$ meV, and

the crystal-field term, $\alpha_0 = 31$ meV. Had the former been the only non-vanishing parameter in the $\alpha + a$ Bloch sum, the corresponding term, $2a_1 \cos \pi(k_c - k_b)$, would have killed the peak from the valence-band resonance at $|k_c - k_b| = \frac{1}{2}$. So, clearly, this peak –convincingly observed with ARPES– is sensitive to the value of the crystal-field term caused by the ribbon-inversion (see Sect. III A) and to the details of the xy - XZ and xy - xz hoppings. Remember, that none of these parameter values were adjusted to the ARPES.

g. Synthesis

From the bottom four rows in FIG. 16 we have seen that the k_c -dependencies of the A , G , $\alpha + a$, and $\gamma + g$ Bloch sums of the xz - xz and xy - xz hopping integrals change relatively little for k_b in the $\pm 10\%$ range around $k_F = \frac{1}{4}$.

By far the strongest k_b -variation of the \widetilde{xy} bands displayed in the top two rows is the one coming from the denominators of the four resonance terms via $E \approx \tau(k_b)$, in combination with the very different shapes of the V- and C-band residues.

What makes the blue resonance peak near $k_c = 0.75$ from the edge of the xz V band differ in shape from the (unhybridized) blue canine-tooth resonance near $k_c = -0.25$ from the edge of the xz C band, is the zero of $\alpha + a$ near $k_c = 0.5$. This zero is a bit inside the frame of the U_V window ($-0.25|0.75$) and therefore "cuts a hole" in Γ_V on the low- k_c side of the resonance, which is thereby sharpened up (see the blue curves to the left in the 4th row). Nothing like this happens for Γ_C near $k_c = -0.25$, because the zero of $\alpha + a$ near -0.1 is outside the U_C window ($-1.25|-0.25$). Hence, it is the shape of the canine tooth which is the simpler.

On the other hand, as seen for $k_b = 0.275$ in the 1st row to the left, the backside of the tooth at $k_c = -0.25$ reaches across the zone boundary at -0.5 , where it is crossed symmetrically by the tooth in the $\widetilde{xy}(\mathbf{k} + \mathbf{c}^*)$ band caused by the resonance from the edge of the yz C band at -0.75 . To the right and in black, we now see that strong $(\mathbf{k}, \mathbf{k} + \mathbf{c}^*)$ hybridization around -0.5 merges the canine teeth in the lower band at -0.75 and -0.25 , thus resulting in a 60-meV splitting of the two \widetilde{xy} bands (see also FIG. 12).

We can go back and compare with what happens for $k_b = 0.225$. Here, we see in the 2nd row to the left that the blue resonance peak at 0.75 is so sharp, that it hardly reaches the zone boundary at 0.5 and therefore hardly overlaps the peak at 0.25 in the $\widetilde{xy}(\mathbf{k} + \mathbf{c}^*)$ band (seen above, in the 1st row) from the yz valence band. Moreover, the hybridization at the zone boundary is much weaker than for $k_b = 0.275$ (black curves to the right in the 2nd row) so that it merely leads to the formation of a bulge in the lower band, 35 meV below the gap between the resonance peaks in the upper band (1st row, to the right and FIG. 12).

The zero of $\alpha + a$ near $k_c = 0.5$ which sharpens the peaks from the V bands, also makes the V bands (dark blue and dark red in row 3) contribute nothing to the *hybridization at the zone boundary*, which therefore comes *exclusively from the C bands and from the dimerization, u, of the direct, perpendicular hops* (green curves to the right in the 2nd row). The blue and the red –equally large– contributions each have a residue given by the value at 0.5 of the grey curve to the right on row 4. For k_b increasing from 0.255 to 0.275, this value increases from 2500 to 3500 meV² and thereby enhances the dominating effect of the decreasing denominator. Since from Eq.s (B2), (B3), and (B7):

$$\Gamma_C(k_b, 0.5) = -\Gamma_C(k_b, -0.5) = (\alpha + a)_{-0.5}(\gamma - g)_{-0.5} = (\alpha + a)_{-0.5}(\gamma + g)_{0.5},$$

the increase comes from $\gamma + g$.

We finally explain why around $k_c = 0$ the lower band is so flat, more than the upper band, and why with increasing k_b this flatness increases, but its range decreases. This is important for nesting and gapping of the FS as was seen in FIG. 15 and discussed Sect. VIE. But first, we return to the question raised at the end of App. B1 a why the repulsion of the upper \widetilde{xy} band by the C-band increases far less than expected from the decrease of the denominators (see FIG. 16 on the 3rd row to the left). The reason can be found on the 4th row to the right and the 6th row to the left: For the upper band near $k_c = 0$, which is the $\widetilde{xy}(k_b, k_c + 1)$ band, the C-band residue, $\Gamma_C(k_b, k_c \approx 1) = |\langle xz_C | H | xy \rangle|^2$, decreases by a factor 4 for k_b increasing from 0.225 to 0.275, and this is mainly [see Eq. (B7)] due to $\alpha + a$ decreasing by nearly a factor 2. This trend is furthermore enhanced by a non-vanishing repulsion from the V band whose residue seen on the 4th row to the left hardly changes with k_b and thus becomes more important when $\Gamma_C(k_b, 1)$ is small.

We now understand that the reason why the lower band is more flat than the upper band, is the same as the reason why the blue resonance peak near $k_c = -0.25$ is much smaller than the one near 0.75, namely that $\Gamma_V(k_b, -0.25) \ll \Gamma_V(k_b, 0.75)$, and this in itself is because the zero of $\alpha + a$ at $k_c = -0.1$ is closer to -0.25 than the zero at 0.5 to 0.75. The dispersion of the lower band around $k_c = 0$ therefore decreases as the V-band denominator increases with k_b (3rd row to the left). As the C-band is approached, canine teeth growing near $k_c = -0.25$ and 0.25 limit the region over which the lower band is flat.

We conclude that the remarkable asymmetry between the contributions from the valence- and the conduction bands to the k_c -dispersion and splitting of the xy bands in the gap, is mainly due to the difference between the positions of the xz valence and conduction bands with respect to the structure in the \mathbf{k} -conserving $\alpha + a$ Bloch sum of the xy - xz hopping integrals. Specifically, the zero of $\alpha + a$ near $k_c = 0.5$ is inside the region where the valence band is formed by the $xz(\mathbf{k})$ band and the conduction band is formed by the $xz(\mathbf{k} + \mathbf{c}^*)$ band, and not the other way around.

2. Spin-spiral bands

We shall assume that the SDW addressed in Sect. VIE has the form of a spin spiral (SS) in which all spins have the same length m , and lie in the same plane, but turn by the angle $2\pi \mathbf{T} \cdot \mathbf{q}$ upon translation by \mathbf{T} of the \widetilde{xy} WO on the $(\mathbf{a}, \mathbf{b}, \mathbf{c})$ -lattice [104, 105]. Hence, for $\mathbf{q} = \mathbf{b}^*/2$, the spin changes direction by 180° in the alternating lattice planes perpendicular to \mathbf{b} , whereby this SS is simply a collinear antiferromagnet. We shall neglect the spin-orbit coupling, which is a good approximation for $k_b = 0.225$ –0.275, and the SS therefore has translational symmetry in both spin and orbital spaces, so that \mathbf{k} is conserved. With $\mathfrak{h}(\mathbf{k})$ being the spin-less (paramagnetic) Hamiltonian, the one of the SS is:

$$\begin{array}{cc} \uparrow & \downarrow \\ \uparrow & -\frac{\Delta}{2} + \frac{1}{2} [\mathfrak{h}(\mathbf{k} + \frac{1}{2}\mathbf{q}) + \mathfrak{h}(\mathbf{k} - \frac{1}{2}\mathbf{q})] \\ \downarrow & \frac{1}{2} [\mathfrak{h}(\mathbf{k} + \frac{1}{2}\mathbf{q}) - \mathfrak{h}(\mathbf{k} - \frac{1}{2}\mathbf{q})] \end{array} \quad \begin{array}{c} \downarrow \\ h.c. \\ \frac{\Delta}{2} + \frac{1}{2} [\mathfrak{h}(\mathbf{k} + \frac{1}{2}\mathbf{q}) + \mathfrak{h}(\mathbf{k} - \frac{1}{2}\mathbf{q})] \end{array}$$

where Δ is the magnitude of the exchange splitting. The unitary transformation:

$$\begin{pmatrix} 1 & -1 \\ 1 & 1 \end{pmatrix} \frac{1}{\sqrt{2}}$$

and a shift of \mathbf{k} to have its origin at $\mathbf{q}/2$, leads to the most simple SS Hamiltonian:

$$\begin{array}{ccc} & (\uparrow - \downarrow)/\sqrt{2} & (\uparrow + \downarrow)/\sqrt{2} \\ (\uparrow - \downarrow)/\sqrt{2} & \mathfrak{h}(\mathbf{k}) & \Delta/2 \\ (\uparrow + \downarrow)/\sqrt{2} & \Delta/2 & \mathfrak{h}(\mathbf{k} + \mathbf{q}) \end{array}.$$

This becomes:

$$\begin{pmatrix} \langle \mathbf{k} | H | \mathbf{k} \rangle & \langle \mathbf{k} | H | \mathbf{k} + \mathbf{c}^* \rangle & \Delta/2 & 0 \\ \langle \mathbf{k} + \mathbf{c}^* | H | \mathbf{k} \rangle & \langle \mathbf{k} + \mathbf{c}^* | H | \mathbf{k} + \mathbf{c}^* \rangle & 0 & \Delta/2 \\ \Delta/2 & 0 & \langle \mathbf{k} + \mathbf{q} | H | \mathbf{k} + \mathbf{q} \rangle & \langle \mathbf{k} + \mathbf{q} | H | \mathbf{k} + \mathbf{q} + \mathbf{c}^* \rangle \\ 0 & \Delta/2 & \langle \mathbf{k} + \mathbf{q} + \mathbf{c}^* | H | \mathbf{k} + \mathbf{q} \rangle & \langle \mathbf{k} + \mathbf{q} + \mathbf{c}^* | H | \mathbf{k} + \mathbf{q} + \mathbf{c}^* \rangle \end{pmatrix}, \quad (\text{B10})$$

when $\mathfrak{h}(\mathbf{k})$ is the two-band Hamiltonian (B2). For simplicity, we have dropped E and \widetilde{xy} in Eq. (B10).

If the off-diagonal element, $\langle \mathbf{k} | H | \mathbf{k} + \mathbf{c}^* \rangle$, is neglected, the Δ -perturbation does not couple between the upper (u) and lower (l) bands, whereby the spin-polarized bands become:

$$E_u(\mathbf{k}) = \frac{1}{2} (\langle \mathbf{k} + \mathbf{c}^* | H | \mathbf{k} + \mathbf{c}^* \rangle + \langle \mathbf{k} + \mathbf{q} + \mathbf{c}^* | H | \mathbf{k} + \mathbf{q} + \mathbf{c}^* \rangle) \pm \frac{1}{2} \sqrt{(\langle \mathbf{k} + \mathbf{c}^* | H | \mathbf{k} + \mathbf{c}^* \rangle - \langle \mathbf{k} + \mathbf{q} + \mathbf{c}^* | H | \mathbf{k} + \mathbf{q} + \mathbf{c}^* \rangle)^2 + \Delta^2} \quad (\text{B11})$$

and

$$E_l(\mathbf{k}) = \frac{1}{2} (\langle \mathbf{k} | H | \mathbf{k} \rangle + \langle \mathbf{k} + \mathbf{q} | H | \mathbf{k} + \mathbf{q} \rangle) \pm \frac{1}{2} \sqrt{(\langle \mathbf{k} | H | \mathbf{k} \rangle - \langle \mathbf{k} + \mathbf{q} | H | \mathbf{k} + \mathbf{q} \rangle)^2 + \Delta^2}. \quad (\text{B12})$$

Here u and l refers to \mathbf{k} in the irreducible zone (see FIG. 12). This is exact for $k_c=0+\text{integer}$ and holds approximately, *except* near the BZ boundaries, $k_c=\pm 0.5$.

At the BZ boundaries the states are degenerate, i.e. $\langle \mathbf{k} | H | \mathbf{k} \rangle = \langle \mathbf{k} + \mathbf{c}^* | H | \mathbf{k} + \mathbf{c}^* \rangle$, so that the upper and lower 2×2 blocks of the Hamiltonian (B10) are factorized by the unitary transformation

$$\begin{pmatrix} 1 & 1 \\ -i & i \end{pmatrix} \frac{1}{\sqrt{2}},$$

thus yielding the two following diagonal blocks (given by respectively the upper or lower sign):

$$\begin{pmatrix} \langle \mathbf{k} | H | \mathbf{k} \rangle \pm \langle \mathbf{k} | H | \mathbf{k} + \mathbf{c}^* \rangle / i & \Delta/2 \\ \Delta/2 & \langle \mathbf{k} + \mathbf{q} | H | \mathbf{k} + \mathbf{q} \rangle \pm \langle \mathbf{k} | H | \mathbf{k} + \mathbf{c}^* \rangle / i \end{pmatrix} \quad (\text{B13})$$

whose eigenvalues are the spin-polarized upper and lower bands.

Appendix C: Experimental Extraction of the FS

In this appendix we describe a three step analysis of the ARPES data to obtain the values of k_{Fb} as a function of k_c that define the FS. Our procedure must take into account the challenge of separating the two xy bands as well as the complex non-Fermi liquid lineshapes. We begin with a general overview of each of these issues.

With respect to the first issue, in the first two steps of the analysis we do not try to separate the two bands, but obtain only the average k_{Fb} . In the first step we look only at the FS map and in the second step we extrapolate the dispersion leading up to E_F to determine a value for k_{Fb} . The second step then also gives a direct measure of the average velocity of the two bands. The third step obtains the splitting of the two bands around the average values. Having taken advantage (in section VB) of an approximate ARPES selection rule to verify that both bands do indeed contribute to the ARPES lineshape, in step three we analyze and interpret the lineshape width

to obtain the splitting of the two bands. For an initial perspective, including the width, we examine the FS maps (integrated over ± 20 meV) of the two samples G and H, also bringing out the sample variation detectable in our experiments. FIG. 17.1.(a) shows the FS map for sample H and 1.(b) for sample G. In the magnification of each branch along k_c –running vertically– one can already notice the *bulge* of the FS, moving outwards where it crosses ZC, the BZ boundary ($k_c=0.5$), compared with where it crosses the ΓY -line ($k_c=0$). Especially for sample G in 1.(a), it appears that there is also a change in width, making the measured excitation near the ΛW -line ($k_c=0.25$) broader. The broadening observed for sample G at the crossing of the FS with ΛW , is clearly due to the *finger* pointing towards Z in the inner sheet, splitting it apart from the outer sheet.

With respect to the second issue, let us remember that LiPB shows a TL-like spectral function with a broad spinon edge feature and a somewhat sharper holon peak feature. For the data here, we show as one fingerprint

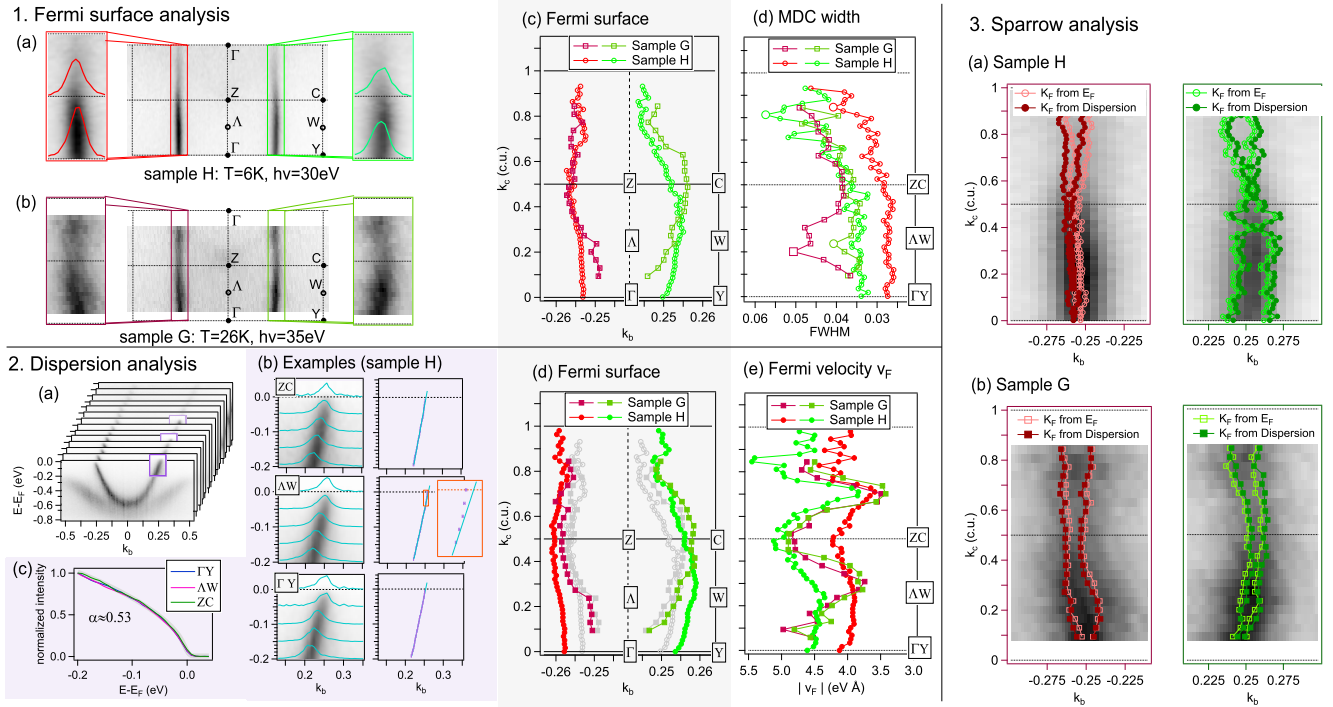


FIG. 17. **1(a)** shows the FS map for sample H ($T = 6\text{ K}$, $h\nu = 30\text{ eV}$) and **1(b)** the FS map for sample G ($T = 26\text{ K}$, $h\nu = 35\text{ eV}$). **1(c)**: The FS $k_F(k_c)$ for each sample is extracted by a line-fit of the MDCs with Lorentzians. **1(d)**: Variation of the Lorentzian width for each sample indicating a splitting of the xy bands. The variation of the width is an upper bound for the splitting. **2(a)**: For the dispersion analysis, the data cube [FIG. 10 (c)] is cut in slices with constant k_c . **2(b)**: On the left are examples for selected slices along ΓY , ΛW , and ZC . The dispersion is determined by a line-fit assuming a Lorentzian line-shape. From the assumption of a linear dispersion, k_F follows. The magnification of the extracted dispersion along ΛW near E_F highlights a non-linearity which might be explained as in the text, or more simply, as the striking asymmetry of the bands seen in FIG. 11. Note that here the double bands cannot be resolved. For that, we need a sophisticated analysis as described in the text. **2(c)**: Integration of the slices over k_b for constant E results in a Luttinger-liquid-like power-law. **2(d)**: the resulting FS $k_{Fb}(k_c)$ has a similar shape as the one shown in weak grey obtained from the FS analysis in 1(c), but is shifted outwards by about 0.005. **2(e)**: The average Fermi velocity, $v_{Fj}(k_c)$, resulting from the 2. analysis. **3**: The Sparrow analysis gives a criterion to compute the upper bound for the splitting. Taking $k_{Fb}(k_c)$ from the 1. or 2. analysis, we can plot for both branches of the FS the two resulting Fermi sheets, $k_{F0}(k_c)$ and $k_{F1}(k_c)$, for sample H (**a**) and sample G (**b**).

of the non-Fermi liquid TL behavior, the momentum integrated EDCs around k_{Fb} shown in FIG. 17. 2(b). A power-law like lineshape can be seen, with a fit using the TL-DOS, as was done as in Ref. [10], that gives $\alpha \approx 0.53$ which is a little bit lower than $\alpha \approx 0.6$ found in Refs. [10, 14, 43]. Speaking about ARPES data analysis in general, the determination of a 'bare electron dispersion' is complicated –even in cases where reasonable assumptions about the spectral function can be made. Some examples are given in Refs. 106–108 where the extractions are discussed for Fermi liquids or marginal Fermi liquids. For TL-like spectral functions the EDCs are very broad, and in general the direct extraction of the FS as in step one or the dispersion as in step 2 must be made with the MDCs, which are much sharper [109].

Although the LiPB ARPES lineshape is well described by the TL spectral function at high T , at low T the spectra do not sharpen as much as expected in the theory [15]. Therefore our specific procedure, described below, follows a route in which no theoretical spectral function is

forced onto the experimental data. However, simulations of our procedure for a TL-spectral function show that the extracted dispersion lies between the spinon and holon dispersions. The exact position depends on the anomalous exponent α , the ratio of the spinon- and holon velocities, and the temperature. Assuming high enough α ($\alpha > 0.5$) the extraction tends to yield a dispersion resembling more the holon branch. Fortunately, there is no holon-spinon splitting at k_{Fb} which, in principle, makes our k_{Fb} -determination valid with respect to this issue.

1. Fermi-surface analysis

In the 1st analysis, we extract k_{Fb} using the momentum distribution curves (MDCs) along the k_b -direction of the FS map, as shown by the (green and red) MDC curves in the magnifications of FIG. 17.1(a). For each MDC, we perform a line-fit using Lorentzians. This re-

sults in the k_{Fb} -values plotted in FIG. 17.1(c). Again, the k_{Fb} -value is smaller at the Γ -line and bends outwards near the ZC-line. FIG. 17.1(d) illustrates the variation in the Lorentzian width which is largest for sample G. Around the Λ -line, we see a broadening. Note that the change of momentum broadening is in the range of 0.005 which translates to the experimentally very demanding range of 0.006 \AA^{-1} ssd (using the solid-state definition of reciprocal space, see Sect. III A).

Although we expect no problem to arise from the holon-spinon splitting, as mentioned above, nonetheless with the k_{Fb} extracted from the Lorentzian fit of the MDCs there is another problem which was already noticed in the case of a marginal Fermi liquid [106] and occurs rather generally. Upon looking more closely at the example MDC curves of FIG. 17.1(a) we can notice a slight asymmetry of the experimental lineshape. Following Ref. 106, the asymmetry is the combined effect of the convolution of the energy resolution and/or the distribution function (in Fermi liquids, the Fermi function), with a spectral function that shows otherwise a completely symmetrical MDC. The asymmetry then causes the extracted k_{Fb} to be closer to the momentum side where the occupied dispersion resides. That this effect plays a role can nicely be seen in the 2nd analysis of the next subsection.

2. Dispersion Analysis

The 2nd analysis goes beyond simply analyzing the MDCs at E_F . Instead, the dispersion in a larger energy window is examined. The process is exemplified in FIG. 17.2(a) where we cut the data in slices with constant k_c . FIG. 17.2(b) shows, on the left, some examples of these slices at some interesting k_c -values. On the right of 2.(b), we show the dispersion as extracted by the Lorentzian fit of the MDCs. Overall, it can be well described by a linear line-fit which extrapolates to cross E_F and thereby provides our second method for determining a k_{Fb} value. This method is a way to bring a larger fraction of the data to bear on the same single number.

The cut along Λ ($k_c=0.25$) in 2.(b) shows in the magnification of the region near E_F a deviation from the linear behavior. A similar behavior is however seen in the TB band structure in FIG. 11 and its origin was ex-

plained at the beginning of Sect. V E. Another cause for this deviation might be the effect described in the preceding paragraph. Hence, the dispersion could be misinterpreted as showing a 'kink', a behavior often taken to imply an interaction with a collective mode. The full systematics of the deviation from the linear behavior can be seen from the graph of FIG. 17.2.(d) where the k_{Fb} resulting from the linear fit is plotted. That k_{Fb} is always larger than the one from the 1. analysis which is underlaid with grey symbols in 2.(d). The magnitude of the bulge is about the same as for the 1st analysis. With this understanding, k_{Fb} from the 2nd method will be used in the following as the best estimate of the true one with the systematic error given by the difference between the results of the 1st and 2nd analysis. Finally, we note that with the average k_{Fb} from both samples being $k_{Fb}^{avg}=0.254 \text{ b}^{-1}$ (0.29 \AA^{-1} using ssd), the Luttinger volume corresponds to an effective $\text{Li}_{1.02}$ stoichiometry, i.e. 51 % electron filling.

The 2nd analysis also gives for each side of the FS the average [78] experimental Fermi-velocity projection along k_b . It is defined in Eq. (28) and shown in FIG. 17.2.(e). Clearly, a variation of v_{Fj} with k_c is visible, showing the quasi-1D character of LiPB as will be quantified further in the following.

3. Sparrow Analysis

In this subsection we estimate the maximum FS splitting, as deduced from the detected variation of the MDC-width at E_F in the 1. analysis. The broadest MDC has width W_{max} and is composed of two Lorentzians. The so-called Sparrow criterion [110] states that two identical, separated Lorentzians are indistinguishable if they add up to give a flat top with zero slope and zero curvature at the center of mass. The peak separation is then $\Delta k_{max} = w/\sqrt{3}$ with each of the two Lorentzian widths being $w = W_{max} \sqrt{3}/(1 + \sqrt{3})$. Assuming these widths to be constant with k_c , they define the peak separation which can be derived from the width variation seen in the 1st analysis.

The obtained separations for both branches of the FS are displayed for sample G in FIG. 17.3. The data from sample H shows, in principle the same features, but was omitted here because of the general better quality of the FS data from sample G.

-
- [1] T. Giamarchi, *Quantum physics in one dimension* (Oxford university press, 2004), URL www.global.oup.com/academic/product/quantum-physics-in-one-dimension-9780198525004.
[2] M. Sing, U. Schwingenschlögl, R. Claessen, P. Blaha, J. M. P. Carmelo, L. M. Martelo, P. D. Sacramento, M. Dressel, and C. S. Jacobsen, Phys. Rev. B **68**, 125111 (2003), URL <https://link.aps.org/doi/10.1103/PhysRevB.68.125111>.

- 1103/PhysRevB.68.125111.
[3] B. Kim, H. Koh, E. Rotenberg, S.-J. Oh, H. Eisaki, N. Motoyama, S. Uchida, T. Tohyama, S. Maekawa, Z.-X. Shen, et al., Nature Physics **2**, 397 (2006), URL www.nature.com/articles/nphys316.
[4] M. Grioni, S. Pons, and E. Frantzeskakis, Journal of Physics: Condensed Matter **21**, 023201 (2009), URL <http://stacks.iop.org/0953-8984/21/023201>.

- $i=2/a=023201$.
- [5] Y. Ohtsubo, J.-i. Kishi, K. Hagiwara, P. Le Fèvre, F. Bertran, A. Taleb-Ibrahimi, H. Yamane, S.-i. Ideta, M. Matsunami, K. Tanaka, et al., Phys. Rev. Lett. **115**, 256404 (2015), URL <https://link.aps.org/doi/10.1103/PhysRevLett.115.256404>.
 - [6] L. Dudy, J. Aulbach, T. Wagner, J. Schäfer, and R. Claessen, Journal of Physics: Condensed Matter **29**, 433001 (2017), URL <http://stacks.iop.org/0953-8984/29/i=43/a=433001>.
 - [7] We do not use the conventional name, $\text{Li}_{0.9}\text{Mo}_6\text{O}_{17}$, because the highly accurate ARPES bands to be described here are filled corresponding to the stoichiometry $\text{Li}_{1.02}\text{Mo}_6\text{O}_{17}$ (see App. C).
 - [8] M. Greenblatt, W. McCarroll, R. Neifeld, M. Croft, and J. Waszczak, Solid State Communications **51**, 671 (1984), ISSN 0038-1098, URL <http://www.sciencedirect.com/science/article/pii/003810988490944X>.
 - [9] M. Onoda, K. Toriumi, Y. Matsuda, and M. Sato, Journal of Solid State Chemistry **66**, 163 (1987), ISSN 0022-4596, URL <http://www.sciencedirect.com/science/article/pii/0022459687902313>.
 - [10] L. Dudy, J. D. Denlinger, J. W. Allen, F. Wang, J. He, D. Hitchcock, A. Sekiyama, and S. Suga, Journal of Physics: Condensed Matter **25**, 014007 (2013), URL <http://stacks.iop.org/0953-8984/25/i=1/a=014007>.
 - [11] G. Wu, X.-s. Ye, X. Zeng, B. Wu, and W. Clark, Scientific Reports **6** (2016), URL www.nature.com/articles/srep20721.
 - [12] J. Chakhalian, Z. Salman, J. Brewer, A. Froese, J. He, D. Mandrus, and R. Jin, Physica B: Condensed Matter **359361**, 1333 (2005), ISSN 0921-4526, proceedings of the International Conference on Strongly Correlated Electron Systems, URL <http://www.sciencedirect.com/science/article/pii/S0921452605004333>.
 - [13] H. Chen, J. J. Ying, Y. L. Xie, G. Wu, T. Wu, and X. H. Chen, EPL (Europhysics Letters) **89**, 67010 (2010), URL <http://stacks.iop.org/0295-5075/89/i=6/a=67010>.
 - [14] F. Wang, J. V. Alvarez, S.-K. Mo, J. W. Allen, G.-H. Gweon, J. He, R. Jin, D. Mandrus, and H. Höchst, Phys. Rev. Lett. **96**, 196403 (2006), URL <http://link.aps.org/doi/10.1103/PhysRevLett.96.196403>.
 - [15] F. Wang, J. V. Alvarez, J. W. Allen, S.-K. Mo, J. He, R. Jin, D. Mandrus, and H. Höchst, Phys. Rev. Lett. **103**, 136401 (2009), URL <https://link.aps.org/doi/10.1103/PhysRevLett.103.136401>.
 - [16] J. Hager, R. Matzdorf, J. He, R. Jin, D. Mandrus, M. A. Cazalilla, and E. W. Plummer, Phys. Rev. Lett. **95**, 186402 (2005), URL <http://link.aps.org/doi/10.1103/PhysRevLett.95.186402>.
 - [17] J. Allen, Solid State Communications **123**, 469 (2002), ISSN 0038-1098, URL <http://www.sciencedirect.com/science/article/pii/S0038109802004258>.
 - [18] G.-H. Gweon, J. W. Allen, and J. D. Denlinger, Phys. Rev. B **68**, 195117 (2003), URL <https://link.aps.org/doi/10.1103/PhysRevB.68.195117>.
 - [19] N. Wakeham, A. F. Bangura, X. Xu, J.-F. Mercure, M. Greenblatt, and N. E. Hussey, Nature communications **2**, 396 (2011), URL www.nature.com/articles/ncomms1406.
 - [20] J.-F. Mercure, A. F. Bangura, X. Xu, N. Wakeham, A. Carrington, P. Walmsley, M. Greenblatt, and N. E. Hussey, Phys. Rev. Lett. **108**, 187003 (2012), URL <http://link.aps.org/doi/10.1103/PhysRevLett.108.187003>.
 - [21] X. Xu, A. F. Bangura, J. G. Analytis, J. D. Fletcher, M. M. J. French, N. Shannon, J. He, S. Zhang, D. Mandrus, R. Jin, et al., Phys. Rev. Lett. **102**, 206602 (2009), URL <https://link.aps.org/doi/10.1103/PhysRevLett.102.206602>.
 - [22] M. H. Whangbo and E. Canadell, Journal of the American Chemical Society **110**, 358 (1988).
 - [23] Z. S. Popovic and S. Satpathy, Phys. Rev. B **74**, 045117 (2006), URL <http://link.aps.org/doi/10.1103/PhysRevB.74.045117>.
 - [24] J. A. M. Haverkort, in *International workshop on Strong correlations and angle-resolved photoemission spectroscopy* (2013), URL <http://corpes13.xfel.eu/>.
 - [25] J. Merino and R. H. McKenzie, Phys. Rev. B **85**, 235128 (2012), URL <http://link.aps.org/doi/10.1103/PhysRevB.85.235128>.
 - [26] P. Chudzinski, T. Jarlborg, and T. Giamarchi, Phys. Rev. B **86**, 075147 (2012), URL <http://link.aps.org/doi/10.1103/PhysRevB.86.075147>.
 - [27] T. Jarlborg, P. Chudzinski, and T. Giamarchi, Phys. Rev. B **85**, 235108 (2012), URL <https://link.aps.org/doi/10.1103/PhysRevB.85.235108>.
 - [28] Since our TB model is considerably more detailed than those previously published [23][27][25][26], we have been forced to change notation. The relation between ours and the earlier notation is: $\tau = t$, $t_1 + u_1 = t_\perp$, and $t_1 - u_1 = t'_\perp$. Note that τ in Sect. III B Eqs (10) and (11) is the coefficient to $\cos \pi n k_b$ whereas τ_n in the Appendix Eq. (A2) are the coefficients to $\cos 2\pi n k_b$. As a result, $\tau \sim 2\tau_1$. Greek and Latin letters denote hops respectively inside the same sublattice, xy - xy and XY - XY , and between sublattices, xy - XY , i.e. essentially intra- and inter-ribbon hops. Subscripts denote the hopping distance. Without subscript, Greek and Latin letters denote Bloch sums of hopping integrals, i.e. functions of $\mathbf{k} = (k_b, k_c)$ which upon translation by \mathbf{c}^* are respectively invariant or change sign. See Eqs (A2)-(A5).
 - [29] The Slater-Koster estimate $\tau=0.9$ eV in Ref. [25] is adjusted down to 0.5 eV, presumably due to misinterpretation of the LDA dispersion[23] between Γ and Y, i.e. over the wavelength $b^*/2$.
 - [30] S. Ejima, F. Gebhard, and S. Nishimoto, Phys. Rev. B **74**, 245110 (2006), URL <https://link.aps.org/doi/10.1103/PhysRevB.74.245110>.
 - [31] J. Merino and J. V. Alvarez, Phys. Rev. B **91**, 035135 (2015), URL <https://link.aps.org/doi/10.1103/PhysRevB.91.035135>.
 - [32] W. Cho, C. Platt, R. H. McKenzie, and S. Raghu, Phys. Rev. B **92**, 134514 (2015), URL <https://link.aps.org/doi/10.1103/PhysRevB.92.134514>.
 - [33] N. Lera and J. V. Alvarez, Phys. Rev. B **92**, 174523 (2015), URL <https://link.aps.org/doi/10.1103/PhysRevB.92.174523>.
 - [34] C. Platt, W. Cho, R. H. McKenzie, R. Thomale, and S. Raghu, Phys. Rev. B **93**, 214515 (2016), URL <https://link.aps.org/doi/10.1103/PhysRevB.93.214515>.
 - [35] P. Chudzinski, The European Physical Journal B **90**, 148 (2017), ISSN 1434-6036, URL <https://doi.org/10.1140/epjb/e2017-70733-4>.
 - [36] O. Sepper and A. G. Lebed, Phys. Rev. B **88**,

- 094520 (2013), URL <https://link.aps.org/doi/10.1103/PhysRevB.88.094520>.
- [37] A. G. Lebed and O. Sepper, Phys. Rev. B **87**, 100511 (2013), URL <https://link.aps.org/doi/10.1103/PhysRevB.87.100511>.
- [38] J. Choi, J. L. Musfeldt, J. He, R. Jin, J. R. Thompson, D. Mandrus, X. N. Lin, V. A. Bondarenko, and J. W. Brill, Phys. Rev. B **69**, 085120 (2004), URL <https://link.aps.org/doi/10.1103/PhysRevB.69.085120>.
- [39] M. Nuss and M. Aichhorn, Phys. Rev. B **89**, 045125 (2014), URL <https://link.aps.org/doi/10.1103/PhysRevB.89.045125>.
- [40] Y. Nohara and O. K. Andersen, Phys. Rev. B **94**, 085148 (2016), URL <https://link.aps.org/doi/10.1103/PhysRevB.94.085148>.
- [41] Y. Nohara and O. K. Andersen (2019), to be submitted.
- [42] O. K. Andersen and T. Saha-Dasgupta, Phys. Rev. B **62**, R16219 (2000), URL <https://link.aps.org/doi/10.1103/PhysRevB.62.R16219>.
- [43] J. D. Denlinger, G.-H. Gweon, J. W. Allen, C. G. Olson, J. Marcus, C. Schlenker, and L.-S. Hsu, Phys. Rev. Lett. **82**, 2540 (1999), URL <http://link.aps.org/doi/10.1103/PhysRevLett.82.2540>.
- [44] K. Breuer, D. M. Goldberg, K. E. Smith, M. Greenblatt, and W. McCarroll, Solid State Communications **94**, 601 (1995), ISSN 0038-1098, URL <http://www.sciencedirect.com/science/article/pii/0038109895001433>.
- [45] We call the xy band the metallic band and –like for semiconductors– call the gapped xz and yz bands valence and conduction bands.
- [46] W. McCarroll and M. Greenblatt, Journal of Solid State Chemistry **54**, 282 (1984), ISSN 0022-4596, URL <http://www.sciencedirect.com/science/article/pii/0022459684901579>.
- [47] M. L. Knotek and P. J. Feibelman, Phys. Rev. Lett. **40**, 964 (1978), URL <http://link.aps.org/doi/10.1103/PhysRevLett.40.964>.
- [48] J. Denlinger, G.-H. Gweon, J. Allen, J. Marcus, and C. Schlenker, Journal of Electron Spectroscopy and Related Phenomena **101-103**, 805 (1999), ISSN 0368-2048.
- [49] S. Moser, L. Moreschini, J. Jaćimović, O. S. Barišić, H. Berger, A. Magrez, Y. J. Chang, K. S. Kim, A. Bostwick, E. Rotenberg, et al., Phys. Rev. Lett. **110**, 196403 (2013).
- [50] S. M. Walker, F. Y. Bruno, Z. Wang, A. de la Torre, S. Ricco, A. Tamai, T. K. Kim, M. Hoesch, M. Shi, M. S. Bahrany, et al., Advanced Materials **27**, 3894 (2015), ISSN 1521-4095.
- [51] L. Dudy, M. Sing, P. Scheiderer, J. D. Denlinger, P. Schütz, J. Gabel, M. Buchwald, C. Schlueter, T.-L. Lee, and R. Claessen, Advanced Materials **28**, 7443 (2016).
- [52] U. von Barth and L. Hedin, Journal of Physics C: Solid State Physics **5**, 1629 (1972), URL <http://stacks.iop.org/0022-3719/5/i=13/a=012>.
- [53] O. Andersen, T. Saha-Dasgupta, R. Tank, C. Arcangeli, O. Jepsen, and G. Krier, *Electronic Structure and Physical Properties of Solids. The Uses of the LMTO Method* (Springer, 2000), URL <https://link.springer.com/book/10.1007/3-540-46437-9>.
- [54] O. Andersen, *NMTOs and their Wannier functions, Correlated Electrons: from Models to Materials: Lecture Notes of the Autumn School Correlated Electrons 2012* (Forschungszentrum Jülich, 2012), vol. 2 of *Schriften des Forschungszentrums Jülich: Reihe Modeling and Simulation*, ISBN 978-3-89336-796-2, URL <http://hdl.handle.net/2128/4611>.
- [55] N. Marzari, A. A. Mostofi, J. R. Yates, I. Souza, and D. Vanderbilt, Rev. Mod. Phys. **84**, 1419 (2012), URL <https://link.aps.org/doi/10.1103/RevModPhys.84.1419>.
- [56] For materials with d - or f -electron atoms in only high-symmetry positions maximally localized and NMTO WFs give similar results when settings are similar [57]. However, maximally localized WFs are not centered at low-symmetry sites, and if forced to, they generally do not transform according to the irreducible representations of the point group. As a consequence, crystal fields depend strongly on the settings. The software found on www.quanty.org interfaces several methods for generating WFs and allows users to compare.
- [57] F. Lechermann, A. Georges, A. Poteryaev, S. Biermann, M. Posternak, A. Yamasaki, and O. K. Andersen, Phys. Rev. B **74**, 125120 (2006), URL <https://link.aps.org/doi/10.1103/PhysRevB.74.125120>.
- [58] M. W. Haverkort, M. Zwierzycki, and O. K. Andersen, Phys. Rev. B **85**, 165113 (2012), URL <https://link.aps.org/doi/10.1103/PhysRevB.85.165113>.
- [59] M. Zwierzycki and O. Andersen, Acta Physica Polonica A **1**, 64 (2009), URL <http://yadda.icm.edu.pl/przyrbwn/element/bwmeta1.element.bwnjournal-article-appv115n1010kz?q=bwmeta1.element.bwnjournal-number-appola-2009-115-1;10&qt=CHILDREN-STATELESS>.
- [60] Actually, the scalar-relativistic Dirac equations.
- [61] L. Vitos, *Computational quantum mechanics for materials engineers: the EMTO method and applications* (Springer Science & Business Media, 2007).
- [62] R. Tank and C. Arcangeli, physica status solidi (b) **217**, 89 (2000), ISSN 1521-3951, URL [http://dx.doi.org/10.1002/\(SICI\)1521-3951\(200001\)217:1<89::AID-PSSB89>3.0.CO;2-C](http://dx.doi.org/10.1002/(SICI)1521-3951(200001)217:1<89::AID-PSSB89>3.0.CO;2-C).
- [63] O. K. Andersen, Phys. Rev. B **12**, 3060 (1975), URL <https://link.aps.org/doi/10.1103/PhysRevB.12.3060>.
- [64] Classical linear muffin-tin orbitals (LMTOs) might be considered ($N=1$)MTOs, but they are not accurate when downfolded[111] to very small basis sets, downfolding comes *after* linearization in LMTO theory..
- [65] E. Zurek, O. Jepsen, and O. Andersen, ChemPhysChem **6**, 1934 (2005), ISSN 1439-7641, URL <http://dx.doi.org/10.1002/cphc.200500133>.
- [66] E. Pavarini, A. Yamasaki, J. Nuss, and O. K. Andersen, New Journal of Physics **7**, 188 (2005), URL <http://stacks.iop.org/1367-2630/7/i=1/a=188>.
- [67] M. I. Aroyo, D. Orobengoa, G. de la Flor, E. S. Tasci, J. M. Perez-Mato, and H. Wondratschek, Acta Crystallographica Section A **70**, 126 (2014), URL <http://dx.doi.org/10.1107/S205327331303091X>.
- [68] As seen in FIG. 1 (b) and (c), the shortest path for hopping of low-energy electrons across the double layer of tetrahedrally coordinated molybdenums is Mo5 - (MO6) - MO5, i.e. from Mo5 in a bottom ribbon, along $-z$ to (MO6) in the top ribbon of the neighboring staircase, and then along $-x$ or $+y$ to MO5 in that top ribbon. This zigzag path thus passes via merely *one* tetrahe-

- drally coordinated Mo atom and gives rise to the slight k_a -dispersion seen along CE in FIG. 2 of the degenerate 4th and 5th bands.
- [69] We denote energy bands $E(\mathbf{k}) = \varepsilon(\mathbf{k}) + E_0$, and their dispersions $\varepsilon(\mathbf{k})$. Here, E_0 is the center of the band.
- [70] For the XYZ system located on MO1 in the upper ribbon, we merely translate the xyz system from Mo1 to MO1. These two parallel, local coordinate systems do *not* follow the space-group symmetry, specifically the centre of inversion between the nearest Mo1-MO1 neighbors. But the t_{2g} projections on the Mo1 and MO1 hard spheres do, because they are even, and this is all what matters for the WOs.
- [71] F. Matsui, T. Matsushita, and H. Daimon, *Journal of Electron Spectroscopy and Related Phenomena* **195**, 347 (2014), ISSN 0368-2048, URL <http://www.sciencedirect.com/science/article/pii/S0368204814000668>.
- [72] H. Daimon, S. Imada, H. Nishimoto, and S. Suga, *Journal of Electron Spectroscopy and Related Phenomena* **76**, 487 (1995), proceedings of the Sixth International Conference on Electron Spectroscopy.
- [73] H. Nishimoto, T. Nakatani, T. Matsushita, S. Imada, H. Daimon, and S. Suga, *Journal of Physics: Condensed Matter* **8**, 2715 (1996), URL <http://stacks.iop.org/0953-8984/8/i=15/a=020>.
- [74] E. L. Shirley, L. J. Terminello, A. Santoni, and F. J. Himpsel, *Phys. Rev. B* **51**, 13614 (1995), URL <http://link.aps.org/doi/10.1103/PhysRevB.51.13614>.
- [75] When discussing ARPES as measured, in particular the CECs, we start from the picture given in Sect. VB of three $xy(\mathbf{k})$, $xz(\mathbf{k})$, and $yz(\mathbf{k})$ energy bands in the (periodically repeated) double zone, but perturbed by back-folding (Umklapp) at the edges of the respective, physical single zones. Note, that back-folding at one of the boundaries, $k_c = \pm 1/2$, of the BZ, which is the physical one for the xy bands—but *not* for the xc or yz bands—is incorrect, because it reflects an xz band in a yz band. When discussing the energy bands, it is correct—and more natural—to start from the picture given in Sect. IV D where \mathbf{k} is in a (periodically repeated) single zone(s), e.g. the BZ, and there are six basis functions, $|m, \mathbf{k})$ and $|m, \mathbf{k} + \mathbf{c}^*)$, whose six bands—before hybridization—are $m(\mathbf{k})$ and $m(\mathbf{k} + \mathbf{c}^*)$.
- [76] For elemental transition metals, 100 meV is the typical size of the s to d energy shift needed to bring the LDA and experimental (dHvA) Fermi surfaces into agreement, see [80].
- [77] Note that whereas the band structure is invariant to the individual mirror operations $k_b \rightarrow -k_b$ and $k_c \rightarrow -k_c$, the eigenfunctions are merely invariant to the inversion $(k_b, k_c) \rightarrow (-k_b, -k_c)$. As a consequence, the above-mentioned even/odd symmetries around $k_c = -1, 0, 1$ and $k_c = \pm 0.5$ do not hold for the blue and red curves individually, but only for their sums.
- [78] The experiment cannot resolve the v_F of each of the bands separately, therefore the experimental extracted v_F represents the average of both.
- [79] The band- and k_c -resolved velocities which result from using the shifted and the straight LDA parameters (see FIG. 7) have averages more than 15% below that of the light-blue velocities in FIG. 14 (b), and they have much larger variations: Near $k_c=0$ and 0.5 the LDA velocities do lie around the 15% lower LDA value, 4.0 eVÅ, but for intermediate values of k_c , they vary much more, reaching minima at 3.4 and 3.0 eVÅ for respectively the upper and lower bands (inner and outer sheets) in the shifted LDA and, in the straight LDA, minima at 2.5 eVÅ and 3.3 eVÅ with the deeper minimum now for the upper band.
- [80] A. Mackintosh and O. Andersen, *The electronic structure of transition metals* (Cambridge University Press, Cambridge, 1980), chap. Electrons at the Fermi surface, pp. 149–224.
- [81] For quasi-particles, one would invoke a very strong k -dependence of the self energy to understand a decrease of the mass, as discussed, e.g., in Ref.112 and Ref.113.
- [82] J. Solyom, *Advances in Physics* **28**, 201 (1979), <https://doi.org/10.1080/00018737900101375>, URL <https://doi.org/10.1080/00018737900101375>.
- [83] J. Voit, *Journal of Physics: Condensed Matter* **5**, 8305 (1993), URL <http://stacks.iop.org/0953-8984/5/i=44/a=020>.
- [84] D. Orgad, *Philosophical Magazine B* **81**, 377 (2001), <https://doi.org/10.1080/13642810108226410>, URL <https://doi.org/10.1080/13642810108226410>.
- [85] We take cognizance that the previous high- T , Γ -Y, TL lineshape analysis [18] found $v_\rho = 4.0$ eVÅ, coincidentally, we think, the same as our LDA value. That our present value of roughly 4.6 eV Å along Γ -Y ($k_c=0$) is somewhat larger could perhaps be due to the considerable temperature difference (250K vs. 6K), the considerable difference in the analyzer angle resolutions along k_b (0.016 Å⁻¹ in the early work vs. 0.006 Å⁻¹ in the present work), or perhaps some small sample dependence. In any case the ratio $v_\rho/v_\sigma \approx 2$ is essentially the same for the present lineshapes and the text conclusion that v_ρ is nontrivially larger than v_F is unaltered.
- [86] J. F. Janak, *Phys. Rev. B* **16**, 255 (1977), note that with Janak's definitions, his I is half- and his DOS twice our value, URL <https://link.aps.org/doi/10.1103/PhysRevB.16.255>.
- [87] O. Gunnarsson, *Journal of Physics F: Metal Physics* **6**, 587 (1976), URL <http://stacks.iop.org/0305-4608/6/i=4/a=018>.
- [88] O. Andersen, *Highlights of Condensed-Matter Theory, Course LXXXIX* (North-Holland, 1985), chap. Canonical description of the band structures of metals, pp. 59–176, international school of physics "enrico fermi" ed., URL www2.fkf.mpg.de/andersen/users/jepsen/Varennna_1985.pdf.
- [89] O. K. Andersen, *From Materials to Models: Deriving Insight from Bands*, vol. 8 of *Lecture Notes of the Autumn School Correlated Electrons 2018* (Forschungszentrum Jülich, 2018), ISBN 978-3-95806-313-6, URL www.cond-mat.de/events/correl18/manuscripts/andersen.pdf.
- [90] We stress that modern theory of direct exchange [114, 115] is based on LSD (or SGGA) and that the above-mentioned value of I is robust. Moreover, for NiO, MnO, and SrTiO₃ the values of the Hund's-rule exchange, J_H , calculated from the spherically averaged TM d WOs as explained in Ref. 58 are within 10 percent of those of I for the respective close-packed metals Ni, Mn, and Ti. This had been anticipated in Ref. 116. Hence, $I = 0.54$ eV should roughly equal J_H for octahedral Mo in LiPB.
- [91] V. Oudovenko, S. Savrasov, and O. Andersen, *Physica C: Superconductivity* **336**, 157 (2000), ISSN 0921-

- 4534, URL <http://www.sciencedirect.com/science/article/pii/S0921453400002823>.
- [92] M. D. Johannes and I. I. Mazin, Phys. Rev. B **77**, 165135 (2008), URL <https://link.aps.org/doi/10.1103/PhysRevB.77.165135>.
- [93] It may be noted that the reduction of $U = 6.4$ eV calculated [19] for an octahedral Mo atom by $24/4$ yields 1 eV, which is in the upperbound range for the 4-orbital set [35].
- [94] G.-H. Gweon, Ph.D. thesis, University of Michigan (1999), URL <https://deepblue.lib.umich.edu/handle/2027.42/131896>.
- [95] P. Kopietz, V. Meden, and K. Schönhammer, Phys. Rev. Lett. **74**, 2997 (1995), URL <http://link.aps.org/doi/10.1103/PhysRevLett.74.2997>.
- [96] S. K. Chan and V. Heine, Journal of Physics F: Metal Physics **3**, 795 (1973), URL <http://stacks.iop.org/0305-4608/3/i=4/a=022>.
- [97] P. B. Littlewood and V. Heine, Journal of Physics C: Solid State Physics **14**, 2943 (1981), URL <http://stacks.iop.org/0022-3719/14/i=21/a=012>.
- [98] R. H. Friend and D. Jerome, Journal of Physics C: Solid State Physics **12**, 1441 (1979), URL <http://stacks.iop.org/0022-3719/12/i=8/a=009>.
- [99] A. P. Petrović, R. Lortz, G. Santi, M. Decroux, H. Monnard, O. Fischer, L. Boeri, O. K. Andersen, J. Kortus, D. Salloum, et al., Phys. Rev. B **82**, 235128 (2010), URL <https://link.aps.org/doi/10.1103/PhysRevB.82.235128>.
- [100] In order to compare with Ref. 99, we took w to be the total width of both bands, contrary to what was done in Sect. VI E.
- [101] We could have avoided the U -functions (A23) which switch between the V and C bands, had we kept the reciprocal-lattice representation for the intermediate xz and yz states, i.e. had we downfolded the six-band Hamiltonian in the reciprocal-lattice representation (A21) instead of in the mixed representation (A25). But the price is that we would lose the description (B1)-(B2) in terms of a sum of single resonances, and that E would enter not only the denominators, but also the numerators.
- [102] The result along $\Gamma'Y'$ ($k_c=\pm 1$) is of course the same although, there, the $|\mathbf{k}\rangle$ bands are anti-bonding and the $|\mathbf{k} + \mathbf{c}^*\rangle$ bands bonding.
- [103] Eqs. (13) and (14) are consistent with the six-band Hamiltonian in the reciprocal-lattice representation (A21).
- [104] L. Sandratskii, Journal of Physics: Condensed Matter **3**, 8565 (1991), URL <http://stacks.iop.org/0953-8984/3/i=44/a=004>.
- [105] O. K. Andersen and L. Boeri, Annalen der Physik **523**, 8 (2011).
- [106] A. Kaminski and H. M. Fretwell, New Journal of Physics **7**, 98 (2005), URL <http://stacks.iop.org/1367-2630/7/i=1/a=098>.
- [107] A. A. Kordyuk, S. V. Borisenko, A. Koitzsch, J. Fink, M. Knupfer, and H. Berger, Phys. Rev. B **71**, 214513 (2005), URL <http://link.aps.org/doi/10.1103/PhysRevB.71.214513>.
- [108] M. Bianchi, E. D. L. Rienks, S. Lizzit, A. Baraldi, R. Balog, L. Hornekær, and P. Hofmann, Phys. Rev. B **81**, 041403 (2010), URL <http://link.aps.org/doi/10.1103/PhysRevB.81.041403>.
- [109] D. Orgad, S. A. Kivelson, E. W. Carlson, V. J. Emery, X. J. Zhou, and Z. X. Shen, Phys. Rev. Lett. **86**, 4362 (2001), URL <https://link.aps.org/doi/10.1103/PhysRevLett.86.4362>.
- [110] A. Jones, J. Bland-Hawthorn, and P. Shopbell, in *Astronomical Data Analysis Software and Systems IV* (1995), vol. 77, p. 503, URL www.adsabs.harvard.edu/full/1995ASPC...77..503J.
- [111] W. R. L. Lambrecht and O. K. Andersen, Phys. Rev. B **34**, 2439 (1986), URL <https://link.aps.org/doi/10.1103/PhysRevB.34.2439>.
- [112] T. Miyake, C. Martins, R. Sakuma, and F. Aryasetiawan, Phys. Rev. B **87**, 115110 (2013), URL <https://link.aps.org/doi/10.1103/PhysRevB.87.115110>.
- [113] C. H. P. Wen, H. C. Xu, Q. Yao, R. Peng, X. H. Niu, Q. Y. Chen, Z. T. Liu, D. W. Shen, Q. Song, X. Lou, et al., Phys. Rev. Lett. **121**, 117002 (2018), URL <https://link.aps.org/doi/10.1103/PhysRevLett.121.117002>.
- [114] R. Cardias, A. Szilva, A. Bergman, I. Di Marco, M. Katsnelson, A. Lichtenstein, L. Nordström, A. Klautau, O. Eriksson, and Y. Kvashnin, Scientific Reports **7**, 4058 (2017), URL www.nature.com/articles/s41598-017-04427-9.
- [115] K. Haule, Journal of the Physical Society of Japan **87**, 041005 (2018), <https://doi.org/10.7566/JPSJ.87.041005>, URL <https://doi.org/10.7566/JPSJ.87.041005>.
- [116] O. Gunnarsson, O. K. Andersen, O. Jepsen, and J. Zaanen, Phys. Rev. B **39**, 1708 (1989), URL <https://link.aps.org/doi/10.1103/PhysRevB.39.1708>.